universität
wien

DISSERTATION

Titel der Dissertation

Development of a metastable helium BEC as a platform for experiments with EPR-entangled matter waves

Verfasser

Maximilian Ebner, M.A.

angestrebter akademischer Grad

Doktor der Naturwissenschaften (Dr. rer. nat.)

Wien, 2012

Inhaltsverzeichnis

Abstract

In the past four years a laboratory has been set up to pursue the fundamental questions of quantum mechanics that can be addressed with correlation measurements of individual atoms in matter-wave experiments. The large coherence length within a Bose-Einstein condensate will be an essential ingredient when the condensate serves as source for matter wave experiments. A four-wave mixing process can be initiated within the condensate to create correlated atom pairs, which is remarkably analogous to the spontaneous parametric down conversion of photons. The pairs are then entangled in the sum of their momenta and the difference of their positions, which is the three dimensional version of the original Einstein-Podolsky-Rosen state. The experimental demonstration of the existence of this entangled state in matter waves promises to open up a playground for matter-wave experiments, extending the successful photonic experiments into the realm of massive particles. Fundamental differences, such as Fermi statistics opposed to Bose statistics, the first order time dependence of the Schrödinger equation opposed to the second order of Maxwell's equations, and gravity, that has a much larger impact on massive opposed to massless particles, will become possible to be tested in the framework of entanglement.

For this purpose, an ultra-cold sample of metastable helium, condensed into a Bose-Einstein condensate has been achieved. After exciting helium-4 to its first excited state the atomic beam is intensified, slowed, and eventually trapped in a magneto-optical trap by optical means. In order to cool the atoms below the Doppler limit of optical cooling, the atoms are transferred to a purely magnetic trap. Quantum mechanical degeneracy is achieved after evaporative cooling of the helium atoms to $1\,\mu\text{K}$ within $10\,\text{s}$. Typically, 10^6 indistinguishable atoms are obtained and serve as a source for later experiments on the statistics of correlated atom pairs.

For detection of the atomic correlations a high resolution, ultra-fast delay-line detector has been installed. The detector consists of a micro-channel plate in combination with a delay line for electronic read out. Each detection event is recorded in space and time with accuracies of $120\,\mu\text{m}$ and $250\,\text{ps}$, respectively.

In order to achieve the correlated atom pairs, lasers to drive Raman transitions have been set up and will be used to initiate the four-wave mixing process. The atoms can then expand under free fall of $80\,\text{cm}$ and drop onto the detector, and hence a three-dimensional reconstruction of the momentum space of the atoms is possible. This opens up the pathway to first experiments for confirming the entanglement of the atom pairs created via the four-wave mixing process.

Finally, various schemes to proof the non-classical correlations have been theoretically investigated and analyzed for their feasibility in the current setup. Among those are a double double-slit and a ghost-interference experiment, in analogy to the experiments with photons of Rarity and Tapster. The analysis showed a scheme with individual collision zones within the Bose-Einstein condensate to be the most promising candidate to demonstrate the correlations of entangled matter waves.

Zusammenfassung

In den vergangenen vier Jahren wurde ein Labor aufgebaut, um grundlegende Fragestellungen der Quantenmechanik, die mit Korrelationsmessungen an individuellen Atomen einer Materiewelle adressiert werden können, zu beantworten. Die große Kohärenzlänge in einem Bose-Einstein-Kondensat, als Quelle für Materiewellen, wird dabei eine wesentliche Rolle spielen. Mit dem Kondensat kann eine Vier-Wellen-Mischung initiiert werden, die zu korrelierten Atompaaren führt, was in bemerkenswerter Analogie zu der spontanen parametrischen Fluoreszenz von Photonen abläuft. Die Paare sind dann in der Summe ihrer Impulse und der Differenz ihrer Position verschränkt, was der dreidimensionalen Version des original Einstein-Podolsky-Rosen-Zustands entspricht. Die experimentelle Demonstration dieses verschränkten Zustands verspricht eine Spielwiese für Materiewellenexperimente zu eröffnen, was die erfolgreichen photonischen Experimente in das Reich der massiven Teilchen erweitert. Dadurch wird es möglich werden fundamentale Unterschiede wie Fermi-Statistik im Gegensatz zu Bose-Statistik, die erste Ordnung in der Zeitabhängigkeit der Schrödinger-Gleichung im Gegensatz zu der zweiten Ordnung in Maxwell's Gleichungen, und Gravitation mit ihrer sehr viel stärkeren Wirkung auf massive Teilchen im Vergleich zu ruhemasselosen Teilchen, im Rahmen von Verschränkung zu testen.

Für dieses Vorhaben wurde eine Probe metastabiler Heliumatome, kondensiert in ein Bose-Einstein Kondensat, erzeugt. Nach dem Anregen von Helium-4 in seinen ersten angeregten Zustand, wird der Atomstrahl mit optischen Mitteln gebündelt, gebremst, und in einer magneto-optischen Falle gefangen. Um die Atome unter das Doppler-Limit zu kühlen, werden die Atome in eine rein magnetische Falle transferiert. Quantenmechanische Entartung wird durch Verdampfungskühlung der Helium Atome bis auf $1\,\mu$K in $10\,$s erreicht. Typischerweise werden 10^6 ununterscheidbare Atome gewonnen und dienen als Ausgangspunkt für die späteren Experimente mit korrelierten Atompaaren.

Zur Detektion der Atomkorrelationen wurde ein hochauflösender, ultraschneller Verzögerungsleitungs-Detektor installiert. Der Detektor besteht aus Mikrokanalplatten in Kombination mit einer Verzögerungsleitung für schnelles, elektronisches Auslesen. Jedes Detektionsereignis wird in Ort und Zeit mit $120\,\mu$m, beziehungsweise $250\,$ps Genauigkeit aufgezeichnet.

Um korrelierte Atompaare zu erzeugen, wurden Laser aufgebaut, die Raman-Übergänge treiben können und später den Vier-Wellen-Prozess einleiten werden. Danach können die Atome im freien Fall $80\,$cm expandieren bevor sie vom Detektor gemessen werden und daraus ein dreidimensionales Bild der Atome im Impulsraum rekonstruiert wird. Das eröffnet die Möglichkeit für Experimente, die die Verschränkung der Atompaare nach dem Vier-Wellen-Prozess beweisen.

Verschiedene Anordnungen, um die nicht-klassischen Korrelationen zu beweisen, wurden theoretisch untersucht und deren Machbarkeit in dem aktuellen Aufbau analysiert. Darunter befinden sich Doppel-Doppelspalt- und Geisterinterferenz-

Experimente, welche analog zu den Experimenten mit Photonen von Rarity und
Tapster sind. Die Analyse zeigt, dass das Erzeugen von individuellen Kollisionszo-
nen in dem Bose-Einstein-Kondensat der vielversprechendste Kandidat ist, um die
Korrelationen zu demonstrieren.

1 Introduction

The smartphones in our pockets, the scanner of a checkout counter when we are shopping, everyday devices such as these, as well as highly advanced medical devices, e.g. nuclear magnetic resonance imaging, are based on the fundamental principles of quantum mechanics. The predictive power of quantum theory has altered everyday life and has had a tremendous impact on today's technology. And yet, 90 years after its inception, its full complexity and toolbox has not been exploited. Quintessential features such as entanglement with all its subtleties embodies a whole new variety of potential revolutions for technological innovations and likewise for evident as well as still concealed mind-boggling fundamental questions. In particular, it is this concept of superposed correlations that holds promises to reveal entirely new solutions in the facets of quantum information and quantum communication and sheds light on how epistomological the world is or how ontic we perceive it.

Even before the mathematical formulation of quantum mechanics by Erwin Schrödinger and Werner Heisenberg, light was the prevailing guide in experiments for this theory into the forefront of modern physics. Thomas Young's double slit experiment and its photonic realizations as well as James Clerk Maxwell's equations on one hand, and the photoelectric effect described by Einstein as well as Planck's quantum hypothesis on the other hand, illuminated the necessity and complimentarity of light being an electromagnetic wave and a photonic quantum at the same time. Nevertheless, with the Schrödinger equation at hand, Louis de Broglie [1] postulated the existence of a similar corpuscule-wave duality for matter, even though matter was genuinely perceived as particle before. Independently, Davisson and Kunsman [2] had already observed then baffling interference effects in diffraction of electrons in nickel crystals. Not only was their work ground breaking for diffraction imaging, but subsequent experiments with neutron interferometry [3–6] and more recently with atoms [7–9] and carbon fullerenes [10] deepened the understanding of fundamental concepts of quantum mechanics. From the time when Schrödinger had formulated his equation governing matter waves, the quantum mechanical repository of tools to understand nature was enriched not only by the particle-wave of light but also by the wave-particle of matter. Within the last century, quantum mechanics has risen to the top of the list of fundamental, exact, and important theories. Its predictions have been demonstrated in many experiments using photons as well as massive particles.

Yet, in 1935 Albert Einstein, Boris Podolsky, and Nathan Rosen (EPR) [11] placed entanglement at the center of a controversy on the completeness of the quantum mechanical theory. Their dissatisfaction with the indeterminism of quantum mechanics led them to conclude that Heisenberg's uncertainty principle [12] and measurement outcomes on entangled systems are incompatible and thus, a deeper theory should exist. Even though their original proposal was discussed in terms of the two conjugate variables position and momentum of two particles, later investigations by

David Bohm [13] translated the argument to spin observables. It was in this framework that John Bell discovered his inequality [14, 15], which, if violated, proofs the existence of the stronger quantum mechanical correlations over the classical ones. In the following decade, Bell's idea excavated EPR's gedankenexperiment and sparked a vivid research in the field of quantum physics [16–20].

In 1982 Aspect et al. [21, 22] performed the first experiment to demonstrate the quantum mechanical correlations beyond classical predictions on a space-like separated system of two photons. Even though they succeeded in selecting the measurement basis on both sides, after the photons were emitted, under strict Einstein locality condition the settings could still have been predetermined. A group of physicists lead by Anton Zeilinger finally closed the locality [23] and freedom of choice loophole [24] by letting a quantum random number generator select the measurement setting in a space like separated fashion so that neither the setting nor the outcome could have been predetermined. As the detection of photons is not efficient, photon experiments have to assume the measured photons to be a fair sample of all photons. Rowe et al. [25] eventually closed what is called the detection loophole by entangling ions in their internal degree of freedom. However, the ions were not space like separated to rule out any kind of signaling, i.e. interaction between the ions. Closing both major loopholes, locality and detection, in either of the systems is an ongoing endeavor [26]. Nevertheless, the features of entanglement are implemented and used in a variety of systems and the expectations for applications of these systems, e.g. quantum computers are skyrocketing [27].

Even though entanglement has been realized in the internal degrees of freedom of systems with massive particles, e.g. ion experiments [25, 28, 29], Josephson junctions [30] and ultra-cold atoms [31–33], the original gedankenexperiment by Einstein et al., employing the external degrees of freedom, has only been realized in experiments with photons. Most prominently, the double-diamond experiment by Rarity and Tapster [34] made use of the low decoherence rate of photons when traveling through space and time.

For matter waves, though, this fundamental experiment has not been realized yet. The strong coupling to the environment causing decoherence and the restriction of particle conservation for matter waves has so far been a significant obstruction in demonstrating the entanglement of the external degrees in matter wave experiments. Nevertheless, with the advent of matter wave lasers, represented by Bose-Einstein-condensed atoms [35, 36], a source of highly coherent matter waves has become available. The experiments, started in the field of matter waves with neutrons and fullerenes, can now start to penetrate into the realm of entanglement. Technological progress, such as precision lasers, highly sophisticated optics, and electronic detection schemes for metastable noble gases, has made possible a variety of experiments on atom statistics.

For example, the prominent idea of Hanbury-Brown and Twiss (HBT) [37] has also been beautifully performed in atomic systems. Discovered in astronomy and used to determine the size of distant stars, the HBT effect looks at correlated intensity fluctuations. Being in a quantum mechanical superposition, the different paths from different spots of the source interfere and the coherence length of the source is recovered in the statistics of bunching photons. In 2005, Schellekens et al. [38] demonstrated the HBT in ultra-cold atomic clouds of metastable helium using a

micro-channel plate (MCP) in combination with a delay-line detector (DLD). The disappearance of the bosonic bunching when the temperature of the cloud crosses the transition temperature to the BEC as predicted in quantum mechanics by Roy Glauber [39–42] was not observed in a rubidium experiment by Perrin et al. [43]. This reveals the more complex structure of an interacting BEC than the one of a laser. The superior detection capabilities of a delay-line detector were essential to experiments by Hodgman et al. [44], where higher order correlation beyond the original photon experiments were shown. While these higher order correlations are the same for photons, Jeltes et al. [45] investigated a property which does not exist for photons and hence shows the importance and prospects of investigations of matter waves in addition to photon experiments. Using again metastable helium, but this time the fermionic isotope helium-3, they could demonstrate the purely quantum mechanical effect of anti-bunching in the case of fermions.

The degenerate Fermi gas [46] is the sister of a BEC and is yet another example where the fermionic nature of certain atoms is paramount. When cooled to degeneracy, the fermionic atoms obey the same statistics as superconductors as described by the BCS-theory, named after physicists Bardeen, Cooper, and Schrieffer. By changing the interaction strength between the fermions, typically by employing a Feshbach resonance [47], molecules of the fermionic atoms can be formed. These molecules, though, compose bosons and hence, a transition between the BCS and BEC can be observed [48]. Dissociating the molecules again yields momentum correlated constituents of the former molecule. Number squeezing of the outgoing modes has been measured [49] and sparked theoretical proposals to perform entanglement experiments, with the external degree of freedom, i.e. momentum of the atoms as the central observable.

In another line of experiments the collisions of atoms were used to generate non-local correlations of matter. Though homodyning of massive particles is challenging, in recent years Gross et al. [32] showed that spin-changing collisions can be used to measure entanglement in atom number and phase of a locally separated spinor BEC. Using specific radio frequency fields to control the interaction of different Zeeman levels of rubidium, and subsequent splitting of the cloud, led to spatially separated correlations between atom numbers. Using again rubidium Bücker et al. [50] used an optimal control scheme to first shake their one dimensional BEC. Subsequent decay under parity conservation populated twin-atom beams with opposite momenta, where they could observe number squeezing as well.

Coming back to helium, there are a number of promising schemes to create entanglement in the external degree of freedom induced by collisions. For metastable helium, the application of a delay-line detector with single-atom sensitivity is superior to investigate momentum correlations after a time of flight (TOF). The collisions follow Hamiltonians equivalent to the spontaneous parametric down conversion (SPDC), which is usually used in entanglement experiments with photons. In 2006, Perrin et al. [51] showed that elastic collisions of two matter waves in a four-wave mixing (FWM) process yield correlations of atoms with opposite momenta as consequence of momentum conservation (back-to-back correlations). In the experiment they showed as well that this spontaneous process contained HBT bunching for atoms scattered into the same direction (collinear correlations). Subsequent data analysis by Kheruntsyan et al. [52] found the back-to-back correlations to outper-

form the collinear ones such that they were even able to violate a Cauchy-Schwarz inequality, ruling out all classical stochastic random variable theories.

An even closer resemblance to the SPDC process in terms of beam profile was demonstrated by Dall et al. [53]. They made use of the different scattering lengths of two Zeeman sublevels, where during collisions the release of mean field energy initiates a momentum kick in an atom pair consisting of one atom of each sublevel. In their analysis of the statistics [54] they found that the bunching of spontaneous scattering disappeared. Given the high densities, they entered a stimulated regime, where phase matching conditions apply, and conical, directed beams as in SPDC were obtained. As a result of the bosonic stimulations, the bunching is suppressed as in the case of an ideal BEC without interactions. The phase matching is of similar nature as superradiance of Dicke states, where light gratings cause atoms to reflect from the grating into collective modes, or equivalently light is reflected from the matter grating [55–57]. After all, while the beam profiles raise the resemblance to SPDC, it is the suppressed bunching statistics that differs for this scheme and makes a proper identification of pairs a severe obstacle.

These exciting advances in atom statistics experiments pioneer the way to investigate the influence of entanglement in matter waves. As demanding as they seem when compared to photon experiments, they also promise access to interesting new realms of physics. Not only does gravity start to play a role for massive particles, but also differences between the Maxwell equations and Schrödinger equation will become addressable. While the Maxwell equations for the relativistic particles have no dispersion in vacuum, the Schrödinger equation naturally causes interference in time as well [58, 59]. This arises from the first order time dependence of the Schrödinger equation. The importance of the vector-characterisitc for electromagnetic waves compared to the scalar form of matter waves can be investigated, as well as their behavior in non-trivial potentials [7, 8]. In addition, the impact of fermionic statistics on entanglement can be addressed uniquely with massive particles.

Besides such fundamental questions, the intriguing application of matter waves for high-sensitivity interferometers is already state of the art for metrology [60–62]. The scale difference of the wavelengths of matter waves and light waves supplies superior precision when realized with similar encompassing areas. Additionally, while quantum metrology in spin systems of atoms has significantly improved its sensitivity employing entangled states, the entanglement of matter waves in their external degree of freedom has not yet been exploited in interferometers.

To pave the way to such still elusive experiments in the realm of matter-wave entanglement, a metastable helium BEC platform has been developed. The system is equipped with a delay-line detector to detect single atom statistics and will facilitate experiments in the succession of the experiments by Perrin et al. The four-wave mixing, applied in their scheme, is in remarkable analogy to SPDC and hence, will be a useful tool for an immediate comparison between matter waves and the successful photon experiments of Professor Zeilinger's group.

This dissertation is outlined as follows: First the system to cool metastable helium to its degeneracy in a BEC is introduced. A variety of steps and a precise control of the atoms along their way is required. First the atoms are brought to their excited state by electron impact in a DC-discharge plasma. Next, laser cooling intensifies the atomic beam, slows it, and eventually traps the atoms spatially. After efficient

transfer into a magnetic trap the atoms can be cooled via evaporation to temperature of $1\,\mu\text{K}$ where the condensation to a BEC occurs. The individual sections are described along with their theoretical background and technical considerations and eventually the emergence of the metastable helium BEC is shown.

The second part of the dissertation focuses on the preparation and detection of the matter waves. A description of the four-wave mixing of two counter-propagating waves will be given. This will include the optical process of Raman transition to initiate the process as well as a schematic of the optical system. As the heart of atom statistic experiments with metastable noble gases a delay-line detector was installed. Its principle and characteristics will be described to give a full overview of the platform.

Eventually, schemes to show entanglement created by the four-wave mixing will be discussed. Extensions to the double-diamond scheme of Horne et al. [63] are discussed in the situation of matter waves. For these schemes, the double double-slit configuration and ghost-interference are presented with their dependence on the size of the source for the atom pairs. To the culmination of the final chapter a practical implementation of the ghost-interference scheme will be considered. One element of this last chapter is to introduce an analytical approach to calculate the expected interference pattern and analyze the feasibility and limitations of such an experiment given the current status of the project.

2 The system to refrigerate metastable helium atoms

To show the counterintuitive phenomena of entanglement in the external degree of freedom of a matter wave there is one major requirement to be able to first create and then detect the entanglement. The initial momentum uncertainty of the source before preparation of a momentum entangled state should be small not to obscure the effects of momentum entanglement. Additionally, different sources should add up coherently. As will be shown later in chapter 4 these two requirements are equivalent. The degree of correlation and thus, the entanglement depends on the coherent volume of the source that is participating in the creation of the entangled matter wave. As the coherent volume becomes smaller and smaller Heisenberg's uncertainty principle omits a good correlation of momenta already in the preparation. However, even though an atomic cloud condensed into a Bose-Einstein condensate (BEC) is only of a few hundred μm down to just a few μm, it still beautifully incorporates this requirement. The quantity defining the coherence length of a single atom as source for a matter wave is given by the de Broglie wavelength λ_{dB} of the atoms. The de Broglie wavelength scales inversely with the square root of the temperature. Thus, an initially colder atomic cloud serves as a better source with larger coherence length for the correlated state. Furthermore, atoms cooled below a certain critical temperature undergo the transition to a BEC. Before condensation they are not only a thermal cloud of ultra cold, but the cloud also consists out of distinguishable atoms. As they all end up in the ground state of the trapping potential, they rather have all a well defined and all the same indistinguishable state. Since atoms in a BEC have low temperatures, i.e. the initial momentum spread, the uncertainty in wavelength is minimal when the process to create momentum entanglement of matter waves is initiated. Furthermore a main signature of a three dimensional condensate of indistinguishable atoms is its large coherence over the whole cloud [64, 65]. So a BEC gives the possibility to start with as small as possible uncertainty in wavelength, with the magnitude precisely controlled in the preparation of the entanglement, while the large coherence volume ensures a well correlated matter wave.

This chapter describes the system to cool metastable helium atoms below the transition temperature and increase the phase space density such that the atoms condense into the BEC. A precise control of various stages is required to prepare the helium atoms in the first excited, metastable state, direct them into the designated science chamber, trap them spatially, and subsequently cool them below the BEC transition temperature. This sequence has to be repeated for every run of the experiment and in the following chapters the individual stages will be described. The stages with focus of this dissertation will all have a theoretical introduction to the underlying principle, describe the realization, and present results about the performance.
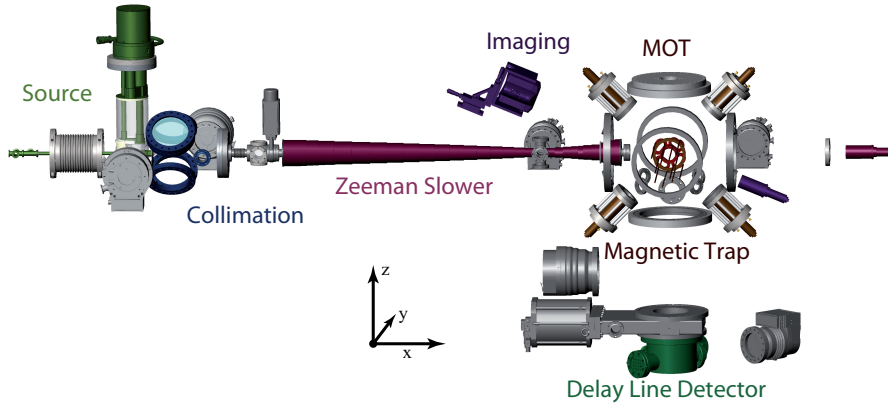
Figure 2.1: An overview of the system. The metastable atoms are produced in the source chamber to the left. Right after the source the atomic beam flux is intensified using laser light in two dimensions to collimate the atomic beam. From there the atoms enter a Zeeman slower, where the atoms are slowed longitudinally to trappable velocities. With this beam a magneto-optical trap is loaded. The trapped atoms are then transferred to a magnetic trap, where they can eventually be cooled below the transition temperature of about $1\,\mu K$ to condense into a BEC. Imaging of the cold atoms by means of absorption imaging is performed a few ms after being released from the trap. Underneath the traps is a delay-line detector DLD mounted to detect the atoms released from the trap. The coordinate system indicates the system used throughout the dissertation. The origin of it is usually placed at the center of the magnetic trap.

The chapter is structured as follows: First the characteristics of helium and its first excited state relevant to this dissertation are presented and the source to produce the excited atoms is briefly sketched. Then a general introduction to the light-matter interaction is given as this interaction is the workhorse to obtain a BEC. This is followed by the arrangement concerned about the preparation of the light. The optical table carrying the optics to lock the laser to the atomic resonance and to prepare all required frequencies is separate from the main optical table carrying the vacuum chamber where the BEC is created. This second table is connected to the main table by glass fibers to deliver the light for manipulation of the atoms. The spectroscopy to generate a reference frequency for the laser is described and the scheme to prepare the frequencies is presented. From there on it will be about the control and manipulation of the metastable atoms.

Figure 2.1 shows the system to give an overview over the stages that will be described in the next sections. Starting from left the source for the metastable helium atoms is followed by a collimation stage to increase the flux of atoms entering the ultra high vacuum chamber[1]. The Zeeman slower decelerates the atoms below the

---

[1]The vacuum chamber between source and Zeeman slower where the collimation of the atomic beam takes place is referred to as "high vacuum chamber". Opposed to this the vacuum chamber where the magneto-optical trap (MOT) is and the BEC is produced is referred to as "science chamber" or "ultra high vacuum chamber". In the science chamber the pressure is

capture velocity of the magneto-optical trap. In latter the atoms are trapped and all further manipulation happens in this place until the atoms are released and dropped upon the delay-line detector underneath the traps. The figure 2.1 has the coordinate system used throughout this dissertation displayed as well. The x-axis is defined by the propagation direction of the atomic beam and the z-axis pointing opposite to gravity. The origin of the coordinate system is placed at the center of the magnetic trap.

2.1 Metastable helium

This section will give an overview of all necessary properties of helium and in particular of its first excited metastable state He* to motivate why this species was chosen and to understand the processes used. In this sense the first subsection provides all essential properties of metastable helium at a glance, which will be found scattered throughout the dissertation again. The second subsection will be a brief description of the source of metastable helium atoms, where they are excited and launched into the experiment. However, the technical realization of the source is not focus of this dissertation and is nicely described in the master thesis of Mateusz Kotyrba [66] and the dissertation of Michael Keller.

2.1.1 Properties of metastable helium

When it comes to laser cooling and ultimately to ultra cold atom experiments the first thought is usually about the alkali metals lithium (Li) [67], sodium (Na) [35], potassium (K) [48], rubidium (Rb) [36], and cesium (Cs) [68]. Their electronic energy level scheme can be significantly simplified as only the valence electron in the outer shell contributes to the light-matter interaction. This electron is well shielded from the nucleus by closed inner shells and thus, behaves in principle like an electron of a hydrogen atom, which is analytically well understood. With this respect alkalis have optical transitions that can readily be accessed for optical manipulation. A different approach is to use the yet more simple noble gas atom helium. Helium is after hydrogen the simplest atom and with its two electron level structure can analytically be calculated. This makes helium interesting as a candidate to investigate models beyond the simple hydrogen atom, but because of the two electrons lying on a closed shell, its only optical transitions lie in the deep ultraviolet spectrum. Lasers with these wavelengths are hard to produce and make helium in its ground state a difficult candidate for laser cooling. However, if one electron is excited from the core to a higher lying state, there exist states that are long lived, such that the lifetime of the excited state is well above any experimental time scale.

For this experiment helium atoms are excited to the lowest lying excited state 2^3S_1. This triplet state is the longest lived state as well as the most energetic of all first excited states within the whole periodic table. The selection rule $\Delta L = \pm 1$ forbids the transition to the ground state 1^1S_0. As the spin of one of the two electrons needs to flip for this transition to occur the process is doubly forbidden and gives a lifetime of about $8000\,\text{s}$ [69]. Thus, this metastable state can serve as virtual ground
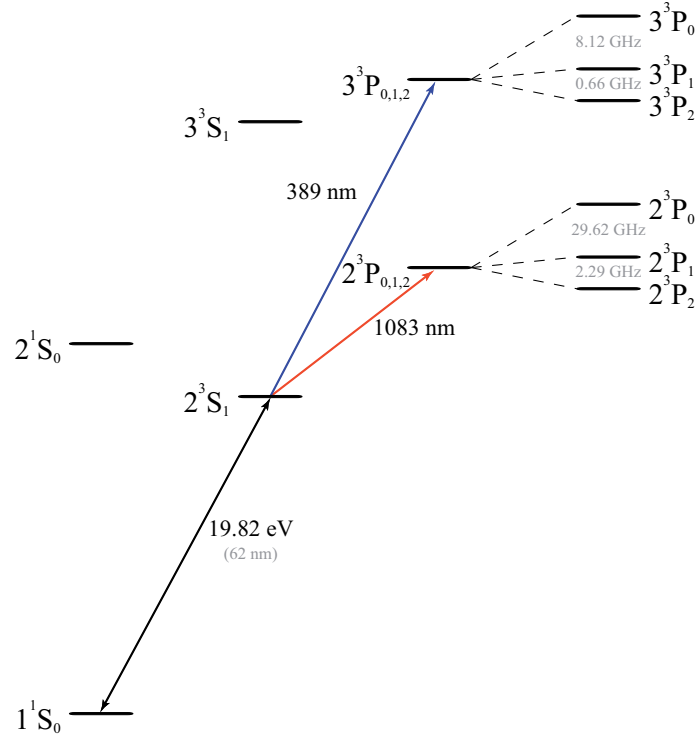
---

below $10^{-10}\,\text{mbar}$

Figure 2.2: The energy levels of helium. It is hard to excite from the electron from its ground state 1^1S_0. However, once brought to the lowest lying triplet state 2^3S_1 this can serve as virtual ground state for experiments. This state has optical transitions to the 2^3P- and 3^3P-manifolds, which can be used for optical manipulation. The high internal energy of $19.82\,\text{eV}$ can be used for detection.

state and now provides not only two optical transitions, but also has an internal energy of 19.8 eV. Fig. 2.2 shows the energy levels relevant for this dissertation. The transition from the 2^3S_1-state to the 2^3P-manifold is at $1083\,\text{nm}$ with linewidth $^{1083}\Gamma = 2\pi \cdot 1.62\,\text{MHz}$ and saturation intensity $^{1083}I_s = 0.16\,\text{mW/cm}^2$ while the transition to the 3^3P-manifold occurs at $389\,\text{nm}$ with linewidth $^{389}\Gamma = 2\pi \cdot 1.49\,\text{MHz}$ and saturation intensity $^{389}I_s = 3.31\,\text{mW/cm}^2$.

The high internal energy of metastable helium makes it possible to electronically detect single atoms with micro-channel plates (MCP)[2]. Upon collision with the walls of the channels the excited atoms release their internal energy and eject electrons out of the walls. Subsequent acceleration of the electrons in high electric fields launches an avalanche in the channels until a decent electronic signal is produced and can be recorded. This is the true advantage of a metastable noble gas species over the alkali metals, where only in recent experiments single particle detection has become available as well [70]. However, the single particle detection of alkali still relies on optical detection, which is limited by long integration times and low flux' of atoms.

While the high internal energy is an advantage of the metastable species in detection, it poses a severe challenge during the preparation of ultra cold samples. Just

---

[2]A more detailed description of MCP detectors is given in chapter 3.2

as the internal energy is released upon collision with the walls of the MCPs during detection, the internal energy is released as well upon collision of a metastable atom with another atom. The consequence is that the collision partner is ionized, while the metastable helium atom is deexcited (Penning ionization) [71]. The partner in the collision can carry away the spin set free by the relaxation of the triplet electron to its real ground state. The metastable atom thus, can return to the real ground state, i.e. the atom is lost for any further manipulation and observation. The Penning ionization only allows for small densities when the atoms are spatially trapped in the MOT and already limits the starting conditions for any step afterwards. Only when the atoms are loaded into a magnetic trap and the sample is spin polarized the Penning ionization can be significantly be suppressed [72]. This suppression is strongest for the ^{4}He isotope, as it has no nuclear spin which could take up as well the excess spin of the electrons participating in the ionization process. Besides the relatively large positive scattering length of $a_{11} = 7.5$ nm [73] for helium, only this strong suppression made it possible to achieve the densities required for the degeneracy of BEC gas and still poses the major challenge for any other metastable species, e.g. neon [74].

The fact that ^{4}He has no nuclear spin and therefore, no hyperfine splitting occurs, has its consequences for the cooling scheme as well. No hyperfine splitting means that no re-pumping is required for laser cooling in order to maintain a closed cycle transition, which reduces the number of required frequencies. However, it should be mentioned that no hyperfine splitting also means, there are no internal states that can be easily used for quantum coherent operations in the radio frequency (rf) spectrum, especially no isolated clock transitions exist.

Due to the two closed optical transitions, metastable helium can be laser cooled at the fairly accessible near UV and near IR wavelengths. However, the small mass of helium $m = 6.64 \cdot 10^{-27}$ kg means that small thermal, and as such kinetic energies, still correspond to relatively high velocities. Therefore, slowing helium atoms by optical means requires considerably more space than slowing alkali metals. Moreover, helium atoms need to be excited to the metastable state (He*) by non-optical means, which cause additional heating of the gas. The stage for this process will be described in the next subsection.

2.1.2 The source for metastable helium

In the preceding subsection it was described how the elementary properties of He* can come in as a benefit for laser cooling and especially for detecting single atoms. On the other hand, this comes at the expense of an extra step when producing the excited atoms. The atoms need to be excited to the metastable state and the extremely long lifetime of the desired state excludes optical means to selectively excite the atoms (not to mention the difficulty to produce a laser with a wavelength at 62 nm). Nevertheless, there are ways to perform this excitation. In chapter 2.3 it will be described how an rf antenna can be used to create a plasma of a helium gas, where some fraction of the atoms is in the excited state. This scheme however requires a low density of atoms and is counterproductive when a high flux source of He* for loading a MOT is desired. A solution for higher flux and continuous output is the supersonic cold cathode discharge source. Fig. 2.3 depicts the principle. Ultra
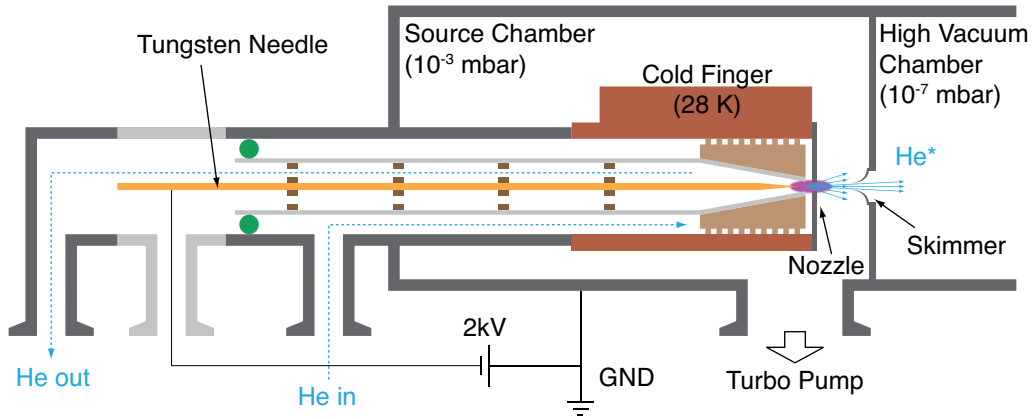
Figure 2.3: The schematic of the metastable helium (He*) source. Ultra pure helium enters the vacuum system and is cooled to 28 K by contact cooling with a cryostat. Before being pumped out again it passes a high voltage needle electrode (2 kV). The discharge of this electrode produces a plasma of helium in which a fraction ends up in the first excited state and enters into the high vacuum chamber. Courtesy of Michael Keller.

pure helium (99.9999%) enters the vacuum system (3 mbar inlet pressure). The gas flows between a glass tube and the outer vacuum chamber to the cold finger. The cold finger is held at 28 K to precool the helium from room temperature to almost its freezing point by contact cooling[3]. Afterwards the gas enters into a strong electric field between a tungsten needle and the nozzle separating this section from the high vacuum chamber. Most of the gas flows back through the glass tube and is pumped out of the system. However, some of the atoms are torn apart and create a plasma. Through various cascades a fraction of about 10^{-5} ends up in the lowest lying excited state 2^3S_1. The nozzle has an orifice, which gives way for some atoms to supersonically expand into the high vacuum chamber (10^{-9} mbar when the helium inlet is closed and 10^{-7} mbar when operating).

The helium is pumped through the vacuum system by an ACP28 by Pfeiffer Vacuum. The same pump is used as backing pump ($3 \cdot 10^{-2}$ mbar when the helium inlet is closed and $3 \cdot 10^{-1}$ mbar when operating) for the turbo pumps ($2\times$ HiPace400, Pfeiffer Vacuum) at the following high vacuum chamber. The cold finger is cooled by a cryostat VT4-500 by Vericold (now Oxford Instruments) and the high voltage (2 kV @ 2.1 mA) between the needle and the orifice is maintained by an Iseg HPn 60-506 power supply.

To prevent the gas from flowing directly to the outlet and not passing the discharge region o-rings seal this path. The tightness of these rings is crucial for the performance of the source and care has to be taken that no discharge other than the one between needle and orifice happens. Even though helium with high purity is used, some nitrogen always enters the chamber and is collected by the cold finger. To remove this load from the cryostat the cold finger is heated up to 60 K every night when no experiments are run. The source can be operated for longer periods of time.

---

[3]Note that the atoms are not yet in the excited state. Hence, collisions with the wall are purely elastic and lead to cooling of the gas.

However, after a couple of days the source will freeze and no output is generated anymore.

Behind the orifice is a skimmer to extract a pre-collimated atomic beam from the source region. With this system an output of a few times $10^{-14}\frac{atoms}{\mathrm{sr}\cdot\mathrm{s}}$ is achieved at a peak velocity of about $800\,\mathrm{m/s}$. This is a comparatively high output for the corresponding velocity and gives a good starting point for the laser cooling process. Further analysis of the source can be found in ref. [66].

2.2 Interaction between light and matter

Throughout this dissertation the interaction between light and matter is of crucial importance, may it be for locking the laser to the optical transition of helium, for cooling the atoms, or to prepare the entangled state of two collided atoms. In this section the fundamental principles underlying these interactions is briefly described. First the concept of the Rabi two level approach to understand the interaction is introduced. This is directly applicable to the situation when the two Raman light pulses prepare the atoms of the BEC in a superposition of counter-propagating wave packets for the four wave mixing process in chapter 3.1. However, this is the concept building the foundation for all other interaction as well. The subsequent sections will thus, make use of it, when the absorption of light will be discussed. The last subsection concludes this theoretical overview by discussing how this interaction of light and matter can eventually lead to cooling of atoms by means of light.

2.2.1 The Rabi two-level concept

A general approach to the interaction between light and matter is to start with a perturbative ansatz, described by the time-independent atomic Hamiltonian $\mathcal{H}$ and a broad perturbation $\mathcal{H}'$ for the interaction. However, this can become complicated for it takes all eigenstates of the unperturbed system into account. The broad perturbation accepts all possible wavelengths and hence, all eigenstates can in principle be excited and participate in the interaction. A more straight forward approach for atom optics was formulated by Rabi [75, 76], where a narrow linewidth laser can individually couple only two states[4]. This reduces the problem to two coupled differential equations for the complex population probability amplitudes $c_{e,g}$ of the two concerned levels $|e\rangle$ and $|g\rangle$, respectively [77, 78][5]

$$i\hbar\frac{dc_g(t)}{dt} = c_e(t)\mathcal{H}'_{ge}(t)e^{-i\omega_A t} \tag{2.1}$$

$$i\hbar\frac{dc_e(t)}{dt} = c_g(t)\mathcal{H}'_{eg}(t)e^{i\omega_A t}$$

where $\hbar$ is the reduced Planck constant, ω_A the atomic transition frequency between the levels, and $\mathcal{H}'_{ge}$ the perturbing Hamiltonian reduced to the two level problem. As the strongest interaction happens when the laser frequency ω_L is close to the

---

[4]Even though for the interaction of matter with light the formulation is semantically restricted to laser light, the formulation is applicable to all electromagnetic fields

[5]Most of the discussion in the section follows the book of Metcalf and van der Straten.

transition frequency ω_A the problem simplifies when entering a frame co-rotating with the laser wave (rotating wave approximation). This way terms of the order $1/\omega_L$ can be neglected compared to terms of the order $1/(\omega_L - \omega_A) = 1/\delta$, where the detuning δ between the laser and the atomic resonance is introduced. Additionally, one assumes the spatial variation of the electric field to be small compared to the spatial extension of the electronic wave function around the atom and the electric dipole to be parallel to the electric field (summed up in the electric dipole transition). A reasonable assumption, as in a two level system the electron can just follow the electric field (this can vary for a multi level problem) and the extent of the field ($\sim 500\,\mathrm{nm}$) and the electronic wave function[6] ($\sim 1\,\mathrm{nm}$) typically differ by two orders of magnitude. For a plane laser wave this results in an interaction Hamiltonian $\mathcal{H}'_{ge}(t) = \hbar\Omega \cos(\omega_L t)$, where the vacuum Rabi frequency Ω is used

$$\Omega = -\frac{E_0}{\hbar} e \cdot \langle e|r|g \rangle \tag{2.2}$$

The dipole matrix element $e \cdot \langle e|r|g \rangle$ can be difficult to calculate, but with the linewidth Γ of the transition known it has the simple form

$$e \cdot \langle e|r|g \rangle = \sqrt{3\pi\epsilon_0 \hbar \lambda^3 \Gamma} \tag{2.3}$$

Where ϵ_0 is the vacuum permittivity. With this the two population probabilities can be decoupled and it can be seen that the populations oscillate at the reduced Rabi frequency $\Omega' = \sqrt{\Omega^2 + \delta^2}$

$$c_g(t) = \left(\cos\left(\frac{\Omega' t}{2}\right) - i\frac{\delta}{\Omega'} \sin\left(\frac{\Omega' t}{2}\right) \right) e^{i\delta t/2} \tag{2.4}$$

$$c_e(t) = -i\frac{\Omega}{\Omega'} \sin\left(\frac{\Omega' t}{2}\right) e^{-i\delta t/2}$$

These equations demonstrate how a resonant laser can drive the populations of a two level system coherently into each other. An extension of this is the basis for coherent population transfer to create the counter-propagating matter waves in chapter 3.

However, the calculation only holds as long as the off diagonal matrix elements of the perturbing Hamiltonian vanish. In particular for high laser intensities and large detunings it can be shown, that the eigenstates of the unperturbed Hamiltonian are no longer eigenstates of the perturbed Hamiltonian. The new eigenstates of the perturbed system are shifted due to this ac-Stark shift from the unperturbed eigenstates by

$$\Delta E_g = +\frac{\hbar\Omega^2}{4\delta} \tag{2.5}$$

$$\Delta E_e = -\frac{\hbar\Omega^2}{4\delta}$$

This result is of particular interest when atoms are trapped by purely optical means [79–81]. As the shift is proportional to the laser intensity, optical traps can

---

[6]Even though the atomic wave function can extend over μm the electronic wave function remains localized around the atom

be formed with laser beams tailored such, that a three dimensional local maximum of the intensity exists. In chapter 2.8 it will be discussed how such a trap could be realized in the existing setup. From a point of view of a matter wave experiment it is even more interesting that such an energy shift due to off resonant laser light can introduce a phase shift for matter waves propagating through this field [8, 9]. This possibility will be illuminated in chapter 4 when entanglement between the atoms in their external degree of freedom is discussed.

2.2.2 Absorption and radiative force

While the Rabi two-level concept elegantly describes the evolution of populations in the electronic states of an atom when the laser can coherently manipulate the atom, in most situations decoherence interrupts this eternal play. An excited atom left by itself decays with finite lifetime $\tau_a = 1/\Gamma$ back to the ground state in a spontaneous process. Spontaneous emission is not considered in the Rabi oscillations. However, this predominantly happens when a laser passes through a gas of atoms. The excited atoms do not only couple to the laser light field but can emit the light into all possible vacuum modes surrounding the atoms. The problem of decoherence is usually encompassed in a density matrix approach. This concept applies in the case of spontaneous emission as well and leads in the two level system to the so called optical Bloch equations. The steady state solution for the population difference of the two levels involved $\Delta\rho = \rho_{gg} - \rho_{ee}$ holds the saturation intensity I_s to characterize the system

$$\Delta\rho = \frac{I_s(1 + (2\delta\,\Gamma)^2)}{I + I_s(1 + (2\delta\,\Gamma)^2)} \tag{2.6}$$

where I is the intensity of the laser. The saturation intensity defines the intensity at which the population difference is $1/2$ and further increase of the laser intensity does not result in a significantly larger population of the excited state but rather broadens the spectrum of absorption. Thus, the population of the excited state is given by

$$\rho_{ee} = \frac{1}{2}(1 - \Delta\rho) = \frac{1}{2}\frac{I/I_s}{1 + I/I_s + (2\delta/\Gamma)^2} \tag{2.7}$$

As no more atoms can be excited some will be stimulated to emit back into the light field. The result is a shorter lifetime for the atoms in the excited state and leads to a power broadened linewidth of the absorption spectrum

$$\Gamma' = \Gamma\sqrt{1 + I/I_s} \tag{2.8}$$

As the laser travels along its way through the gas more and more excited atoms spontaneously decay into other modes and the photons are lost from the laser intensity. This fact is central to spectroscopy and follows the Beer-Lambert law for intensities smaller than the saturation intensity

$$I(z) = I_0 e^{-\sigma n z} = I_0 e^{-OD z} \tag{2.9}$$

where n is the density of atoms, $\sigma = 3\lambda^2/2\pi$ is the scattering cross section, and OD the parameter describing the concept of optical density.

As in every physical process energy needs to be conserved as well as momentum. The absorbed photon thus needs to transfer its momentum to the atom. If the atom now spontaneously emits the photon into an incoherent mode, i.e. not back into the laser mode again, the momentum of the atom before and after the interaction with the light has changed. The direction of the spontaneous emission is random and the average of the various direction cancels the momentum kick exerted by the emission and only the momentum kick from the absorbed photon remains. From the Ehrenfest theorem follows that the radiative force on the atom by a large number of photons is simply the momentum of the photons times the scattering rate and the probability to be excited

$$\vec{F}_r = \hbar \vec{k}_L \cdot \Gamma \cdot \rho_{ee} = \hbar \vec{k}_L \cdot \frac{1}{2} \frac{I/I_s}{1 + I/I_s + (2\delta/\Gamma)^2} \tag{2.10}$$

where the momentum of photons is defined over the wave vector of the laser $\vec{k}_L$. From eq. (2.10) it is clear that the maximal force of $\hbar\vec{k}_L\Gamma/2$ can only be reached if the laser is always on resonance with the atomic transition.

The analysis so far treated the atom always at rest. However, when it comes to cooling atoms by means of laser light the atoms are, at least at the beginning of the process, moving and upon interaction with the light change their velocity $\vec{v}_A$. Atoms moving relative to the laser experience a Doppler shift

$$\delta_D = -\vec{k}_L \cdot \vec{v}_A \tag{2.11}$$

In the chapters concerned with slowing and trapping of atoms it will be discussed in more detail how this problem can be compensated experimentally. A closer look at the level structure of atoms reveals another parameter to adjust the detuning. Most energy levels have a magnetic degeneracy, which can be lifted by external magnetic fields $\vec{B}$

$$\Delta E = m_J \vec{\mu}_{eff} \cdot \vec{B} \tag{2.12}$$

where m_J[7] is the magnetic quantum number to the total angular momentum $\vec{J} = \vec{L} + \vec{S}$, consisting of the orbital angular momentum $\vec{L}$ and electronic spin $\vec{S}$. The magnetic moment $\vec{\mu}$ can be calculated from the Landé g-factor g_J of the respective state and Bohr's magneton μ_B

$$\vec{\mu} = g_J \vec{\mu}_B \approx \left(\frac{3}{2} + \frac{S(S+1) - L(L+1)}{2J(J+1)} \right) \vec{\mu}_B \tag{2.13}$$

So the total detuning of the laser light from the atomic resonance is given by

$$\delta = \omega_L - \vec{k} \cdot \vec{v} - \vec{\mu}_t \cdot \vec{B}/\hbar - \omega_A \tag{2.14}$$

---

[7]As ^{4}He does not have a nuclear spin all effects are discussed in the terminology using J as well-defined quantum number. For atom species with nuclear spin $\vec{I}$, e.g. ^{3}He this is not valid anymore. However, the principle stands and can be extended by replacing $\vec{J}$ with the total spin $\vec{F} = \vec{I} + \vec{J}$

where $\vec{\mu}_t = \vec{\mu}_e - \vec{\mu}_g$ is the magnetic moment of the transition between the excited and ground state with effective magnetic moments $\vec{\mu}_e$ and $\vec{\mu}_g$, respectively.

It should be mentioned that due to the spontaneous emission process as inherent part of the radiative force there is a fundamental limit to the minimum speed that can be achieved when the radiative force is used to slow atoms. Even if the atom is perfectly at rest after the absorption of the photon the subsequent emission is random, i.e. cannot be pre compensated for, and imprints a momentum kick on the atom again. This last photon transfers a momentum of $\hbar k_L$ and defines with the mass m of the atom the so called recoil velocity[8]

$$v_{rec} = \frac{\hbar k_L}{m} = 92.1 mm/s \tag{2.15}$$

This is generally regarded as the lower limit for laser cooling processes. However, this would require a knowledge of when the atom has just absorbed the last photon and an immediate switch off of the laser is required. In most cooling schemes though, the laser light is a strong coherent field that acts on an ensemble of atoms. Thus, this one to one knowledge of the last photon for a single atom in order to reach the recoil limit is in most cases not available. The atoms rather have to get out of resonance with the laser, which happens when the Doppler detuning is on the order of the linewidth of the transition. This defines the so called Doppler limit applicable to most cooling schemes:

$$v_D = \sqrt{\frac{\hbar \Gamma}{2m}} \tag{2.16}$$

with the equipartition theorem and the Boltzmann constant k_B this can be expressed in terms of a temperature:

$$T_D = \frac{\hbar \Gamma}{2k_B} = 38.9 \mu K \tag{2.17}$$

With this the most basic concepts of the light-matter interaction are introduced and this section will be pulled up whenever a fundamental equation is required.

2.3 The optical setup for laser cooling

The preceding section gave a theoretical overview to the interaction of light and matter. This interaction plays a crucial role in the experiment as the narrow linewidth of a laser gives enormously precise control of single atoms [82, 83] or as in the case of this dissertation of an ensemble of atoms. Nevertheless, in order to make use of this interaction the laser has to be well referenced to the atomic resonance. In this section the laser system at hand is described. First two principles to lock a laser to an atomic transition are described. While the polarization spectroscopy is relatively easy to set up, its drawback is its susceptibility to birefringence and magnetic fields. The saturation spectroscopy on the other hand requires a small electronic overhead in order to lock the laser to the center of the transition, but is less coupled to the

---

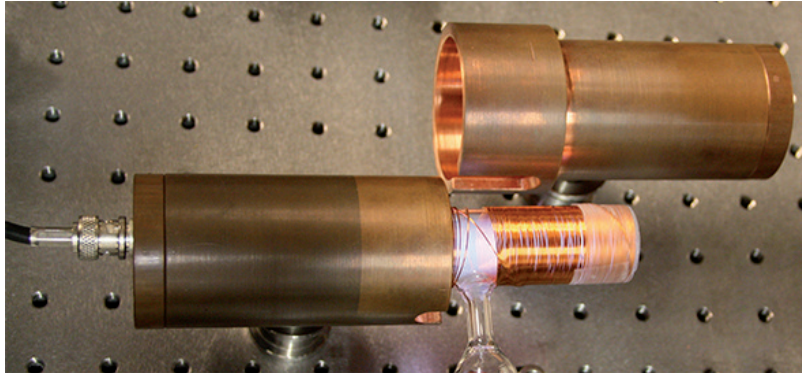[8]The values given here refer to the 2^1S-2^3P transitions of helium

Figure 2.4: To produce a reference frequency for laser cooling helium is continuously pumped through a glass cell. An rf antenna ignites a plasma to produce metastable atoms. A μ-metal shields the atoms in the cell from the environment and the copper Faraday cage shields electronic equipment from the rf.

environment and thus, serves to greater extent as an absolute reference. The last subsection explains the design of the optical table, where all various frequencies are generated that are needed throughout the experiments.

Central to both spectroscopy methods is a reference sample of the atoms to which the laser should be locked to. The noble gas species helium is at room temperature already in the gas phase. However, it is not in the excited state which will be subject to the laser manipulation. This excitation however, can be accomplished by a strong rf field generated by an antenna around the cell. The rf induces a plasma in the cell which contains some metastable atoms. Yet, the plasma is very reactive and cleans effectively all dirt of the walls [84]. Once the walls are clean the dirt mixes with the gas and the excited atom transition is quickly quenched to non-existence through collisions with other atoms and molecules [85]. This process made all reference cells that were commercially available lose the spectroscopy signal within minutes. In principle, the cell can be cleaned properly by super strong plasmas before hand. However, the process is delicate and the project of this dissertation uses the approach to continuously pump the dirt out of the cell. This open system is also continuously filled with helium gas such that a steady state pressure of about 0.1 mbar is maintained. The pressure is crucial for the number of atoms. The best signal is obtained at the mentioned pressure. However, this leads to a collision broadening of the transition of about 20 MHz. Fig. 2.4 shows such a cell with the plasma ignited. Around the cell is the antenna wrapped to ignite and maintain the plasma. To shield the gas from external magnetic fields a μ-metal is placed around the cell and to shield the electronic equipment from the rf a Faraday cage made out of copper encapsulates the whole arrangement. The rf source runs at 25 MHz and can be turned up to 5 W power to ignite the plasma. However, in operation this is usually reduced to about 100 mW to minimize the noise on the signal.

2.3.1 Polarization spectroscopy

To make use of the sharp linewidth of a laser to manipulate atoms it is absolutely necessary to have the laser frequency resonate with the atom's transition. For this purpose the spectroscopy cell is used as a reference in order to lock the laser to the transition. The laser passing through the cell is attenuated depending on the relative detuning $\delta = \omega_A - \omega_L$ between the atomic transition frequency ω_A and the laser frequency ω_L (compare eq. (2.9)). On resonance, $\delta = 0$, the absorption is strongest.

The width of the atomic transition is determined by four processes which all add up. The natural linewidth is due to the finite lifetime of the excited state of the atom without any external perturbation and poses an ultimate limit on how narrow the linewidth can be.

Collisions among the atoms and other residual gas atoms lead to shifted levels and de-excitation of the atoms. This reduced lifetime of the excited state and the shifted levels manifest themselves in a collision-broadened linewidth. The effects of this broadening can be minimized by lowering the pressure in the cell. However, smaller pressure is equivalent to less atoms and thus, less signal. So there is an optimum at which signal strength and linewidth have tolerable extents.

The third broadening is caused by the laser probing the gas itself. Depending on the intensity of the laser the emission of photons from excited atoms is induced by the laser. This again shortens the lifetime and increases the linewidth (compare eq. (2.8)). This contribution is minimized by operating the laser as far as possible below the saturation intensity.

Lastly, the biggest contribution stems from the doppler broadening. This is not caused by a reduced lifetime, but originates from the different velocities existing in the thermal gas. The atoms in the gas have all different velocities, following a Boltzmann distribution with the temperature as the parameter to determine the width. Each atom thus experiences a different doppler shift δ_D depending on its velocity with respect to the laser propagation and resonates at different frequencies with the laser.

Doppler-broadening can be elegantly eliminated completely by means of Doppler-free spectroscopy. For this method a second laser counter-propagating with the original probe laser has a high intensity to excite the atoms and saturate the transition. The counter-propagating direction of the so called pump beam has the effect that only atoms at rest interact with both lasers at the same frequency and the high intensity of the pump laser "burns" a hole into the gas of absorbing atoms, i.e. into the absorption spectrum of the probe laser. The resulting profile shows a dip within the Doppler-broadened signal, which is only limited by the natural lifetime, the collision-broadening, and the power-broadening.

The doppler-free absorption profile is the basis for all locking schemes. However, stable locking of a laser to the center of a transition of an atom is only possible with a dispersion-like signal, i.e. a monotone slope around the locking-point. One way to generate such a dispersion-like signal is by introducing a birefringence in the gas. A σ^+-polarized pump beam only saturates the σ^+-transition (assuming this kind of transition exists see fig. 2.5). Thus, a linearly polarized probe beam, decomposed in its two circular polarizations, experiences a differential refractive index [86]. The result is an elliptical and rotated probe beam at the exit of the gas cell. Placing a
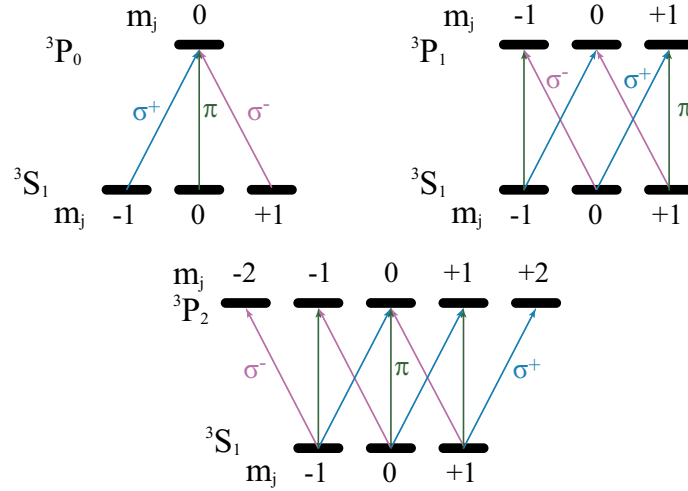
Figure 2.5: Optical dipole transitions for the first excited states $^3P_0$, $^3P_1$,and $^3P_2$ from the metastable state $^3S_1$. The $^3P_0$-state does not have magnetic sublevels and hence, does not support $\sigma^{\mp}$-transitions for closed cycles.

half wave plate (HWP) and a polarizing beam splitter (PBS) further down the beam to measure the two components under 45° to the original polarization, gives direct access to a dispersion signal centered around the center frequency of the transition and any offset, e.g. from laser noise, is eliminated by subtracting those two signals. Fig. 2.6 shows a scheme of the setup for this technique and a signal obtained by it.

This method is easy to implement and does not require sophisticated electronics to generate an appropriate error signal. No modulation of the laser broadens the laser linewidth nor an additional optical modulator needs to be placed in the spectroscopy. The detectors do not need to have a high bandwidth and can provide a strong signal. However, there are two factors that make polarization spectroscopy sensitive to fluctuations in the environment. The implemented scheme to eliminate the offset assumes equal transition frequencies for σ^+- and σ^--light. This is only guaranteed in the absence of any magnetic field. Secondly, the original polarization of the probe beam has to be known and stable. Thus, smallest fluctuations caused by any additional birefringence can lead to a shift of the signal. Both effects can be challenging to control and render the main disadvantages of this technique.

2.3.2 Saturation spectroscopy

Due to the simplicity of the polarization spectroscopy, this technique was used without any problems until the stage of the magnetic trap and even the BEC could be realized. However, in order to achieve long lifetimes in the magnetic trap with the trap bottom at only a few Gauss the atoms need to be well shielded from any resonant light. This required to completely enclose the optical table, prohibiting a proper temperature stabilization. At this stage long term drifts in the spectroscopy could be observed, as the glass of the spectroscopy cell exhibits temperature dependent birefringence. This subsection describes a spectroscopy technique that overcomes these external influences by deriving the dispersion signal from a beating with it-
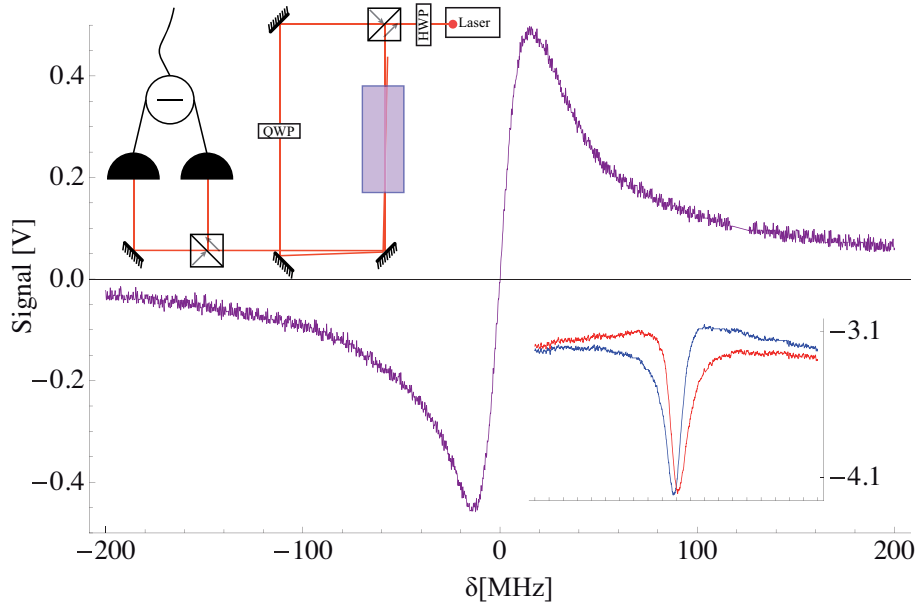
Figure 2.6: A dispersion like signal can be obtained by polarization spectroscopy. Central components are a circularly polarized pump beam and a polarization sensitive detection.The insets show the schematic of the setup and the signals obtained from the individual detectors, which are subtracted from each other.

self. Moreover, this technique does not require a specific level structure as does the polarization spectroscopy, which relied on a σ^+-transition. So the laser to drive the Raman-transfer to initiate the two counter-propagating matter waves has to apply this technique in order to use the $^3P_0$ (see chapter 3.1).

The idea behind this is to take the Doppler-free absorption profile and by modulating the laser frequency the derivative can be obtained. Modulating the laser frequency, either by means of the frequency of the laser itself or by introducing an electro-optical modulator (EOM) into the laser beam, results in sidebands of the carrier frequency. The individual side bands experience a phase shift with opposite sign, depending on which side of the absorption peak the bands are, and an interference between the carrier and the sidebands can be observed in the beating signal. Thus, by mixing down this signal again a strong signal with steep slope at the center of the peak can be obtained. This approach has its beauty in two effects: firstly, the signal is independent of any constant offset and automatically centers around the peak; secondly, the detection happens at higher frequencies, and as such operates at a level where the $1/f$-noise has dropped significantly.

In principle there are two regimes of frequencies to modulate the laser with. One is at frequencies smaller than the linewidth, called lock-in (typically some ten kHz). This requires lower modulation frequencies, and is less demanding in terms of bandwidth for the detectors. However, typically filters are used to reduce any residual $1/f$-noise from the signal and can cause an unwanted phase between the input signal and error signal generated at the output. The second regime operates at much higher frequencies than the linewidth (some ten MHz) and is called after physicists
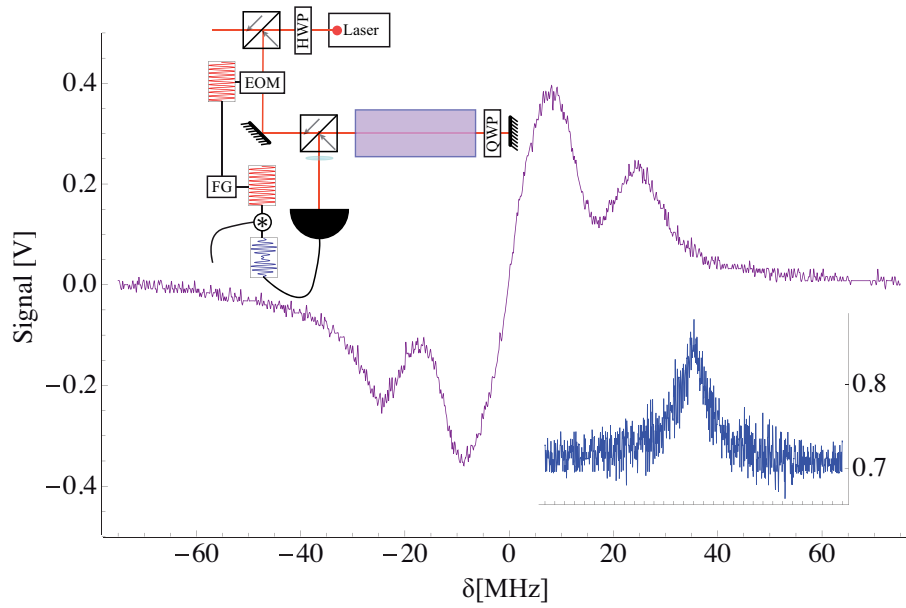
Figure 2.7: The derivative of the Doppler-free absorption spectroscopy can be obtained by phase-modulating the laser light. Central is the EOM (4004-M, Newport) to phase modulate the laser beam introducing sidebands and a high bandwidth photodetector (Balanced Photoreceiver 1817FS, Newport). Mixing down the beating signal reveals an interference between carrier and sidebands, which is proportional to the derivative of the signal around the absorption peak. The insets show the schematic of the setup and the signal of the detector before demodulation.

Robert Vivian Pound, Ronald Drever, and John Lewis Hall Pound-Drever-Hall-locking (PDH). PDH requires neighboring absorption peaks to be well separated and is typically used for locking of optical cavities. However, the fine structure splitting of He* is on the order of GHz and thus allows for this technique to work. Fig. 2.7 shows a scheme of the setup for this technique and a signal obtained by it. An electro-optical modulator (EOM) makes use of the Pockels effect to modulate the refractive index of its crystal. This way a broadening of the laser itself and high modulation frequencies can be achieved. To deconvolute the signal again the signal is mixed down by the modulation frequency in PDD100-module of Toptica.

2.3.3 The optical frequency preparation

A fiber laser (Adjustik-Y10-10, Koheras) is the workhorse for laser cooling the metastable helium atoms. An input of $1\,\mathrm{mW}$ input power is required to saturate a $5\,\mathrm{W}$ fiber amplifier (KPS-CUS-BT-YFA-1064-SLM-PM-50-110-CO, Keopsys). The rest of the fiber laser light can be used for the spectroscopy with which the laser is locked to the atomic resonance of the 2^3P_2-transition by the PDH-scheme. Fig. 2.8 shows the arrangement to generate the frequencies required for cooling. About $3\,\mathrm{W}$ of the amplifier is used to prepare light for the collimation stage, the Zeeman slower, the MOT beams, and for spin polarization as well as imaging. The frequencies
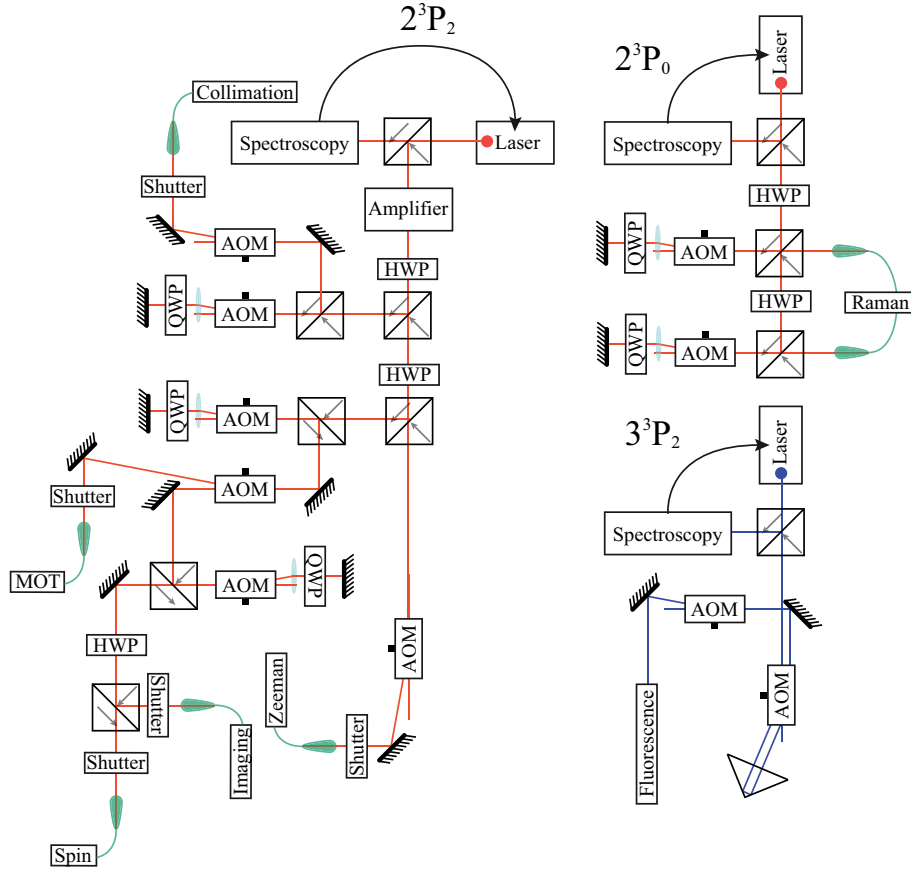
Figure 2.8: The schematic of the optical table. Laser cooling is done by a fiber ampli-
fied fiber laser at 1083 nm locked to the 2^3P_2-transition. A second laser at
1083 nm is locked to the 2^3P_0 transition for the Raman transitions that
prepare the atom in the BEC in two counter-propagating matter waves.
For a fluorescence detection a third laser can be set up. Produced in a
second harmonic generation setup the laser at 389 nm (3^3P-manifold) is
a convenient tool that can easily be detected by CCD cameras, e.g. to
characterize the collimation or Zeeman slower stages.

are shifted by acusto-optical modulators (AOM), where an rf signal is transduced
into a sound wave in a crystal. The light is Bragg-reflected from the sound wave
and depending on the incident angle either picks up the momentum of the phonon
$\hbar k_{phonon} = h/\lambda_{rf}$ or loses one quanta of phonon momentum. To be able to tune the
frequencies most stages have one double-pass configuration of an AOM. This way
the angle dependence on the frequency can be reduced.

Various AOMs from Brimrose, Isomet, and Intraaction are used to shift the fre-
quencies in the optical setup. While Brimrose AOMs are the most compact ones,
Intraaction AOMs are the most convenient ones to align. In performance they do
not differ much when operated at the designed rf power.

The collimation stage consists of a double-pass AOM at ~ -40 MHz and one
single-pass AOM at 80 MHz to shift the frequency back to the resonance. The light
is then coupled to a polarization maintaining fiber (PM) and sent over to the vacuum

system. Of the initially 250 mW at the beginning of this stage 50 mW come out of the fiber and are used for collimating the atomic beam.

The Zeeman slower has only one AOM at -370 MHz. The high detuning is not very efficient and therefore, it is more favorable to tune the magnetic field of the Zeeman slower by changing the current there. About 400 mW is required at this stage to produce 90 mW of PM-fiber coupled light.

The MOT stage requires most of the power. About 2.4 W impinges on a double-pass AOM set to $\sim -2 \times 40$ MHz. A second AOM at 40 MHz shifts the frequency back to the required frequency for the MOT. This AOM is turned off when the MOT is not used and spin polarization, 1D-cooling, or imaging is turned on. This way the zeroth reflection-order is strongest and the light from the double-pass AOM in this order can be used for either spin polarization, 1D-cooling or imaging.

The MOT light is then coupled into a PM-fiber and sent to a fiber cluster[9] (Fiber Beam Port 2to6, Schäfter und Kirhchoff), where the light is split evenly into six plus one PM-fibers. Eventually 40 mW per laser beam is used for the MOT.

For spin polarization, 1D-cooling and imaging another AOM in double-pass configuration shifts the frequency from the double-pass AOM of the MOT stage back by 2×40 MHz. After this the beam is split into two. One entering a PM-fiber and send to the MOT cluster where it is split into two plus one beams for the spin polarization and 1D-cooling. The light for these stages is coupled via the same PM-fibers to the vacuum system. However, the beam propagating in positive y-direction needs to be orthogonally polarized to the MOT beam propagating the same direction. To get this polarization into the same PM-fiber the beam splitter before the coupler needs to be non-polarizing and thus, an auxiliary port exists in the scheme for MOT, spin polarization, and 1D cooling (this is the "plus one"). After the PM-fiber ~ 2 mW is available for imaging and about ~ 20 mW for spin polarization and 1D cooling[10]. All fiber ports on the optical table have a mechanical shutter in front of them. This way the light is switched rapidly off by means of the AOMs and safely to prevent leakage by the mechanical shutters. As doors of the optical table can be completely shut, this gives the possibility to block any unwanted resonant light from disturbing the trapped atoms.

A diode laser (Syst DL100 L, Toptica) is locked to the 2^3P_0-transition. The current of the laser can be modulated fast enough to use the lock-in scheme. However, this will be eventually substituted by a PDH-scheme employing an EOM as well to avoid the modulation on the laser itself. Most of the light is sent to two AOMs in double-pass configuration. Each shifts the beam by $\sim 2 \times 350$ MHz. Each of this highly off-resonant beams is PM-fiber coupled and amplified by a 2 W Keopsys amplifier for further use for the Raman pulses.

The third laser on the optical table is a diode laser at 778 nm which is frequency doubled in a second harmonic generation SGH all within a compact system (TA SHG 110-2V0, Toptica). The output is at 389 nm and can be locked to the 3^3P-manifold typically using polarization spectroscopy. As this wavelength can be detected bet-

---

[9]The cluster is a compact setup of PBSs and HWPs to split the beam and directly couple the resulting beams into six plus one fibers. Some light falls onto photodiodes and can be used for monitoring purposes

[10]Not all of this light is used. The fine tuning of the power is done by controlling the rf power of the AOMs

ter with CCD cameras, about $40\,\text{mW}$ of this laser are available for fluorescence measurements (e.g. for the collimation stage in chapter 2.4 and Zeeman slower in chapter 2.5), but have no specific purpose in the current system.

2.4 The collimation of the atomic beam

After producing a high flux of ^{4}He*, the atoms can be optically addressed and manipulated. This gives precise control over the atom's motion and can be used to cool and trap atoms. In order to collect a high number of atoms the first laser cooling section is installed already right after the skimmer. At this stage the atomic beam is strongly divergent and only a tiny fraction would reach a trap more than $2\,\text{m}$ downstream. An effective way to avoid loss of atoms is to collimate the beam by means of laser light. In this section a scheme is described that allows for a two-dimensional cooling of atoms moving in the third direction. In the setup the third direction corresponds to the x-axis (compare fig. 2.1).

2.4.1 The idea behind optical molasses

In section 2.2.2 it was shown that a light field impinging on atoms can exert a force. However, this is only one side of the story. As soon as the atoms are pushed in the direction of the laser the Doppler detuning changes accordingly and the atoms get out of resonance. The situation changes when a second laser impinges from the opposite side. Now, the lasers frequency can be tuned such that they are tuned to the red, i.e. $\delta < 0$, by half the linewidth of the atomic transition and the resulting net force of both lasers gives a velocity dependent force in one dimension. This effect resembles the viscous drag of molasses and gives the name "optical molasses" [87]. In fig. 2.9 it can be seen that this mechanism only works well for atoms with a Doppler shift smaller than the natural linewidth. Beyond this point the atoms experience a smaller force than what is needed to effectively eliminate the velocity component parallel (anti-parallel) to the laser light propagation. It is noteworthy, that this is not a relocating force. A particle displaced from the center of the atomic beam stays displaced, only its velocity is reduced to approximately zero (limited by the Doppler velocity of eq. (2.16)). An atomic beam entering such a molasses stage with its longitudinal velocity $\vec{v}_\perp$ perpendicular to the laser light but with some divergence in its transversal velocity component $\vec{v}_\parallel$ can in that sense be seen as getting collimated, i.e. all atoms having parallel momenta $m\vec{v}_\perp$.

The change in velocity for an atom traveling opposite to a resonant laser is limited by the Doppler shift

$$\Delta v = \frac{\Gamma}{2k_L}\sqrt{1 + I/I_s} \qquad (2.18)$$

Taking this for the transversal velocity one can define an acceptance angle of such a collimation scheme together with the longitudinal velocity as

$$\alpha_{max} = \arctan\left(\frac{\Gamma}{2k_L v_\perp}\sqrt{1 + \frac{I}{I_s}}\right) \qquad (2.19)$$
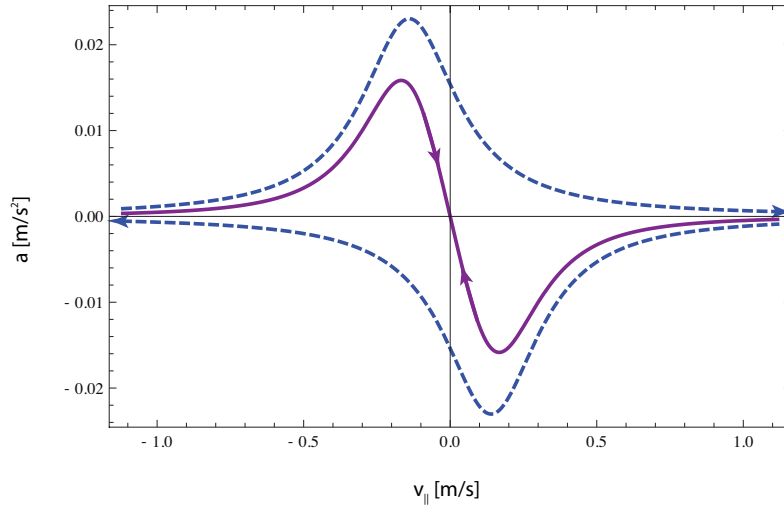
Figure 2.9: The force field of two counter-propagating laser beams (blue) is called
optical molasses. Within the linewidth the sum of both (purple) result
in a velocity dependent drag for the atom. The detuning of the lasers for
this graph is set to half the linewidth of the atom. Helium atoms with
about $0.15\,\mathrm{m/s}$ experience the strongest deceleration of $a = 15\,\mathrm{mm/s^2}$.

For an atomic beam at $v_\perp = v_x = 800\,\mathrm{m/s}$ this will mean only $1.5\,\mathrm{mrad}$. There
are schemes that employ a two-dimensional MOT to enhance the capture angle and
even focus the beam back on to its axis [88, 89]. However, this requires additional
magnetic fields and focusing the atomic beam would eventually lead to divergence
again. Thus, it would need considerable overhead around or even inside the vacuum
chamber and proper focusing such that the atoms are still bundled at the trap
position ~ 2 m behind the source.

A much simpler approach is realized in a curved wavefront scheme. The curvature
of a focused laser beam results in locally different directions for the quasi momentum
of the laser $\vec{k}_L$. This way one can make use of the angle dependence of the Doppler
shift (compare eq. (2.11)). In other words, the laser is not restricted to the one
dimension perpendicular to the main component of the velocity v_x of the atomic
beam, but can change its direction to maintain the resonance condition with the
divergent but in the process of becoming collimated atoms.

With the idea of a curved wavefront one can lift the restriction that only atoms
with a Doppler shift smaller than half the natural linewidth can be slowed. The
objective is now to maximize the capture angle β within a certain interaction length
after which the atomic beam exits the collimation section again. This is limited by
the fact that the atoms need to acquire first a certain Doppler shift, e.g. change
in velocity, before the direction of the laser should be changed. Thus, there is a
minimal radius R_{min} the atoms can be forced to move on. The minimum is given
exactly when the radiative force and the centrifugal force are of equal strength [90]

$$R_{min} = \frac{m\vec{v}^2}{\hbar k} \frac{2}{\Gamma} \frac{(1 + I/I_s)^2}{I/I_s} \tag{2.20}$$

This is the theoretical idea behind the collimation stage and in the next subsections it will be described how it is implemented in the system.

2.4.2 The implementation into the system

In the previous subsection the theoretical idea of collimating a divergent atomic beam suggested that the capability to collimate the beam can be enhanced by using a focused beam to create a curved wave front. This scheme is used in multiple experiments [90, 91]. However, from eq. (2.20) an interaction length can be deduced which is on the order of 10 cm for an enhancement of a factor of 10 in the case of 850 m/s fast helium atoms. This requires a laser with beam waist of 10 cm as well and a power to achieve a decent saturation of the transition. A different approach is to change the angle of the laser step by step. For this, two mirrors opposed to each other are tilted with a small angle ($\sim \alpha_{max}/2$) to each other [92, 93]. The laser is then injected at an angle $\beta = N_{refl} \cdot \alpha_{max}$ from being perpendicular to the x-axis. Hence, the laser resonates with atoms diverging from the x-axis with the angle β. After the beam was reflected from the mirror at opposite side and the mirror on the same side it has changed its angle by $2 \cdot \alpha_{max}/2$. The next time it impinges on the atomic beam it is thus resonant again and deflects the beam again by the amount α_{max}. This happens N_{refl} times before the laser beam becomes perpendicular to the x-axis. The same effect happens when the laser beam is on its way back from the mirror at the opposite side. However, now on atoms diverging from the atomic beam with the angle $-\beta$. The interaction length before the atoms get out of resonance is now less than 3 mm, thus a laser beam of $\sim$ 6 mm suffices to deflect the atomic beam by α_{max} (for alignment convenience the laser beam was later enlarged to 12 mm). Because the transmitted light is recycled by the mirrors much more efficient use of the light is obtained. By setting up the same mirror assembly under 90° to the first assembly a collimation in two dimensions can be achieved.

Fig. 2.10 shows a schematic of the setup. During alignment care is taken that the laser beam enters the vacuum chamber as close as possible after the skimmer of the helium source. This way it is made sure that the atoms entering the high vacuum chamber are not displaced from the atomic beam axis already before the collimation starts[11]. The relative tilt between the two opposing mirrors is then set such that the beam bounces back and forth sixteen times before they reach the end of the interaction region and are almost perpendicular to the atomic beam axis. If they were perpendicular they would be reverted and go all the way back and start heating the atomic beam transversally again. To avoid this a small angle is kept at the end of the stage, which requires the laser beam to be slightly blue detuned in order to be resonant with the atoms until they are parallel with the atomic beam axis. The common angle of the mirrors with the atomic beam axis can be used to some extent to steer the beam as this defines the final direction at which the atoms exit the stage.

To detect the atoms after collimation a light sheet with the laser at 389 nm is set up further downstream. The light sheet is tilted under 45° such that an EMCCD-camera[12] can detect the fluorescent signal from the side (for more details on the

---

[11]In chapter 2.2.2 it was shown that optical molasses is not a relocating force.

[12]For troubleshooting simple finger cameras, e.g. Sony DV1910 can be used.
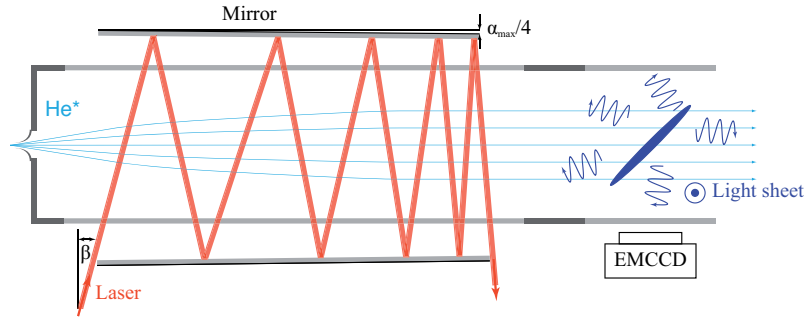
Figure 2.10: Two mirrors are set up with an angle $\alpha_{max}/2$ to each other. After deflecting the atomic beam for the first time the laser beam bounces off the mirrors twice and hence, changes its direction by α_{max}. This way the laser beam becomes resonant again with the atoms and can deflect the atomic beam again. The same happens for the laser coming back from the other mirror and another pair of mirrors is set up perpendicular to the one shown achieving a two dimensional collimation of the atomic beam. The atomic beam after the collimation stage is detected by a blue light sheet (389 nm).

EMCCD-camera see chapter 2.7) . Fig. 2.11 shows the signal without and with the collimation on. Due to the finite linewdith only atoms traveling perpendicular to the propagation direction of the light sheet, i.e. along the atomic beam axis into the Zeeman slower are scattering photons. When the collimation is off the beam diverges rapidly and only a thin line of the spread out profile is visible. The situation changes dramatically when the collimation is turned on (laser power per beam $\sim 25\,\mathrm{mW}$ corresponding to about $10\,I_s$). The atoms do not diverge anymore but are bundled in two dimensions to increase the flux by a factor of about 30.

Typically an effect of the laser beams on the atomic beam is already visible when the laser is bouncing between the mirrors like it is depicted in the inset of fig. 2.11. A fine tuning of the alignment can be done on the signal by isolating one dimension and scanning the light sheet frequency to see the whole profile. A thin line indicates proper alignment in one dimension. Switching on both dimensions achieves a signal as shown in fig. 2.11, which than can be observed with simple finger cameras (Conrad). At a later stage a Faraday-cup detector was installed behind the MOT. Monitoring the current produced at this detector is sufficient to achieve collimation, too. An additional advantage is that the direction of the atomic beam can be optimized this way since it has to go through the Zeeman slower before it enters the science chamber with the Faraday cup. A well collimated beam corresponds to about $10\,\mathrm{nA}$ on an ampere meter (6485 Picoammeter, Keithley Instruments).

After the collimation stage the atomic beam passes through a 5 mm large shutter. After loading of the MOT this is switched off to block any further flux ($\sim 10^{11}$atoms/s) of atoms into the science chamber. In an earlier stage of the project a deflection stage, working with the exact same idea as the collimation, but this time really with a focused beam, bent the atomic beam around the shutter by about 10 mrad. The idea of this is to separate the He*-atoms from any other atoms entering the system through the source. However, it turned out that the vacuum could
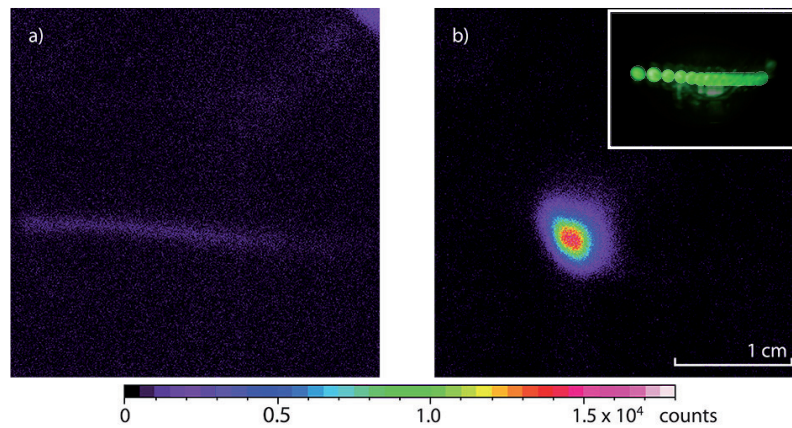
Figure 2.11: An image recorded with an EMCCD of the uncollimated atomic
beam (a) and the collimation stage switched on (b). The resonant laser
light only scatters off of atoms traveling perpendicular to it. Hence,
in the uncollimated beam only a thin stripe of the divergent beam is
visible. However, when the collimation is switched on the atoms are
collimated on the x-axis and resonate with the light sheet. With the
collimation stage on an increase by a factor of 30 is achieved. The inset
shows an infrared light intensified image of the reflections of the laser
beam on the surface of one of the mirrors.

be improved by introducing a complete valve (DN40 Slide Valve with Million Cycle
Option, VAT) in front of the Zeeman slower that shuts any time the magnetic trap
is loaded. Thus, the deflection stage was redundant and is not used anymore in order
to simplify the system.

2.5 The Zeeman-tuned slowing of neutral atoms

The most frequently used species for ultra cold experiments Rb is usually prepared
by heating a dispenser. The evaporated Rb has a low energetic tail with enough
atoms to be collected by a MOT. Thus, without any further effort the MOT can be
loaded just from the background pressure in the chamber. In the case of helium an
atomic beam enters the ultra high vacuum chamber. After the collimation stage a
high flux of atoms is achieved. The atoms produced in the dc discharge are in the
metastable state and the two dimensional transversal cooling made sure they are
only minimally divergent. However, they travel at the speed of about 800 m/s. This
is far too high to be captured by a magnetic trap and even a MOT with a capture
range of about 100 m/s operates at lower velocities. In this section it is described
how the atoms can be slowed sufficiently in longitudinal direction to be captured in
a MOT.

2.5.1 The theory behind Zeeman-tuned slowing

A resonant laser counter-propagating to the atomic beam can slow the atoms according to eq. (2.18) by less than $1\,\text{m/s}$; by far too little to bridge the gap between atomic beam velocity and capture velocity of the MOT. In the early beginnings of laser cooling of atoms there were schemes, where the laser frequency was chirped to stay on resonance with the slowed atoms [94]. Yet, besides technical challenges for the chirp this produces a pulsed train of atoms. A more frequently applied method nowadays is to make use of the Zeeman shifts occurring in magnetically degenerated energy levels [95, 96]. According to eq. (2.14) a magnetic field can compensate for a Doppler shift and the laser stays on resonance with the atom even if the laser frequency is unchanged and the atom slows down. By lifting the degeneracy though, the closed-cycle transition in general is open to loss to other magnetic sublevels. This loss is avoided by driving a transition whose only decay channel is back to the magnetic sublevel the electron came from. The only points in a magnetic sublevel splitting to achieve a closed cycle transition are at the very end of a transition (see fig. 2.5). However, the maximally stretched state does not suffice to maintain a closed cycle. To make the process efficient it is additionally necessary, to have an excited state with one quanta of total angular momentum more than the ground state, supporting one more magnetic sublevel. Hence, driving a σ-transition with a circularly polarized laser is possible and the cycle remains closed even under varying magnetic fields. This is the reason for locking the cooling laser to the 2^3P_2-transition[13].

Since the objective is to slow the atoms exiting the collimation stage from an initial velocity to a final velocity within a fixed distance x_0, the atoms will have a position dependent velocity within the Zeeman slower. Equivalently, the Doppler detuning will be position dependent and thus, the magnetic field will have to vary depending on the position of the atoms and fortunately not in time. Assuming a constant force, i.e. deceleration, the velocity drops quadratically with distance traveled. Thus, an appropriate magnetic field to maintain the resonance condition follows [97]

$$B(x) = B_0 - B_{x_0}\sqrt{1 + x/x_0} \tag{2.21}$$

As there are two maximally stretched states the Zeeman slower can in principle operate at either of the two σ-transitions, depending on the definition of the quantization axis. It is intuitive to use the initial magnetic field direction to define this axis. The most simple type of Zeeman slower starts at zero magnetic field which then gradually increases until it reaches its maximum magnitude at the end of the slower. This way the Zeeman-tuned slowing works on the closed cycle transition of σ^+. A Zeeman slower employing the σ^--transition on the other hand, starts at a high magnetic field and then monotonically decreases. However, latter design allows for some freedom in choosing the final magnetic field. By giving the counter-propagating laser light a red detuning from the atomic resonance the magnetic field can cross zero magnitude, change its direction and increase again. This change typically is slow enough, such that the atoms can follow the change in magnetic field and do not undergo Majorana-flips (see chapter 2.8). There are two main considerations why this advantage is important for the implementation. Firstly, for helium there exists a

---

[13]The same reasoning applies to the situation in the MOT

level crossing between the used transition 2^3P_2 and the 2^3P_1-transition at $563\,G$ [98], a magnetic field magnitude close to what would be required by a σ^+-Zeeman slower for atoms in this experiment. The other consideration is related to the section that follows the Zeeman slower. Obviously, a large field at the end of the Zeeman slower takes longer to decay and thus, would penetrate deeper into the MOT where the experiments later will take place. Nevertheless, the laser beam for Zeeman slowing shines through the MOT. Hence, some magnetic field at the end of the Zeeman slower bears the additional advantage that the laser needs to be detuned and by proper design can be far off-resonant for atoms in the MOT.

In chapter 2.2.2 it was argued that the spontaneous emission is isotropic in all directions and thus the net force is zero. However, in the process of scattering individual photons the atoms undergo a random walk and thus the beam spreads transversely [99, 100]. This heating becomes more pronounced the longer the slower is and towards the end of the Zeeman slower and has a severe effect on the divergence of the atomic beam exiting the slower. Thus, a short slower is desirable and the exit of the slower should not give much space for the atoms to diverge before they are captured by the MOT.

2.5.2 The implementation of the Zeeman slower into the system

With the Biot-Savart law it is straight forward to calculate a magnetic field for a given geometry of currents. The reversed process, i.e. calculating the required geometry of currents for a desired magnetic field can be challenging. However, with nowadays computer power an algorithm can be run to optimize the distribution of current loops such, that the shape of the magnetic field on the axis of the solenoid has the desired profile. The final code for such an optimization using Mathematica can be found in Florian Leupold's master thesis [101]. The result is shown in fig. 2.12. The theoretical curve is given by the amount of deceleration required and the length of the vacuum tube.

Here, it becomes obvious why the closed cryostat at the source to pre-cool the atoms and thus, achieve a smaller initial velocity makes the whole system smaller and simpler. The atoms only need to be slowed by about $800\,\mathrm{m/s}$, which corresponds to about $530\,G$ and is theoretically possible on a distance of roughly $80\,\mathrm{cm}$. In the case of a Zeeman slower with a zero crossing the magnetic field B_0 can be distributed roughly even between the two sections on the left and right of the zero crossing. This is advantageous as the required electrical power to run the solenoid is mostly determined by the maximal magnetic field. Additionally, not only more power is consumed for high fields, but the dissipation of electrical power into heat makes active water cooling a requirement at a certain level. For this reason the first generation Zeeman slower consisted of double-wall vacuum tube to carry cooling water along the inner side of the solenoid. However, the current needed and the heat dissipation were small enough to discontinue the water cooling precautions in the second generation slower.

The algorithm to compute the necessary current distribution arranges small coils in an optimal way to reproduce the desired field. This is exactly what happened in reality when a wire was wound around the vacuum tube. Fig. 2.13 shows the
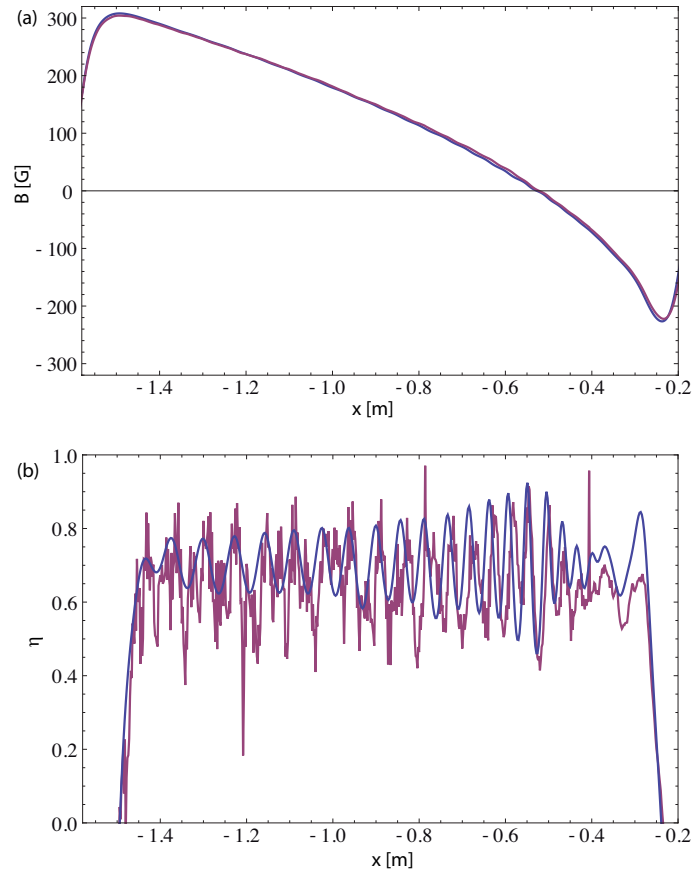
Figure 2.12: The magnetic field in the vacuum tube for the Zeeman slower follows eq. (2.21). The real field (purple) and the simulated (blue) correspond almost perfectly (a). However, at the steps of the layer a step in the field occurs, too. This is more obvious when the local efficiency $\eta(x)$ is plotted (b).

partially finished Zeeman slower on a lathe-like arrangement to wind the solenoid. The solenoid is wound in such a way that a first layer of coils is wound until the desired amount of coils is reached. Then the wire is lifted into the next half-layer and wound back. Repeating this for all layers, care was taken that the wires stay where they are supposed to be by fixing them with Kapton tape at the steps of one layer to the next. A plastic ring holds the wire in place at the start of all layers. An important point for the construction is that wire with a circular cross-section does not tightly drop into the grooves of the preceding layer, making the layers irregular very fast. For this reason rectangular wire is used with dimensions of the enameled wire of $2.5 \times 1.1\,\mathrm{mm}^2$ plus $0.05\,\mathrm{mm}$ isolation on each side.

The solenoid has two geometrical constraints in terms of its diameter. The outer diameter was given by the design of the science chamber and the effort to be as close as possible with the exit of the Zeeman slower to the MOT position. The inner diameter is given by the diameter of the vacuum tube. On one hand, this should be as small as possible to improve the ultra high vacuum in the science chamber by differential pumping. On the other hand the atomic beam needs to get through it

Figure 2.13: For building of the Zeeman slower the vacuum tube was mounted with ball bearings such that it can be rotated. A rectangular wire was carefully wound around the tube forming a tapered solenoid to create the required magnetic field to slow atoms inside the tube.

and be decelerated. Not only a hard task to align, given the length of the Zeeman slower (1.36 m), but the smaller the inner diameter of the solenoid the less uniform is the field inside the tube. Thus, the atomic beam needs to be more precisely on the axis of the slower. For this the outer tube diameter (wall thickness 2 mm) was chosen to be 34 mm. Fig. 2.14 shows that the current design is tolerant to atoms being more than 10 mm off axis. The magnetic field calculations for this where done using the Radia[14] package for Mathematica with which the three dimensional magnetic field of known geometries can be calculated easily.

While the ideal Zeeman slower has a smooth variation along the axis, the real solenoid is made out of individual coils with steps at each layer (compare fig. 2.12). At these steps the magnetic field changes faster than what would be required for a constant deceleration. To take this into account a position dependent efficiency $\eta(x)$ of the Zeeman slowing can be calculated [97]

$$\eta(x) = \frac{2m\mu_{eff}}{\hbar^2 k_L^3 \Gamma} \frac{dB(x)}{dx} \left(\frac{\mu_{eff}B(x)}{\hbar} - \delta_0 \right) \tag{2.22}$$

where δ_0 is really just the detuning of the laser from the atomic resonance without taking the Doppler or Zeeman shift into account. As can be seen in fig. 2.12 the efficiency of the slower needs to go up everywhere a layer of coils ends. If there is enough time between steps where the required efficiency is low enough for the atoms to catch up again, the slower works even with short stages where the efficiency goes above unity. However, once the resonance condition is lost, the atoms will never get

---

[14]Radia is a Mathematica package developed by the European Synchrotron Radiation Facility (ESRF) and can be used in different branches of physics, where efficient solutions of 3D boundary problems of Magnetostatics are needed
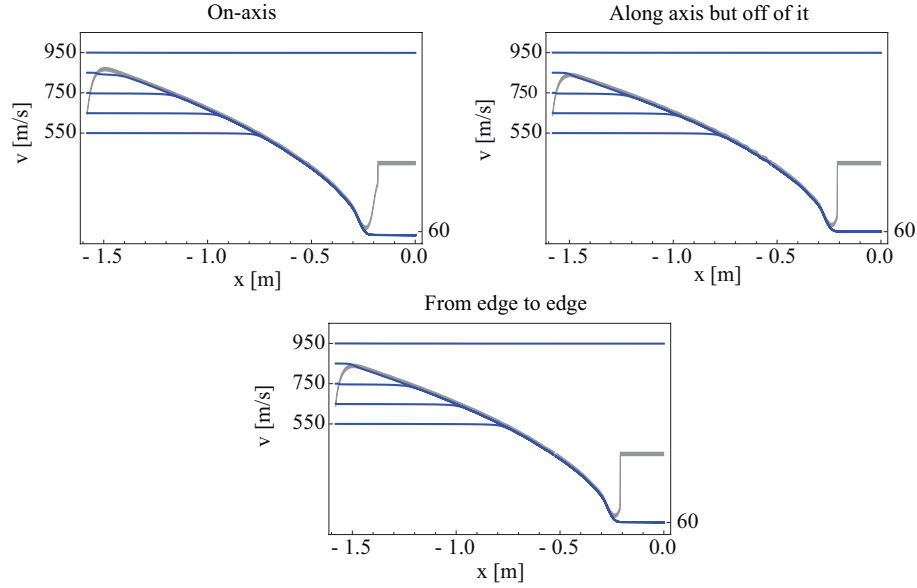
Figure 2.14: Calculating the equation of motion of the atoms along different direc-
tions in the vacuum tube reveals the tolerance of the Zeeman slower
to misalignment. All atoms entering the Zeeman slower with velocities
smaller than 850 m/s are collected and slowed to less than 60 m/s. Even
if the atomic beam is completely off axis or misaligned with the Zeeman
slower axis, the atoms are slowed.

back into resonance. Thus, it is meaningful to make the slower a little longer than
what is necessary. A length of the solenoid of 1.36 m gives an overall efficiency of
about 0.7.

The power for the solenoid (2.2 A for the first section and 1.9 A for the second)
is delivered by a standard laboratory power supply (PL330QMD, Thurlby Thandar
Instruments). The current stability only marginally changes the acceptable veloc-
ity (first section) and final velocity (second section) of atoms that can be slowed.
So no active stabilization of the currents is required. However, as the MOT is al-
ready 20.5 cm downstream of the Zeeman slower exit, no compensation coil for the
magnetic field was installed, which would require even more space. Therefore, the
magnetic field of the second section can penetrate into the MOT region (1 G in z-
direction at the center of the MOT). There was no effect observed on the MOT when
the Zeeman slower was left on. However, in full operation of the system the second
section is switched of by a voltage at a linearly regulated insulated-gate bipolar
transistor (IGBT) to avoid effects in the magnetic trap and imaging. The IGBT ad-
ditionally stabilizes the current through the section by comparing the voltage across
a shunt resistor.

The laser beam to perform the deceleration is expanded by a fiber coupler (60FC-
Q1083-4-M150-37, Schäfter und Kirchhoff). The coupler holds a $\lambda/4$-waveplate to
make the laser circularly polarized. To reduce the effect of the random walk heating
in the slower the laser is focused onto the source, i.e. the initial 36 mm beam waist
reduces to below 1 mm at the skimmer. This creates a curved wave front just as in
the collimation section. The photons off-axis have some component pointing towards

the axis and can thus imprint a small momentum kick back to the axis. When the Zeeman slower was first set up a laser power of about $90\,\text{mW}$ was used. However, a laser power of $10\,\text{mW}$ suffices as well, corresponding to the saturation intensity. The detuning of the laser is $\delta_0 = -370\,\text{MHz}$.

The atomic beam entering the Zeeman slower consists of an unpolarized sample of atoms. Atoms in the wrong magnetic sublevel would not be slowed in the Zeeman slower as their energy shifts would be in the wrong direction. However, the field first rises at the entrance of the Zeeman slower before actual slowing begins at the maximum field. Within this slope the transition m_{-1}[15] to m_0 becomes resonant first and the m_{-1}-state becomes depopulated. A little bit later the transition m_0 to m_1 becomes resonant with the laser light and hence, the atoms become spin polarized as they enter the Zeeman slower.

In order to achieve ultra high vacuum in the science chamber the source side has to be blocked as well as possible. The first measure is to reduce the opening of the Zeeman slower. For this purpose a differential pumping tube with an outer diameter matching the inner diameter of the vacuum tube of the Zeeman slower is inserted. The differential pumping tube has a bore of $3.5\,\text{mm}$, just big enough to let the atomic beam enter, and has a length of $150\,\text{mm}$. In the second generation of the Zeeman slower a six-way-cross was placed at the zero crossing of the magnetic field, i.e. where no solenoid is needed. This gave optical access, but more importantly gave space for a turbo pump (HiPace300, Pfeiffer Vacuum) that pumps out already most of the residual gas coming from the source.

2.5.3 The performance of the Zeeman slower

To confirm that the actual magnetic field reproduces the simulated one, a Hall-probe was guided through the tube. A sledge carrying the probe was moved in $2\,\text{mm}$ steps by means of a $M6$-threaded rod. Fig.2.12 shows how well the field matches the theoretical needed one.

For troubleshooting the experiment the velocity of atoms coming out of the source for He* has to be measured, as too fast atoms cannot be slowed by the Zeeman slower (see fig. 2.15). For diagnosis purposes the initial velocity of the atomic beam it can be "chopped" by switching of and on the collimation section. The arrival of atoms at the Faraday cup $2.1\,\text{m}$ behind the source is indicated by a rise of the flux, i.e. increase in current. From this time of flight measurement a velocity can be deduced. To characterize the functionality of the Zeeman slower no faraday cup can be placed further downstream as the laser light would be blocked. An alternative, is to probe the atomic beam behind the Zeeman slower from the side with the laser at $389\,\text{nm}$. The scattered photons from this laser are then collected by an EMCCD. The laser is not at perfectly $90°$ to the atoms, but deviates from this by an angle β. This gives the laser a small but sufficient sensitivity to the longitudinal velocity of the atoms by means of the Doppler shift $\delta_D = -k_L v_x \cos\beta$. This doppler shift needs to be compensated by the laser frequency to maintain a high fluorescence signal. Two AOMs are arranged such that the angle of the beam is unchanged when scanning δ_0 from $0 - 60\,\text{MHz}$ (see fig. 2.8).

---

[15]For the remainder of this dissertation the state $m_J = -1$ is abbreviated as m_{-1} and all other magnetic substates correspondingly as no confusion with different J can arise.
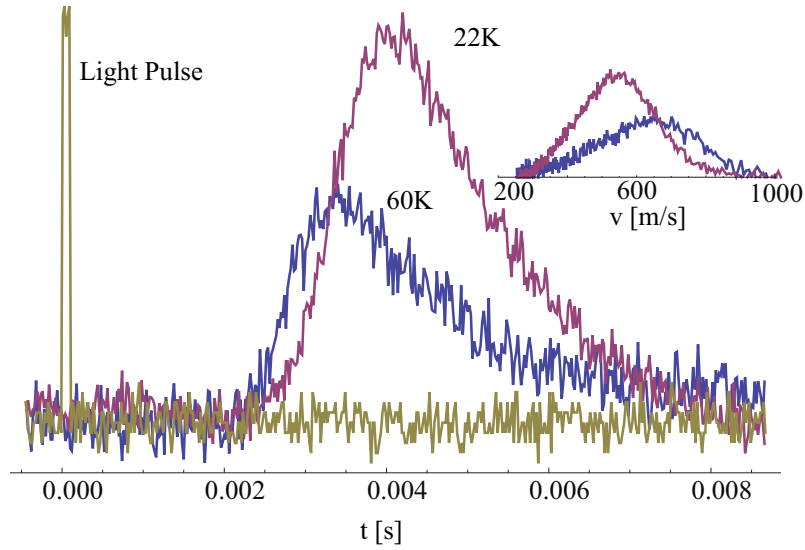
Figure 2.15: The atomic beam can be "chopped" by turning on and off the col-
limation stage. The increase in flux is detected with a Faraday cup
2.1 m behind the collimation section. The light pulse is recorded as well
and serves as reference (brown) to calculate the time of flight of the
atoms. The purple trace corresponds to a source running at 60 K and
the blue to 22 K. The velocity increases when the source is warmer.
The inset shows the corresponding velocities. This can be used for di-
agnostic purposes of the source however, is not available to measure
the velocities after the Zeeman slower. The velocities shown here are
significantly smaller than what was measured when the source and the
Zeeman slower were initially characterized. The data here is from a
more recent troubleshooting and hence suggests that the source has
improved during operation in that characteristic.

From the signal strength the resonant atoms can be counted and via the condition
$\delta_D = \delta_0$ related to a velocity. Fig. 2.16 shows the result of such a measurement for
a non-slowed beam, the first Zeeman section turned on, and for the second section
turned on at about 1 A. The initial atomic beam has a velocity peaking at almost
900 m/s. The first section than reduces the velocity to about half its magnitude,
while the second brings them down to about 150 m/s.

The overall intensity of the slowed atoms seems to decrease, the slower the atoms
get. However, this is due to the random walk heating that causes the atoms to spread.
The absence of any atoms at the initial velocity rather indicates a high degree of
efficiency of the slowing process. The reduced signal strength at lower velocities is
also the reason for the low current in the second section. Higher currents in the
second section would further reduce the speed. However, they were not detectable
anymore with the described method. As a matter of fact this is the signature of a
working Zeeman slower in the usually used troubleshooting scheme: a resonant laser
sheet of the 389 nm laser shines through a viewport of the MOT and its fluorescence
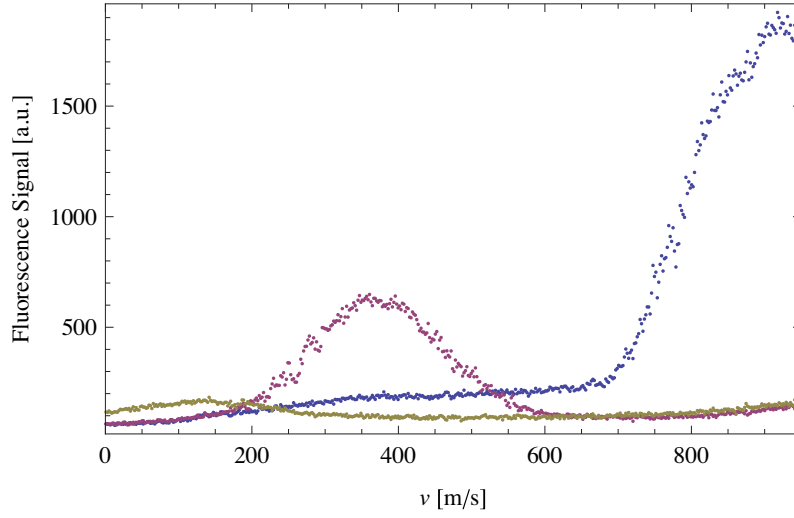is viewed by the EMMCD. The atoms can be seen when the slower is off. When

Figure 2.16: The velocity of the atomic beam after the Zeeman slower is measured with an off-resonant laser beam under an angle to be sensitive to the velocity component along the x-axis. Scanning the laser frequency reveals the operation of the Zeeman slower. Without the Zeeman slower the atoms have a velocity of about 900 m/s (blue). The first Zeeman slower section slows the atoms to less than 400 m/s (purple) and the second section brings the velocity down to capturable values (brown). The decrease in signal is caused by the spread of the atomic beam due to transversal heating within the Zeeman slower.

the first section is switched on the signal spreads and with the second section active almost no atoms are visible.

2.6 The magneto-optical trap

The source supplies the experiment with He*, the collimation stage increases the flux, and the Zeeman slower decelerates the atoms tunably below 100 m/s. The next step is to spatialy trap the atoms. For this purpose, all ultra cold atom experiments use the celebrated magneto-optical trap (MOT) [102–107]. The MOT combines a magnetic field with the radiative force of light to create a position dependent force field. In this section the principle idea behind a MOT is presented for completeness, but is not focus of this dissertation.

The MOT consists of three pairs of lasers and two coils for the magnetic field. The coils are positioned at $y = \pm 60$ mm on the y-axis which is horizontal and perpendicular to the atomic beam propagation direction (x-axis). They are part of the magnetic trap[16] as well, but are used in this situation with 75 A in an anti-Helmholtz configuration. An observer at the center of the trap looking in positive y-direction would see the current at $y = +60$ mm rotate clockwise. This creates a quadrupole field ($\frac{dB}{dy} \sim 7\,G/m$) with the magnetic field pointing away from the

---

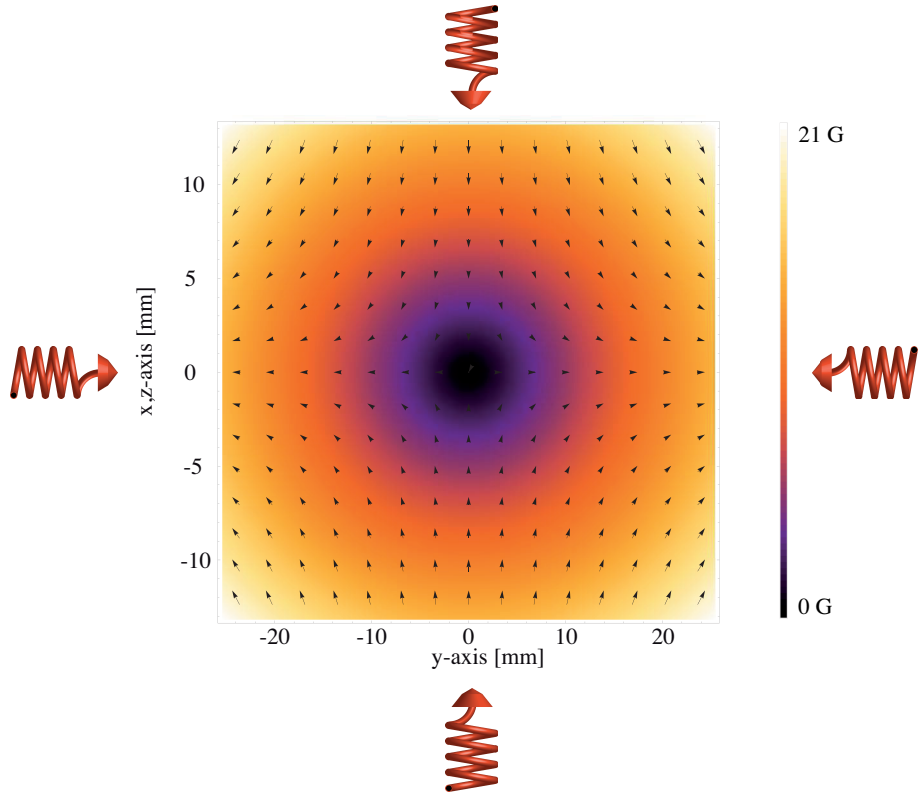[16]Chapter 2.8.2 will describe how they are produced

Figure 2.17: A two dimensional schematic of the MOT principle. Due to the symmetry of the coils, the field is rotationally symmetric around the y-axis as well. The field lines are pointing away from the origin at the y-axis and to the origin in xz-plane. This way a local quantization can be defined that allows for σ^+-transitions, with the laser counter-propagating the atoms. Due to the Zeeman shift the atoms stay on resonance with the laser beam they are propagating towards even when they are slowed.

origin on the y-axis and to the origin in the xz-plane (see fig. 2.17). The laser pairs are then on the y-axis and in the xz-plane. In order to not interfere with the Zeeman slower the pairs in the xz-plane are under $45°$ and $-45°$ to the x-axis, respectively. The lasers are detuned $-40\,\mathrm{MHz}$ from the atomic resonance and are all circularly polarized.

While the lasers on the y-axis are right handed [17], the four lasers in the xz-plane are all left handed. This way they are all driving a σ^+-transition on their side of the trap. As the lasers are red detuned they are in resonance with atoms in the center that move rapidly towards them. Due to the magnetic field they are also resonant with slow atoms on there respective side of the trap and not resonant with atoms, slow or fast, at the other side of the trap. Simplified, this means each side of each direction forms a Zeeman slower, which eventually pushes the atoms back into the trap. The mechanism of a MOT is analyzed e.g. in ref. [104]

---

[17]Throughout this dissertation the convention for left and right handed is to define it with respect to the photon, i.e. an observer travelling with the photon would see the electric field rotate clockwise for right handed light

To generate the six beams the laser with shifted frequency is split into six plus one[18] equally power balanced components by the fiber cluster. They are then guided by fibers directly to collimators that are attached to the viewports and have only the tip/tilt degrees of freedom. The collimators have a $\lambda/4$-waveplate incorporated to produce the correct polarization after the PM-fiber. The beam waist after the collimators is 55 mm corresponding to about twice the saturation intensity.

The MOT is able to capture atoms as fast as $80\,\mathrm{m/s}$ (this is equivalent to a few K) and cool them down to typically $\sim 1.5\,\mathrm{mK}$. This is a reduction of three orders of magnitude in temperature from the velocity after the Zeeman slower[19]. In principle one could think that an infinite amount of atoms can be trapped with a MOT as long as atoms are supplied by the slowed atomic beam. However, collisions with the hot background gas and inelastic intraspecies collisions (e.g. three body collisions that lead to the formation of molecules) lead to a loss of atoms from the trap. Especially for metastable helium the rate at which inelastic collisions occur increases as the density of the cold cloud increases with higher atom numbers. For He* detrimental inelastic collisions can happen already between two helium atoms. The high internal energy of He* is not only released upon collision with the walls of a MCP, but also when the atom collides with another He* or a background gas atom. In this process the He* atom returns to the real ground state and its energy ionizes the collision partner. Thus, all participants of the collision are lost from the trapping scheme due to the so called Penning ionization.

The Penning ionization is the reason for the large detuning of the MOT lasers[20] to minimize the loss rate due to high densities but still achieve large atom numbers [105, 106, 108]. However, at some point loss rates become as large as the loading rate with the slowed atomic beam and a steady state is reached. In this system the steady state is reached when about 10^9 atoms are compressed to a sphere with radius $\sim 1.2\,\mathrm{mm}$ (Fig 2.18 shows a time series of a cloud after being released from the MOT). This is an increase of phase space density by four orders of magnitude from the start at the source and serves itself as a starting point for ultra-cold atom experiments.

2.7 The absorption imaging of atomic clouds

The shadow image of atoms in fig. 2.18 was taken by shining a weak laser beam on the cold atoms. The laser is resonant with the atoms and some photons get scattered out of the beam. An EMCCD behind the cloud collects the unscattered photons and by that images the shadow of the atoms. This absorptive measurement heats up the cloud and the atoms are eventually lost. There are schemes that can monitor cold atoms non-destructively by using off-resonant lasers which only experience a dispersion due to the presence of the dense cloud of atoms [109]. However, absorption imaging is the simplest scheme to implement and is well understood to determine atom numbers and cloud profiles. This section describes how the images are taken and analyzed to gain the information about the cloud.

---

[18]the seventh component is only used for monitoring. This occurs because the lasers for spin polarization (see chapter 2.8.4) are prepared with the same cluster.

[19]Actually, the temperature of the atoms after the Zeeman slower with respect to their velocity distribution in a co-moving frame is almost the same as in the MOT

[20]Typical alkali experiments work with a detuning on the order of the linewidth
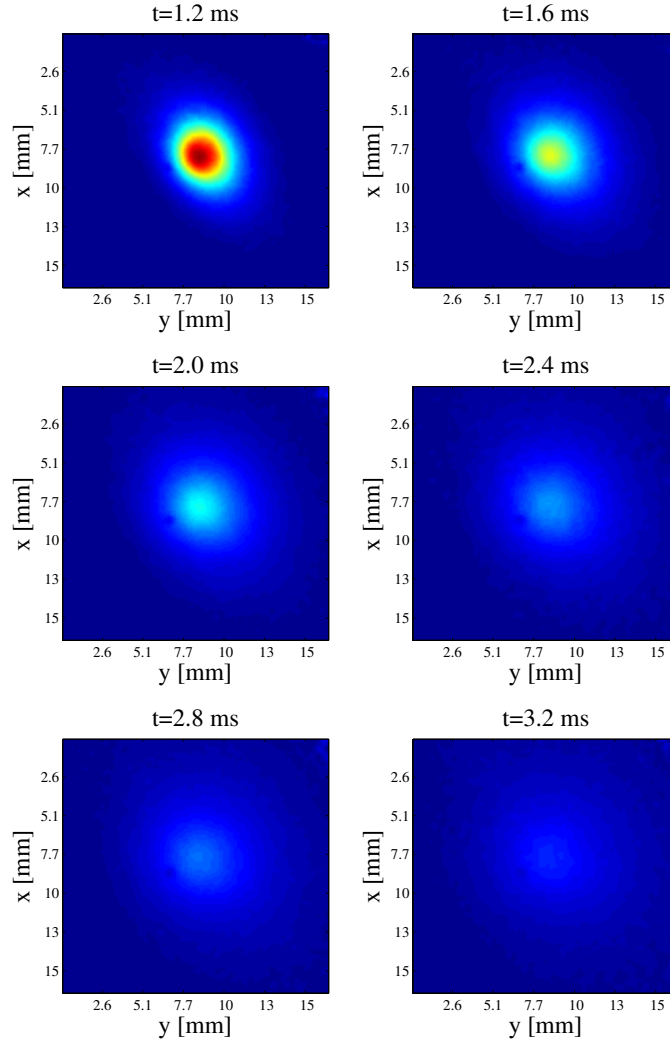
Figure 2.18: The atomic cloud expanding after being released from the MOT is imaged with absorption imaging (see next section 2.7). The temperature of the cloud can be extracted from the isotropic expansion.

For imaging an EMCCD-camera (iXon885-VP, Andor) is used. The chip is optimized to extend into the near UV spectrum and has ultra fast readout electronics (35 MHz, vertical clock speed $< 1\,\mu$s). However, due to the electronmultiplier gain it is able to detect low intensity levels of light with 1083 nm wavelength as well. Hence, the 1 Megapixel large chip with $8 \times 8\,\mu$m^2 pixel size can be used for absorption imaging with intensities below the saturation intensity. Emerging cameras using an InGaAs chip, which has its maximal sensitive further in the near IR, are available. However, in practice no superior images could be obtained and more post- or pre-processing of the read out signal is required.

The simple scheme of absorption imaging is depicted in fig. 2.19. The laser is scattered from the cloud and loses intensity depending on the profile of the atomic cloud. This is an application of the Lambert-Beer law (eq. (2.9)). However, in this case not the total intensity is recorded. A lens images the plane of the cloud on to

Figure 2.19: A laser beam falls onto the atomic cloud and is partially absorbed. Two lenses can be placed in between the atomic cloud and the EMCCD camera to select between different magnifications ($f = 125\,\mathrm{mm}$ for 4:1 and $f = 150\,\mathrm{mm}$ for 1:1). The offset coils can be used to define a quantization axis parallel to the laser beam.
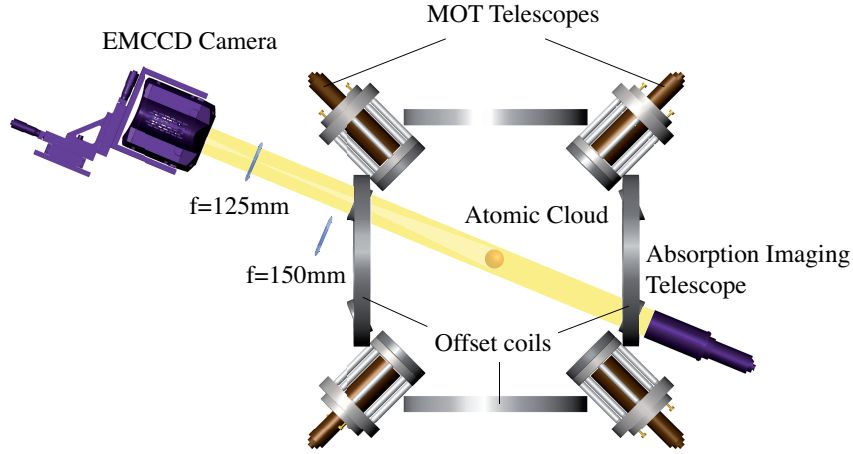
the chip of the EMCCD camera and the two dimensional profile of a low intensity laser beam coming from $-\infty$ is gained[21]

$$I(x,y,z) = I(-\infty,y,z)\exp\left(-\frac{\Gamma}{2}\frac{\hbar\omega_L}{I_s(1+4(\delta/\Gamma)^2)}\int_{-\infty}^{x}n(x,y,z)dx\right) \qquad (2.23)$$

where the resulting intensity profile is an integration over the density $n(x,y,z)$ of the cloud along its propagation direction. In this low intensity approximation it is also assumed that the laser linewidth is negligible compared to the linewidth of the transition. An imaging sequence consists of an image of the shadow of the cloud $I_c(y,z)$, a subsequent image of the laser without cloud as reference $I_r(y,z)$, and finally an image without the laser to subtract the background $I_b(y,z)$. As the absorption is logarithmic the final picture is calculated as well by taking the logarithm to obtain optical density(compare eq (2.9))

$$OD(y,z) = \ln\left(\frac{I_c(y,z)-I_b(y,z)}{I_r(y,z)-I_b(y,z)}\right) \qquad (2.24)$$

From the original Lambert-Beer idea one can assume each pixel of the EMCCD to be a bucket detector and just sum up the intensity on each pixel to get the number of atoms N [110]

$$N = -\frac{2\pi A_{pixel}}{3\lambda^3}\frac{I_s'(T)}{I_s}\sum_{pixel}OD(y,z) \qquad (2.25)$$

---

[21]Here the coordinate system is rotated by $\pi/8$ around the y-axis with respect to the original coordinate system. This makes the analysis for absorption imaging much easier as the new x-axis falls together with the k-vector of the light.

Here A_{pixel} is the effective area of the pixel taking magnification by the optical system into account. Additionally, a parameter $I'_s(T)$ is introduced. This takes care of effects of polarization and temperatures for the saturation intensity and will be discussed a little later. A more complete information about the atomic cloud can be gained from fitting the resulting image. Not only are statistical fluctuations on different pixels averaged out this way, but also the radii of the cloud can be extracted. A thermal cloud's density is governed by the Boltzmann statistics and results in a Gaussian distribution. However, the BEC is described by an inverted parabola (compare section 2.9). So the fit needs to include two functions when approaching the transition to the BEC:

$$OD(y,z) = -\frac{\hbar\,\omega_L}{I'_s(T)}\frac{\Gamma}{2}\left(\frac{N_{therm}}{2\pi\sigma_y\sigma_z}\exp\left(-\frac{y^2}{2\sigma_y^2}-\frac{z^2}{2\sigma_z^2}\right)\right.$$

$$\left.+\frac{9}{16}\frac{N_{BEC}}{R_{TFy}R_{TFz}}\left(1-\frac{y^2}{R_{TFy}^2}\right)\left(1-\frac{z^2}{R_{TFz}^2}\right)\right) \tag{2.26}$$

This is the general fitting function including a BEC with its Thomas-Fermi radii $R_{TF\,y,z}$. However, in most situations only one of the distributions is imaged and the respective term can be dropped. Additionally, to the number of atoms the fit procedure also holds the radii of the cloud. Taking a time series of the cloud expanding, i.e. measuring the time of flight, one can deduce the temperature of the cloud as well as

$$\sigma_i^2(t) = \sigma_i^2(0) + \frac{k_B T}{m}t^2 \tag{2.27}$$

This is how the most important data is extracted from the images, though in the equations a modified saturation intensity is used. There are two factors modifying the lineshape of the atoms. Depending on the orientation of the atoms with respect to the laser beam propagation, i.e. the polarization of the atoms, and the laser polarization, the laser is absorbed with different strength. In different situations different factors have to be used and a detailed analysis can be found in ref. [111]. For linear light and unpolarized atoms the f-factor is initially 18/10 and becomes 17/10 in the steady state. A circularly polarized beam pumping the atoms to the m_{+1}-state changes more drastically the f-factor to ideally up to 3. However, comparison of the two polarizations did not show a statistical significant difference in the MOT and magnetic trap. This is likely to be due to the propagation direction of the laser perpendicular to the quantization axis of the magnetic trap. This way the atomic cloud appears unpolarized to the laser beam and the optical pumping is insufficient to reach a steady state with $f = 3$. To be less susceptible to magnetic field fluctuations after the switch off of the magnetic trap, typically a field of $2\,G$ is applied pointing in the propagation direction of the laser.

A second factor $\chi(T)$ is required owed to the thermal distribution of the atoms. Not all atoms are on resonance with the laser. Integration over the Boltzmann

distribution for thermal atomic clouds then gives

$$\chi(T) = \sqrt{\pi} u(T) \exp\left(u^2(t)\right) \operatorname{erfc}\left(u(T)\right) \tag{2.28}$$

$$u(T) = \frac{\lambda \Gamma}{4\pi} \sqrt{\frac{m}{2k_B T}}$$

This is a marginal correction for the heavy alkali. In helium however, a temperature of $50\,\mu K$ results in 10% less absorption by the atoms and a cloud with a temperature of $1\,\text{mK}$ already absorbs 70% less light. With these two corrections the saturation intensity is given by

$$I_s'(T) = \frac{f}{\chi(T)} I_s \tag{2.29}$$

Typical CCD cameras are made for visible light. The two transitions of He* lie at the edge of this spectrum. However, most cameras have a prolonged quantum efficiency (QE) into the ultra violet, while the infrared is significantly reduced. The EMCCD used in this experiment has a QE of $\sim 30\%$ at 389 nm and 0.1% at 1083 nm. This makes the blue laser a convenient tool when monitoring the fluorescence of the atomic beam in the sections 2.4 and 2.5. Yet, the atoms exposed to the laser beam are pushed in the direction of the beam and heated radially leading to a weaker signal as the light impinges on them. The more photons the atoms absorb the more they get out of resonance and scatter less photons. For fluorescent imaging of an atomic beam this degradation does not play a role as new atoms are continuously provided. However for imaging of cold samples of atomic clouds it becomes important. Fig. 2.20 shows the scattering rate per atom over time for the two transitions.

It is clear from these considerations that the blue laser is not useful to obtain a good signal in absorption imaging. The atoms do not even scatter two photons before they get out of resonance, due to the high recoil velocity of 256.5 mm/s. On the other hand, the atoms can scatter about 15 photons within $60\mu s$ when exposed to $0.1\,I_s$ of the light driving the 2^3P_2 transition. Thus, the higher scattering outweighs the technological advantage of laser with a wavelength of 389 nm. A possible solution to overcome the radiative force in imaging of one beam is to set up an optical scheme where second beam from the opposite side balances the force on the atoms [70, 112]. However, metastable helium does not rely on such sophisticated optics as detection of helium can outstandingly be achieved with the DLD detector.

2.8 The magnetic trapping of metastbale helium

The MOT is able to capture atoms with velocities up to $80\,\text{m/s}$ and cool them to a few mK. Bose-Einstein condensation typically occurs around $1\,\mu K$. This is even below the Doppler temperature. When the first BEC was produced in 1995 the breakthrough came with the implementation of evaporative cooling for atomic gases [113, 114]. Evaporative cooling will be described in more detail in chapter 2.9, but the idea is similar to cooling a cup of coffee. The hottest atoms evaporate from the liquid and the remaining atoms cool down. To enhance the effect one can blow the vapor away and force the evaporated atoms away to leave, thus more
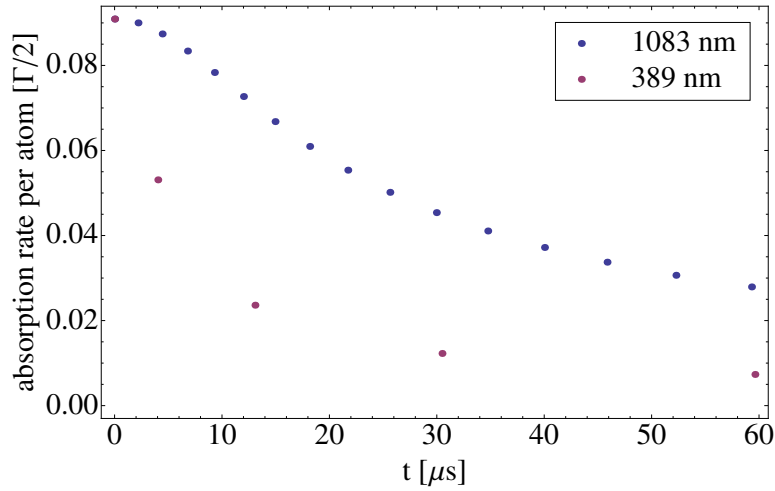
Figure 2.20: The scattering rate per atom is displayed over time in units of the maximal possible scattering rate. Each dot indicates a scattered photon after an average time. Because of the large momentum transfer the scattering rate per atom drops significantly before a second photon can be scattered in the case of 389 nm laser light. The exposure time in the case of laser light with wavelength 1083 nm is chosen such that about 15 photons are scattered at $0.1\,I_s$.

atoms can evaporate. In principle this can be achieved in an optical dipole trap. Optical dipole traps are not based on radiative force which limit the temperature, but are conservative forces far off resonance to avoid absorption of photons, i.e. momentum transfer. Nevertheless, "blowing" the hottest atoms away is hard in this scheme. There are schemes of crossed dipole traps that achieve all optical runaway cooling [80, 115, 116], however magnetic traps offer an easier handle to do the forced evaporative cooling.

In section 2.6 it was argued that Penning ionization limits the density achievable with metastable atoms. However, it was experimentally shown that Penning ionization is significantly suppressed for a spin polarized cloud [72]. During Penning ionization of a triplet state atom the electron needs to flip its spin in order to relax to its ground state. However, in a spin polarized cloud a two atom system is in its maximally stretched state and the collision partner cannot take up the spin of the relaxed electron. Thus, spin conservation avoids Penning ionization. This is especially pronounced in the case of ^{4}He, where no nuclear spin exists which could take up the spin. Because all other noble gases have a nuclear spin, this actually is the dominant effect that so far has obstructed condensation of other species, e.g. neon [74]. In the first subsection it will become obvious why a magnetic trap naturally works well for a cloud of He*. Thus, a magnetic trap offers the most straightforward method to achieve Bose-Einstein condensation and its theoretical background, implementation, results, and consequences will be discussed in this section.

2.8.1 The theoretical considerations for a magnetic trap

From eq. (2.12) it follows that depending on the magnetic sublevel the energy can shift to higher or lower energies. This can be used to trap neutral atoms with a magnetostatic trap [117–119]. The force experienced by an atom in a magnetic field is given by:

$$\vec{F} = m_J \vec{\mu} \cdot \nabla |\vec{B}| \qquad (2.30)$$

A He* in its virtual ground state 2^3S_1 has three magnetic sublevels. While the m_0 state does not experience a shift in a magnetic field the energy of the m_{-1} state is lowered and the energy of the m_{+1} state is raised proportional to a magnetic field. Due to the fact that physical systems try to minimize their energy m_{+1} is called low field seeking state, while m_{-1} is called high field seeking state. As it is impossible to generate a three dimensional local maximum for a magnetic field only the low field seeking state can be trapped. This is advantageous in two situations. Firstly, the cloud is naturally spin polarized once it is trapped and Penning ionization is suppressed. Because the MOT relies on an unpolarized cloud of atoms, in subsection 2.8.4 it will be shown that it is necessary to spin polarize the atoms while the magnetic trap is switched on in order not to loose more than half of the atoms at the transfer from MOT to the magnetic trap. The second advantage is that atoms can be selectively outcoupled of the trap by transferring them to other magnetic sublevels. This is first used when runaway evaporation is enforced on the hottest atoms. But the different behavior in magnetic fields of the different sublevels is also a nice feature for the creation of the counter-propagating matter waves. There, atoms can be transferred into a magnetic insensitive state to cancel effects of any stray magnetic fields on their way to the DLD detector.

The strength of such a magnetic trap is given by how fast the magnetic field rises around the minimum. The simplest geometry to achieve such a field is the quadrupole field of anti-Helmholtz coils, which is used for the MOT as well. However,the advantage that atoms which are not in the low field seeking state are lost from the trap during evaporative cooling, is a disadvantage in this situation. The magnetic moment of the atom has to follow the field direction for the energy to be minimal. The condition for this to happen is that the rate at which the direction of the magnetic field θ changes should be smaller than the Larmor frequency[22] of the atom

$$\frac{d\theta}{dt} < \frac{\mu |B(x,y,z)|}{\hbar} \qquad (2.31)$$

The Larmor frequency is proportional to the magnitude of the magnetic field and thus, approaches zero for zero magnetic field. Thus, at low magnetic fields where the direction changes faster than what the atoms can follow the atoms end up in another state. The effect is commonly referred as Majorana spin flip, but is also captured in the problem of Landau-Zener transitions [120]. The Landau-Zener-problem looks at the probability of finding a quantum mechanical system in the

---

[22]The Larmor frequency is the frequency at which the magnetic moment precesses around an external magnetic field. Its value is related to the Zeeman energy by $1/\hbar$

upper energy eigenstate in the presence of a timevarying Hamiltonian. The minimum of the quadrupole field however is zero and thus, such a geometry offers only limited lifetimes. As the atoms at the center of the trap are mostly from the low energetic tail of the Boltzmann distribution of the cloud this loss does not lead to cooling of the cloud and should be avoided.

Even though there are schemes that circumvent the loss in the middle of the quadrupole trap, e.g. with time-average orbiting potential or a blue detuned optical plug to avoid atoms entering the region of loss [35, 121, 122], it is evident from this example that it is advantageous for a magnetic trap to offer a magnetic field offset (trap bottom). One of the most commonly used geometry is a Ioffe-Pritchard type of trap, where a "cloverleaf"[23] configuration offers 360° optical access in the plane perpendicular to the axis of the coils. A total of twelve coils (six on each side of the trap) is required to achieve the field. A set of two small coils on axis (SA-coils) carrying current in the same direction generate a harmonic potential along the y-axis. A second set of large coils on axis (LA-coils)[24] generate a constant field in the trap region. Those coils together achieve a confinement along the y-axis and can control the trap bottom. However, their field has a saddle point at the center of the trap and atoms would leave radially in the xz-plane. Four "cloverleaf" coils on each side placed off axis (CL-coils) carry current with alternating direction within one side and with respect to the other side. The superposition of their fields gives a strong linear confinement in the xz-plane and prevents the atoms to leave in those two dimensions. Fig. 2.21 shows the arrangement.

The adiabatic condition for the magnetic moment to follow the direction of the magnetic field still holds and for this configuration the lifetime of a cloud in such a trap can be calculated with [123]:

$$\tau_{majorana} = \left(2\pi\omega_{trap} \tanh\frac{\hbar\omega_{trap}}{2k_BT} Exp\left(-\frac{4\mu B + \hbar\omega_{trap}}{\hbar\omega_{trap}} \tanh\frac{\hbar\omega_{trap}}{2k_BT} \right) \right)^{-1} \quad (2.32)$$

Fig. 2.22 shows that for a typical system below a trap bottom of $2\,G$ the lifetime of the atoms in the magnetic trap become limited by Majorana spin flips. This is more pronounced at higher temperatures as the atoms move faster in the trap and experience a faster change of the direction of the magnetic field.

The geometry of an Ioffe-Pritchard type trap is fully defined by three parameters. The axial curvature $B_y'' = \frac{\partial^2 \vec{B}(0)}{\partial y^2}$ is produced by the small coils on axis; the clover leafs off axis are responsible for the radial gradient $B_r' = \frac{\partial \vec{B}(0)}{\partial x} = \frac{\partial \vec{B}(0)}{\partial z}$; and the large coils on axis define the trap bottom $B_0 = |\vec{B}(0)|$ by subtracting an almost constant field from the field produced by the small coils on axis. With this parameters it is possible to calculate the magnetic field strength in cylindrical coordinates:

$$|\vec{B}(y,r,\varphi)| = \sqrt{(B_r'^2 - B_0 B_y'')r^2 + (B_0 + B_y'' y^2)^2 - 2B_y'' B_r' y r^2 \sin 2\varphi + B_y''^2 r^4/4}$$

$$(2.33)$$

---

[23]The name stems from four small coils placed off axis on each side giving the coil arrangement the shape of clover.

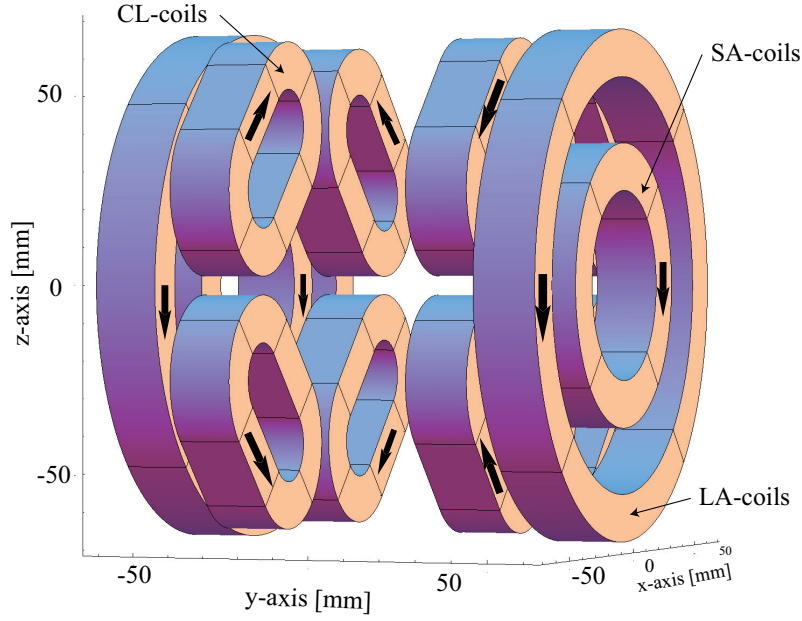[24]The same coils are used for the MOT but in anti-Helmholtz configuration

Figure 2.21: The coil arrangement to achieve magnetic trapping of He*. The two small coils on axis achieve trapping along the y-axis, the two large coils on axis generate an offset and the small coils off axis confine the atoms radially. The arrows indicate the direction of current in each coil during operation of the magnetic trap.

A peculiarity is that the trapping potential is linear in radial direction but becomes harmonic in the center where the trap bottom is generated to avoid Majorana flips. The radius where the transition from linear to harmonic regime happens is determined by the condition $(|\vec{B}(\vec{r})| - B_0)/B_0 < 1$ for the trap to be harmonic. In a strong magnetic trap with low trap bottom this radius can be as small as $200\,\mu m$. Thus, a large thermal cloud of atoms extends wide into the linear regime, from which the evaporative cooling will benefit as will be seen in chapter 2.9.1. Once the motion of the atoms is governed by the harmonic regime however, the trapping frequencies of the trap can then written as

$$\omega_{rad} = \sqrt{\frac{\mu}{m}(B_r'^2/B_0 - B_y'')} \qquad (2.34)$$

$$\omega_{ax} = \sqrt{\frac{2\mu B_y''}{m}}$$

Experimentally ω_{rad} and ω_{ax} can be adjusted independently by changing the currents in the CL-coils and SA-coils, respectively. However, ω_{rad} also depends on the trap bottom which can be controlled by the LA-coils. So by increasing the current in those coils the trap bottom can be lowered and the trap becomes more stiff in radial direction, compressing the atomic cloud.

When capturing a thermal cloud of atoms the efficiency at which this happens is limited by the trap depth. If the atoms have a higher energy than the energy depth of
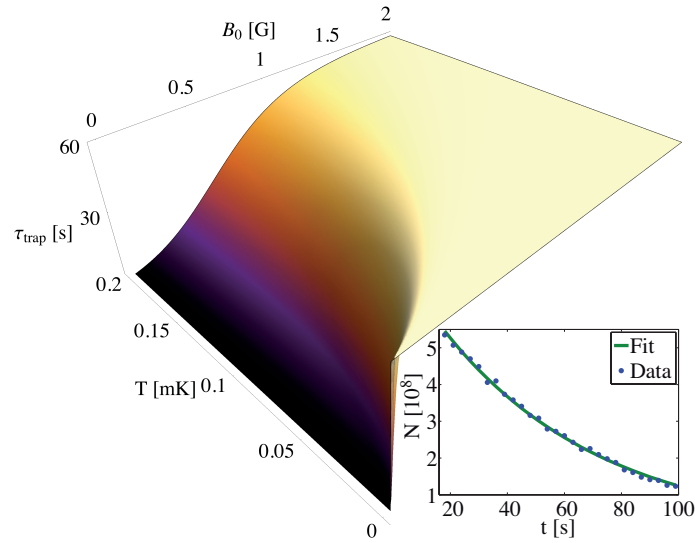
Figure 2.22: The influence of Majorana flip loss in the cloverleaf trap. As the trap
bottom becomes too low the Larmor frequency of the atoms decreases
at the center of the trap as well. As a result the atoms cannot follow
the change of the magnetic field anymore and undergo Landau-Zener
transitions to the untrapped magnetic substates. Hence, the lifetime
becomes limited by Majorana spin flips for magnetic fields below $1\,G$
and drops below $60\,s$. The inset shows a measurement of the lifetime in
the uncompressed magnetic trap yielding $\tau_{loss} = 55\,s$

the trap, they will escape. The cloverleaf trap has four saddle points where this can
happen. Those are typically some mK higher than the trap bottom. This requires
the cloud to be loaded into the trap to be $\leqslant 1\,mK$ and explains why a magnetic
trap cannot be directly loaded from the Zeeman-slowed beam. In chapter 2.8.4 it
will be shown that even for the transfer from a MOT extra precautions are required
to achieve efficient loading.

2.8.2 The realization of the magnetic trap

In the previous subsection it was shown that a magnetic trapping potential with
an offset at the center can be achieved using a cloverleaf configuration, i.e. a set
of twelve coils. This offset makes the cloverleaf configuration superior over a simple
quadrupole field. However, two coils in anti-Helmholtz configuration generate easily
high magnetic gradients thus, achieving stiff trapping with little current. In contrast,
a cloverleaf trap requires a considerable amount of current to generate a confining
potential. Especially, because the coils have to be placed fairly far away from the
trap center due to the large volume of the MOT and the diameter of its laser
beams. Additionally, the load of the MCP detector will be attached to the vacuum
chamber hosting the MOT and magnetic trap. Thus, a glass cell would be exposed
to considerable stress and might break. In this experiment reentrant flanges are used

to bring the coils as close as $\pm 25\,\mathrm{mm}$[25] to the trap center. The reentrant flanges have another inner tube that makes it possible to have the thick viewport for the MOT beams behind the coils. Thus, the coils are closer to the trap center however, they cannot be removed without breaking the vacuum[26].

The coils itself are wound out of $4 \times 4\,\mathrm{mm}^2$ rectangular copper tubes with a $2 \times 2\,\mathrm{mm}^2$ hollow core to be cooled from the inside using $16\,^{\circ\circ}\mathrm{C}$ cold water (at $6\,\mathrm{bar}$). Each coil has three layers with three windings each. The diameter of the coils is given by the geometry of the reentrant flanges. The SA coils are optimized with an inner diameter of 51 mm, just big enough to be pushed over the knife edge of the viewport flange. The flange itself is assembled after the magnetic trap is inserted. The diameter of the LA coils (112 mm) is given by the inner radius of the reentrant flange and some extra space to guide the tubes for the CL coils to the back. The CL coils need to be fit between those two dimensions. Squashing them to racetracks gives a little bit more circumference[27]. The straight part of the racetrack is 25 mm and the inner radius of the turns is 10 mm. For getting the coils in the right shape the blank tubes are annealed to relief thermal stress from the copper. Without any further bending the wire is then taped with $50\,\mathrm{\mu m}$ thick Kapton to insulate the individual coils from each other without adding to much space between them. Kapton was chosen primarily due to its thickness, good heat resistance, and electric insulation. The heat resistance is required as the insulation should not be destroyed during bake out of the vacuum chamber, which is done at about $180\,^{\circ}C$ and after the coils are inserted. Even though, the thickness of Kapton is advantageous to achieve a tight winding of the coils, it also makes the manufacturing a delicate process. Shells that guide the wire into the next layers are necessary to keep a tight arrangement of the coils, while at the same time avoid the copper tubes to bend such that edges can punch through the Kapton and cause short circuits. The coil holder for the coils was made out of Teflon, again due to its insulating and heating characteristics. The holder fixes the coils already in their designated positions and only the rotational degree of freedom for the whole assembly remains free when the coils are attached to the vacuum chamber. All tube endings are then guided out of the reentrant flange and are connected there to water tubes and the current carrying wires (the wire cross-section is $50\,\mathrm{mm}^2$ for the LA coils and $2 \times 50\,\mathrm{mm}^2$ for the SA and CL coils) from the power supplies.

For theoretical modeling it is necessary to take the finite thickness of the coils into account. This is again done using Radia. With this package the required coil geometries are determined. Some additional coils are wound and all individually characterized by measuring the magnetic field on their axis. Comparing them to the theoretical model and among each other the best ones where chosen and assembled. Each set of one side is then measured again in its complete arrangement and from

---

[25]Another set of reentrant flanges is available to bring the coils 5 mm closer at the cost of clipping the MOT laser beams

[26]Small and quick changes can be done by maintaining a small overpressure of nitrogen inside the vacuum chamber, avoiding a bake out process.

[27]Some setups make use of kidney shapes for the clover leafs to improve the trap even more. However, simulation did not show a significant improvement to justify the additional complication of manufacturing the CL coils in that shape. Hence, the second generation of the magnetic trap uses racetrack shaped CL-coils.
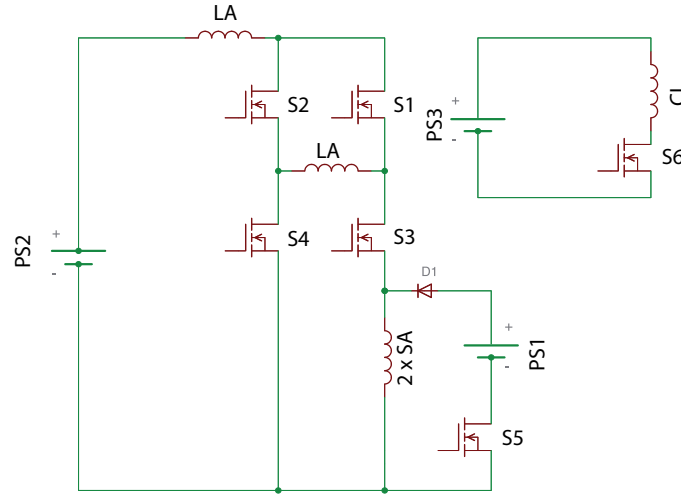
Figure 2.23: The schematic of the electronics to switch the currents for the magnetic fields. In the MOT configuration only S1 and S4 are closed. For the magnetic trap S1 and S4 open and all others close. This way the current of PS1 is added to the current from PS2 and runs through the SA coils. The current of PS2 runs first through the LA coils where the direction in one of the coils is reversed with respect to the MOT configuration. PS3 provides exclusively the current to the CL coils.

this the theoretical model is adjusted to predict the values for the final magnetic trap.

The current is supplied by three Delta Elektronika (SM15-100, SM30-200, and SM15-400) power supplies. The current through the LA coils is supplied by the SM30-200 (PS2). The same current passes through the SA coils. However, the SM15-100 (PS1) adds extra current for these coils. The SM15-400 (PS3) is exclusively to supply the current for the CL coils as they need the highest current for the radial confinement. Fig. 2.23 shows a schematic of the electronic setup, including the basic function of power IGBT based switches to make the currents turn on as fast as possible[28]. Within 1 ms the current is supplied and takes another 5 ms to settle. This is essential as the cloud released from the MOT should not be allowed to expand too far into regions where the atoms would experience a high magnetic potential when the magnetic trap is switched on, thus leading to heating of the atoms.

The switch on characteristics of the magnetic trap can be optimized by means of a PID. A major challenge in operating the magnetic traps is to keep the magnetic fields stable. Fluctuations of the fields can cause heating in the trap, counterproductive to the cooling process. In addition, the temperature after the evaporative cooling is given by the frequency of the rf knife with respect to the trap bottom. If the trap bottom is fluctuating the temperature of the cloud after evaporative cooling will be different. As the trap bottom is defined by the difference of the two large fields of LA and SA coils, the current must be stabilized. In the current system this means

---

[28]When in the next section the transfer between the MOT and magnetic trap is described it will be explained that too fast switching would cause problems as well. However, with the present system it is impossible to get into this regime.

a relative stability of 10^{-5} to achieve a stability on the order of tens of kHz[29]. A feedback loop to control the coupled system of two plus one power supplies. Three flux-gates (IT 400-S Ultrastab, LEM Danfysik) are used to transduce the current by a factor of 10^3, working on a zero-flux principle to compensate the flux of the current carrying wires. The currents after the current transducers are then measured as voltage drop over a precision resistor (VCS3322Z, $5\,\Omega$,Tolerance 0.1%,Vishay). The setpoint of the PID controlling the feedback loop is given by a programmable digital to analog converter (Flex DAC, WieserLabs) which generates the ramp for the compression. After the ramp the set point reference can be swapped to a highly stable reference as after the ramp a sub mV stability is required.

2.8.3 The process management of the system

Up until the magnetic trap the system can run in a continuous mode. The laser system, source, and magnetic fields can keep all their values to achieve the steady state in the MOT. However, for proper imaging and especially for loading the magnetic trap a precise control of timed sequences is necessary. A detailed description of the computer control can be found in the dissertation of Michael Keller. But starting with magnetic trap it is impossible to proceed without the computer control. The main components are briefly introduced here as well. In short, a LabView interface serves as GUI to an field-programmable gate array (FPGA) (cRio-9104, National Instruments), which in real time sends commands to the respective devices: the rf generators are set over an ethernet connection, the programmable digital to analog converter (FlexDAC) for the magnetic field ramp and a direct digital synthesizer (DDS) to generate the rf signals for all AOMs are set over an RS232 connection, and various TTL signals trigger the afore mentioned devices when the sequence runs. TTL signals are also sent to the vacuum shutter and valve to block the atomic beam, to the laser beam shutters, and the switch for the magnetic trap currents. Analog signals control the current of the second Zeeman slower section, of the offset coils, and of the LA coils in MOT-operation. The FPGA has also analog inputs to monitor various parameters during the experiments. This way the system can be deterministically controlled in principle on a $40\,\text{MHz}$ time scale. Another independent FPGA (equipped with an SMS module for notifications) is set up to control valves behind all turbo pumps and another one in front of the DLD as well as between Zeeman slower and collimation stage to react upon any failure and protect the ultra high vacuum. This FPGA monitors all pressures, the vacuum pump status, the electricity in the laboratory, and the temperature of the cooling water.

2.8.4 The trap transfer

The magnetic trap is able to trap atoms with a temperature of about $1\,\text{mK}$. However, the MOT does not cool the atoms down to the Doppler limit and furthermore, between switch off of the MOT and switch on of magnetic trap the atoms can expand. To reduce both effects a short $0.3\,\text{ms}$ long laser pulse of near-resonant light ($\sim \Gamma$)is applied in three dimensions while the magnetic field of the MOT decays

---

[29]For comparison in section 2.9 the BEC is achieved about $150\,\text{kHz}$ above the trap bottom hence, leaving not much space for fluctuations in the currents to occur

($\sim 0.9 I_s$). This optical molasses pulse cools the atoms to $800\,\mu K$ and prevents their expansion. This force is not position dependent anymore. Offset coils though, can generate a few G strong fields at the MOT position. This way the MOT itself is moved, such that it has the best overlap with the magnetic trap, and the atoms can be steered to some extent during the molasses pulse.

The second phase of the transfer from one trap to the other one happens during the switch on of the magnetic trap. While the field rises a strong laser pulse is applied along the y-axis for $0.3\,\mathrm{ms}$ ($\sim 7 I_s$). The magnetic field is now pointing over the whole range of the trap in direction of the y-axis and defines the quantization axis. While the laser traveling the opposite direction is exactly the same as it was in the MOT case, still pumping a σ^+-transition. The MOT laser traveling along the positive y-direction would now drive a σ^--transition and thus, the handedness of this beam has to be reversed. To couple to the same MOT telescope as the MOT laser the same PM-fiber has to be used. However, the spin polarization beam has to have opposite polarization and thus, the coupling to the fiber has to happen after a non-polarizing beam splitter. This causes the afore mentioned seventh laser output of the cluster. The two lasers together blue detuned from the atomic resonance but red detuned to atoms in the magnetic trap. This way they are a little bit cooled but more importantly the laser first depopulates the m_{-1} state and a fraction of time later the m_0 state as the magnetic trap field rises. Thus, just as at the beginning of the Zeeman slower, but now in time, the atomic sample becomes spin polarized, where all atoms are in the low field seeking state. Hence, to achieve efficient polarization the field must not rise too fast. Fig. 2.24 shows a transfer without and with the spin polarization pulse applied. The transfer efficiency can be increased by about a factor of three corresponding to the magnetic degeneracy still existing in the MOT cloud.

The last part of the transfer is already within the magnetic trap. The currents have been switched on to their final values for the uncompressed trap (SA coil current $C_{SA} = 168\,A$, LA coil current $C_{LA} = 70\,A$, CL coil current $C_{CL} = 140\,A$). In this situation the trap depth is defined by the magnetic field strength at the walls of the reentrant flange as the saddle points are further outside. The fields reach at the walls only a value of $39\,G$, which results compared to a trap bottom of $20\,G$ in a trap depth of $5\,\mathrm{mK}$ and is certainly too wide for a cloud with temperature of almost $1\,\mathrm{mK}$. In order to maintain the density of the MOT the atoms are therefore cooled by a delicate laser beam for a period of $1.2\,\mathrm{s}$ ($\sim 0.008 I_s$). In contrast to the molasses pulse at the beginning of the transfer, this time only the beams in the y-direction are used, maintaining the high degree of spin polarization. However, due to the high density of atoms the emitted photons are reabsorbed and cool additionally to the elastic collisions among the atoms in the other dimension [124]. Fig. 2.25 shows how the radial component is getting cooled when the power is increased, demonstrating this effect. The efficiency of the cooling process strongly depends on the density that mediates the reabsorption of scattered photons. Hence, without the spin polarization no efficient 1D cooling is possible.

2.8.5 The performance of the trap

During the evaporative cooling most of the atoms will be sacrificed for a small fraction of ultra cold atoms condensing into a BEC. The evaporation is more efficient
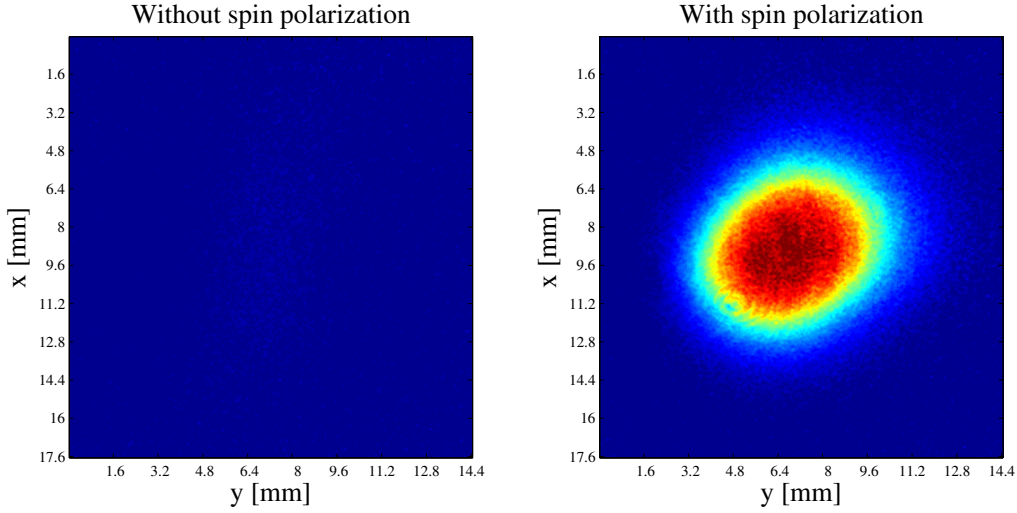
Figure 2.24: A strong laser pulse from two beams propagating in $\pm y$-direction spin polarizes the atomic sample during loading of the magnetic trap. Without the polarization about two third of the atoms in the MOT are lost for the magnetic trap, significantly reducing the number of atoms in the magnetic trap. With the low density 1D cooling does not work efficiently as shown by the two images of cloud after the 1.2 s of 1D cooling within the trap and 3 ms time of flight.

the more elastic collisions occur, throughout the process. Even at the beginning of the process a high phase space density fertilizes an efficient cooling process. In the previous subsection all the various stages to achieve the highest phase space density available were described. From the 10^9 atoms in the MOT about 90% are transferred to the magnetic trap. After the one-dimensional cooling stage they have a temperature of $100 \, \mu K$. Thus, the phase space density has increased from the MOT by a factor of 10 to 10^{-6} in the magnetic trap.

The science chamber is equipped with a large turbo pump (HiPace 700, Pfeiffer Vacuum) to achieve a good base pressure. A second turbo pump (HiPace 300) at the back of the chamber is supposed to pump out as many atoms as possible that were not captured in the MOT. With these two a pressure of very low 10^{-9} mbar was achieved before bake out. After a good week at a temperature of about $180 \, ^\circ C$[30] the pressure in the science chamber drops to the low 10^{-10} mbar. A titanium sublimation pump can be used on a daily basis to bring the pressure well into the 10^{-11} mbar[31]. With this pressure and the valve in front of the Zeeman slower closed the lifetime of the uncompressed trap is ~ 60 s. When the currents are ramped to the compressed situation care has to be taken that no resonant light can enter into the chamber. This is achieved easily as all light is prepared separately on a different optical table and then transferred via glass fibers. Therfore, closing all shutters and the doors of the

---

[30] The DLD must not be heated above $150 \, ^\circ C$. Everything else is rated to at least $200 \, ^\circ C$ if all unnecessary (electronic) equipment is detached.

[31] A VAT valve (DN200 UHV slide gate, VAT) at the connection to the DLD has to be closed in order not to cover the MCP with titanium and destroy it.
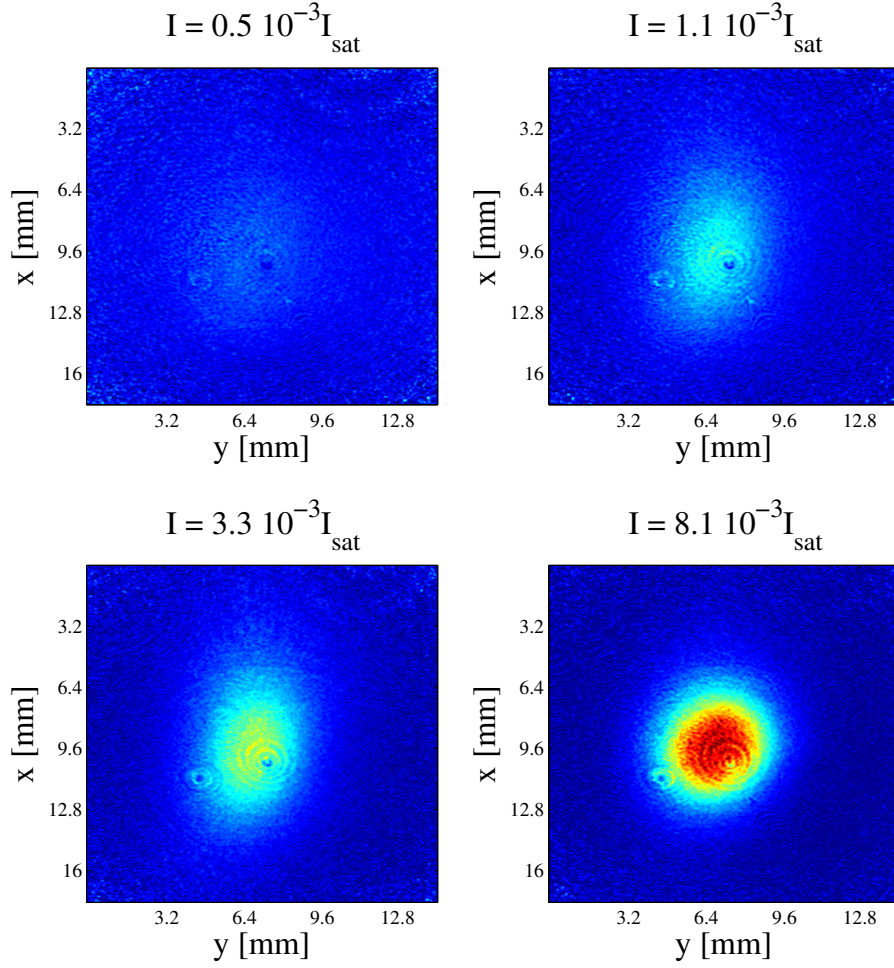
Figure 2.25: A sequence of images with increasing power during the 1D cooling stage. When more and more photons are scattered from the cold cloud the atoms begin to be cooled first axially and eventually in the radial direction as well, where there are no cooling laser beams.

table is sufficient to maintain a background gas limited lifetime on the same order as in the uncompressed scenario. A small effect of the Majorana flips is expected if the trap bottom is lowered below $1\,G$ however, from fig. 2.22 it is expected to lose importance as the cloud is cooled and the trap bottom is typically kept between $1 - 3\,G$.

To characterize the magnetic field the trapping frequencies and trap bottom can be measured. In the uncompressed situation a small displacement[32] of the cloud during loading and a sudden release lets the cloud oscillate in the trap. From the oscillations (compare fig. 2.26) trap frequencies can be inferred. With an rf knife the trap bottom can be sampled (see fig. 2.27). The values for the radial trap frequency $\omega_{rad} = 52\,Hz$, axial trap frequency $\omega_{ax} = 30\,Hz$, and for the trap bottom $B_0 = 20\,G$ match well to the simulated parameters. The measurement for the trap bottom is

---

[32]A displacement can easily be achieved by means of the offset coils.

Figure 2.26: If the magnetic trap is displaced with respect to its original position by means of the offset coils and suddenly released, the cloud starts to oscillate in the trap at the frequency of the trap. In the uncompressed trap the cloud oscillates in a harmonic potential with $\omega_{rad} = 2\pi \cdot 55\,\mathrm{Hz}$ and $\omega_{ax} = 2\pi \cdot 32\,\mathrm{Hz}$ matching the simulations for the coils.
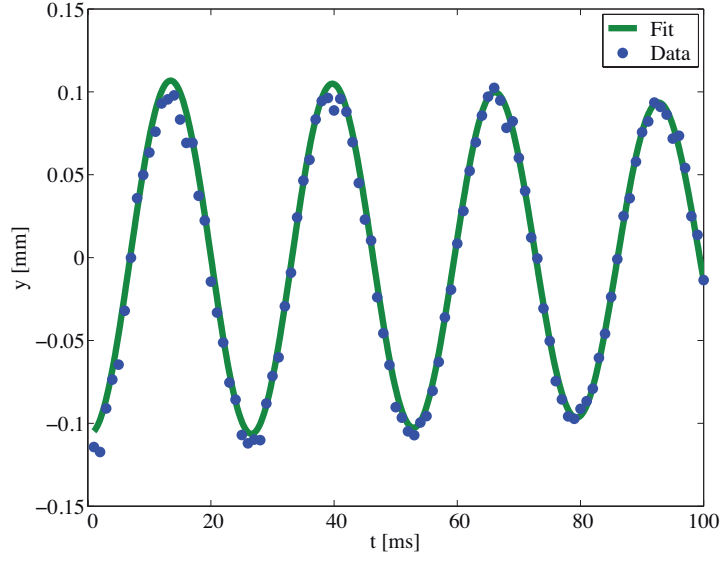
fitted with

$$\frac{N_r(f_{rf})}{N_t} = 1 - \frac{2}{\sqrt{\pi}} \exp\left(-q(f_{rf})\right)\sqrt{q(f_{rf})} + \mathrm{erf}\left(\sqrt{q(f_{rf})}\right) \qquad (2.35)$$

where $q(f_{rf}) = (hf_{rf} - B_0\mu/k_bT)$ and hence, the temperature T of the cloud is a fit parameter. The $250\,\mu\mathrm{K}$ match with time of flight measurements with absorption imaging.

Before evaporation the magnetic trap is compressed within $1.5\,\mathrm{s}$ to a SA-coil current $C_{SA} = 238\,\mathrm{A}$, LA-coil current $C_{LA} = 140\,\mathrm{A}$, and CL-coil current $C_{CL} = 360\,\mathrm{A}$. As a consequence the trap becomes much more anisotropic with the y-axis being least stiff. With these currents the trap has an axial curvature of $B_y'' = 8\,G/\mathrm{cm}^2$, a radial gradient of $B_r' = 83\,G/\mathrm{cm}$, and a trap bottom of $B_0 = 2\,G$. The extreme radial gradient manifests itself in an efficient evaporative cooling process and is helpful to achieve degeneracy of the metastable helium gas.

Planned improvements

The stability of the trap is of outmost importance for the reproducibility of the experiment. Especially, fluctuation of the trap bottom changes the condition when degeneracy is achieved. Stabilizing the currents through the coils as well as mechanical stability is required to have continuous operation with ever the same quality. For this the precise current sensors of Dan-fysiks has been set up as well as a next generation magnetic trap is under construction. Besides slightly improved coils this
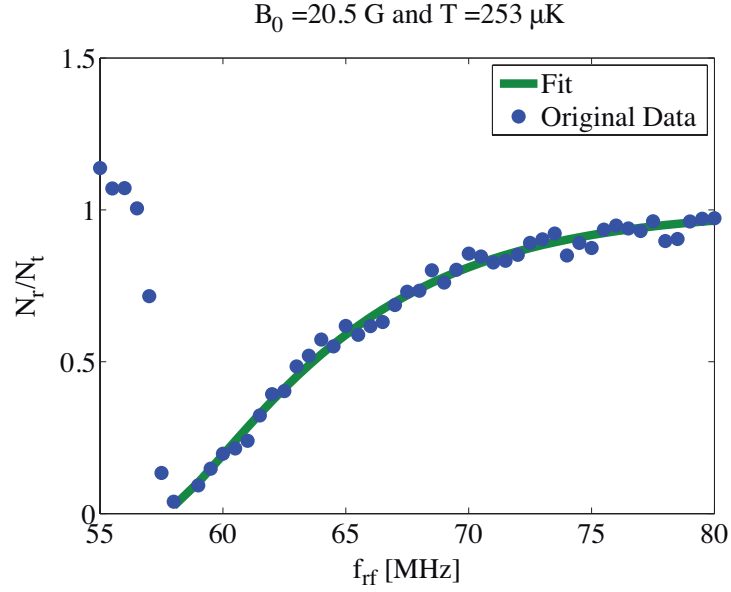
Figure 2.27: With an rf knife all atoms with energies above the rf frequency are spilled out of the trap. Monitoring the remaining atoms maps out the energy distribution of the atoms in the magnetic trap and reveals the trap bottom at which no atoms remain in the trap. In the uncompressed trap the trap bottom is around $20\,G$ and is lowered for the compressed trap to $2\,G$. The temperature is a fit parameter and can be determined from the measurement as well.

will in particular have higher mechanical stability. The whole assembly will be one massive block filling the whole reentrant flange and will be firmly attached to the vacuum chamber.

On a somewhat bigger conceptual change, an optical dipole trap is planned. Following eq. (2.5), a single focused laser beam can achieve three dimensional spatial confinement if the laser is red detuned. Dichroic mirrors, reflective for 1083 nm but transmissive for 1550 nm (AdjustiK E15-10, Koheras + CEFA-C-PB-HP-PM-40-NL1-OM1-BT203-FA-FA, Keopsys), can either be placed along the y-axis coupling to the beam path of the MOT-beams, or on the z-axis to inject the beam from the above. The laser power is much more easier to stabilize than the high currents in the magnetic trap and with the different viewports to align the trap offers a higher flexibility on the geometry of the trap. For example, aligning the major axis with the z-axis will provide the possibility to make use of the high temporal resolution of the delay-line detector as well as a way to test for the influence of gravity in later experiments. However, in chapter 3.1 it will be discussed how a Raman transition can be used to release some atoms out of the magnetic trap without the requirement to switch the trap off. Such a convenient transfer is not possible with an optical trap.

2.9 The Bose-Einstein condensation

The energy of an atom in a thermal cloud is characterized by its temperature and follows a Maxwell-Boltzmann distribution. In the vicinity of a trapping potential and in the regime of low temperatures the energy eigenstates become discrete and so does the distribution. In order to be able to calculate the total energy of the system the macroscopical occupation of the ground state is taken to be zero. However, when the chemical potential drops below the energy for the first excited state any additional atom is filled into the ground state and thus, the ground state becomes macroscopically populated. This indicates a phase transition at which the atoms condense into a Bose-Einstein condensate where the ensemble of millions of atoms can be described by the single particle wave function. This section describes the last step to cool He* below the transition temperature T_c and demonstrates experimentally some basic features of a BEC.

2.9.1 The evaporative cooling

After compression of the magnetic trap about 10^9 atoms are trapped in a volume of about $1{\times}1{\times}3\,\mathrm{mm}^3$ and have a temperature of $1\,\mathrm{mK}$. Thus, there are still seven orders of magnitude missing in the phase space density to achieve condensation. Further optical cooling is not possible because of the limiting recoil velocity. However, atoms with higher energy than the trap depth of the magnetic trap can leave the trap. These atoms carry away more energy than the average energy per atom. Thus, the average energy per atom decreases when such hot atoms leave the cloud. After the energetic loss the atoms rethermalize through elastic collisions again yielding a lower temperature.

In principle there is a finite probability that an atom gains so much energy to leave the magnetic trap on its own. Therefore in principle, the cloud gets colder and colder the longer one waits. Evaporative cooling, on the other hand, only works efficiently if the phase space density increases as well. The lifetime of an atom is limited by background collisions[33]. Thus, if such bad collisions with background atoms outbalance the good elastic collisions and the time for a high energetic atom to carry away more than the average energy, the loss of atoms leads to loss in density. Hence, by waiting for an atom to leave the trap the cloud might get smaller and no increase in phase space density would be achieved even though the temperature falls.

An elegant way to change the trap depth without changing the trap stiffness is to use an rf knife. This is a single sharp frequency to truncate the trap on a well defined surface. The effect of the rf is to flip the magnetic moment of the atom to an untrapped state thus, selectively releasing atoms from the magnetic trap. As atoms with higher energy can climb the potential further up and experience higher magnetic fields they get resonant with higher rf frequencies. This gives the experimentator an easy handle to remove hot atoms from the trap. Once the atoms are removed the remaining atoms undergo collisions, scatter new atoms in the higher lying energetic states and those are removed again until the cloud settles at a new temperature.

---

[33]Three-body collisions and detrimental penning ionization are sufficiently suppressed to not play a role in the evaporative cooling scheme

This is the moment when the rf frequency is changed again to truncate the trap at even lower trap depths. This process can be described by the ratio ν between the change of temperature relative to the current temperature T and the change of atom numbers relative to the current amount of atoms N

$$\nu = \frac{\dot{T}/T}{\dot{N}/N} = \frac{d(ln(T))}{d(ln(N))} \tag{2.36}$$

Eq. (2.36) shows that this process happens on a logarithmic scale. In a trap without any other loss mechanisms, the best (even though slow) strategy would be to just wait until energy states are populated spontaneously that are able to leave the trap in order to achieve a cold while still large cloud. In practice though, a logarithmic scan with a time constant τ_{ev} for the truncation frequency is optimal. In this system only a single logarithmic scan is implemented but in general it might be better to adapt the time constant of the ramp from time to time during the cooling process. The so called runaway regime is entered when one achieves a constant or increasing rate of the elastic collisions $1/\tau_{el}$, indicating a stable density. For this to happen the lifetime in the magnetic trap τ_{loss} has to be large

$$\tau_{loss} > \frac{\tau_{ev}}{\nu(\gamma - 1/2) - 1} \tag{2.37}$$

In eq. (2.37) it was implicitly assumed that the rate of elastic collisions must be much larger than the rate due to losses. The parameter γ is defined such that the volume scales as T^γ and depends on the dimensionality of the trap, e.g. $\gamma = 3/2$ for a harmonic trap and $\gamma = 3$ for a linear potential whereas it is zero for a box potential.

From eq. (2.37) and the parameter γ it can be seen that a linear trap potential is beneficial for an evaporative cooling scheme. This can be understood as a compression effect. When the atoms become colder they are also pushed further towards the center of the trap than in the case of a harmonic potential. Thus, the density of the atoms increases more than what would be accomplished by a harmonic trap. This remains valid when the trap has a harmonic potential in one dimension as it is in the cloverleaf trap.

The rf frequency is generated by an arbitrary waveform generator (81150A, Agilent) which can be programmed via ethernet in different modes (exponential and linear ramp, constant frequency) and gets a TTL-pulse triggers (for a gate-mode operation) when the ramp should start. This signal is then amplified by a rf amplifier (BSA 0125-25, Bonn Elektronik) up to $25\,W$. A second rf frequency can be fed to the amplifier from an rf signal generator (SMA-B103, Rohde&Schwarz). Via BNC feedthroughs the signal is guided into the vacuum chamber, where two square coils with $48 \times 50\,mm^2$ area are placed at $z = \pm 30\,mm$. These are connected in Helmholtz configuration to produce an approximately homogenous magnetic field at the position of the trapped atom cloud. Each of the coils consists of five windings of enameled, vacuum compatible wire on a Teflon frame to support it. They are placed such that they are close to the trap but clip as little of the MOT laser beams as possible. The coils have only a marginal impedance for the rf signal. To reduce the backreflection of the high power signal it is attempted to match the $50\,\Omega$ output of the amplifier with a $50\,\Omega$-terminator in series with the coils.
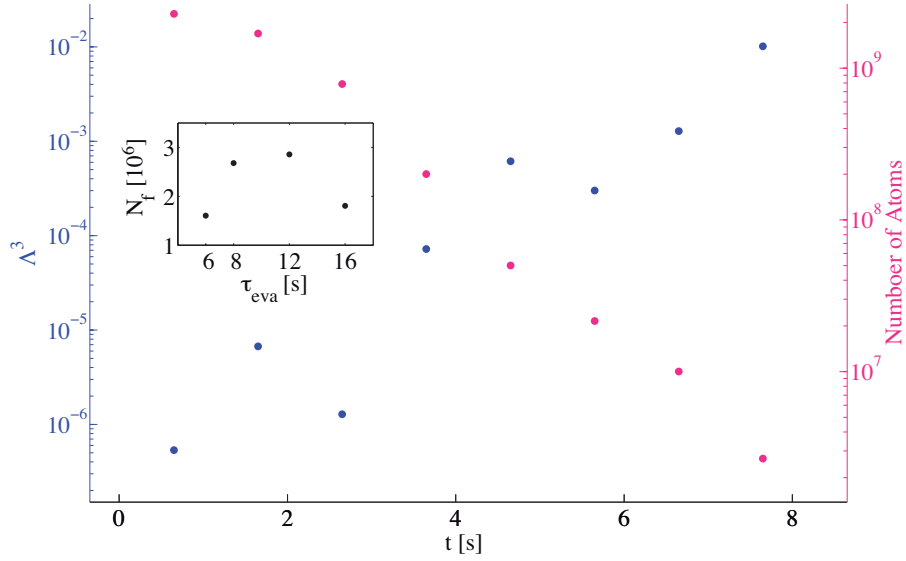
Figure 2.28: The phase space density increases during evaporative cooling as the temperature approaches the transition temperature. A ramp with time constant 8 s is interrupted in between to measure the temperature in a time of flight measurement. While the number of atoms decreases the density increases as well as the deBroglie wavelength and hence, the PSD approaches values close to unity (above for the BEC). The inset shows the dependence of atom numbers after the ramp N_f on the time constant of the rf ramp τ_{eva}. For too short time constants the too many atoms are spilled out of the trap before rethermalization. For too large time constants too many atoms are lost because of background collisions.

Fig. 2.28 shows how the phase space density of a sample increases during this final step of evaporative cooling of a cloud. The rf ramp is typically ramped from 75 MHz to 150 kHz above the trap bottom ($B_0 = 1.6\,G$) within 8 s.

2.9.2 The basic features of a BEC in matter wave experiments

When the phase space density $\Lambda^3 = n/\lambda_{dB}^3$, i.e. the density of atoms n per de Broglie wavelength $\lambda_{dB} = \sqrt{2\pi\hbar^2/mk_BT}$ cubed, approaches unity the wave packets of all atoms start to overlap. This means each atom can be found within a volume which is already occupied by another one. Thereby the atoms become indistinguishable as no defined position can be assigned anymore to individually identify them. For a harmonic trap the condition for the transition is:

$$\Lambda^3 > 1.202 \tag{2.38}$$

As the density in a harmonic trap is defined by the geometric mean of the trap frequencies $\bar{\omega} = (\omega_{rad}^2\omega_{ax})^{1/3}$, eq. (2.38) can be used to relate the transition temper-

ature T_c to the number of atoms N

$$T_c \approx 0.94\hbar\bar{\omega}N^{1/3} \tag{2.39}$$

The transition temperature for a Bose-Einstein condensate in dilute gases with about a million helium atoms is around $1\,\mu K$. Once the atoms are cooled below the transition temperature and compressed to densities high enough such that the phase space density fulfills eq. (2.38) the atoms start to macroscopically occupy the ground state of the harmonic trap and condense into the Bose-Einstein condensate. They are all indistinguishable from then on and thus, the many body system can be described by a single particle wave function. This can be used for the Gross-Pitaevski equation, which adds an interaction term to the single particle Hamiltonian:

$$\left(-\frac{\hbar}{2m}\nabla^2 + V(\vec{r}) + \frac{4\pi\hbar^2 a_{11}}{m}|\Psi(\vec{r})|^2\right)\Psi(\vec{r}) = \mu\Psi(\vec{r}) \tag{2.40}$$

where $V(\vec{r})$ is the external potential of the trap and μ the chemical potential. The interaction depends on the density of the particles and the scattering length a_{11}. The simplicity to use a single parameter to describe the interaction between atoms is owed to the low temperatures of the atomic cloud. At the ultra-low temperatures only isotropic s-wave scattering can occur[34] and thus, the in general complex interaction can be taken into account with a single parameter. ^{4}He in the m_{+1}-state has a scattering length of $a_{11} = 7.5\,\text{nm}$, favorable to achieve Bose-Einstein condensation.

For large atom numbers in the BEC the contribution of the kinetic energy is negligible and therefore the this term is dismissed for the Thomas-Fermi approximation. The remaining external potential counteracts the repulsive interaction, and one finds that the chemical potential, i.e. the energy to add a particle to any point in the cloud, is the same everywhere. From this and the knowledge about the trapping potential the chemical potential for a harmonic trap can be inferred

$$\mu = \frac{1}{2}\left(\frac{15Na_{11}}{\bar{r}_0}\right)^{2/5}\hbar\bar{\omega} \tag{2.41}$$

where $\bar{r}_0$ is the geometric mean of the extents of the single-particle ground-state in the three dimensions of the magnetic trap:

$$\bar{r}_0 = \sqrt{\frac{\hbar}{m\bar{\omega}}} \tag{2.42}$$

Due to the interaction the single particle ground state extent is smaller than the Thomas-Fermi radius R_{TF}, which describes the extent of the whole cloud:

$$R_{TFi} = \sqrt{\frac{2\mu}{m\omega_i^2}} \tag{2.43}$$

The one dimensional probability amplitude for an atom in the BEC is then given by:

$$|\phi(x)|^2 = \sqrt{\frac{3}{4R_{TFx}}\left(1 - \frac{x^2}{R_{TFx}^2}\right)} \tag{2.44}$$

---

[34]This will be important for chapter 4 as well where the four wave mixing process prepares an entangled state.
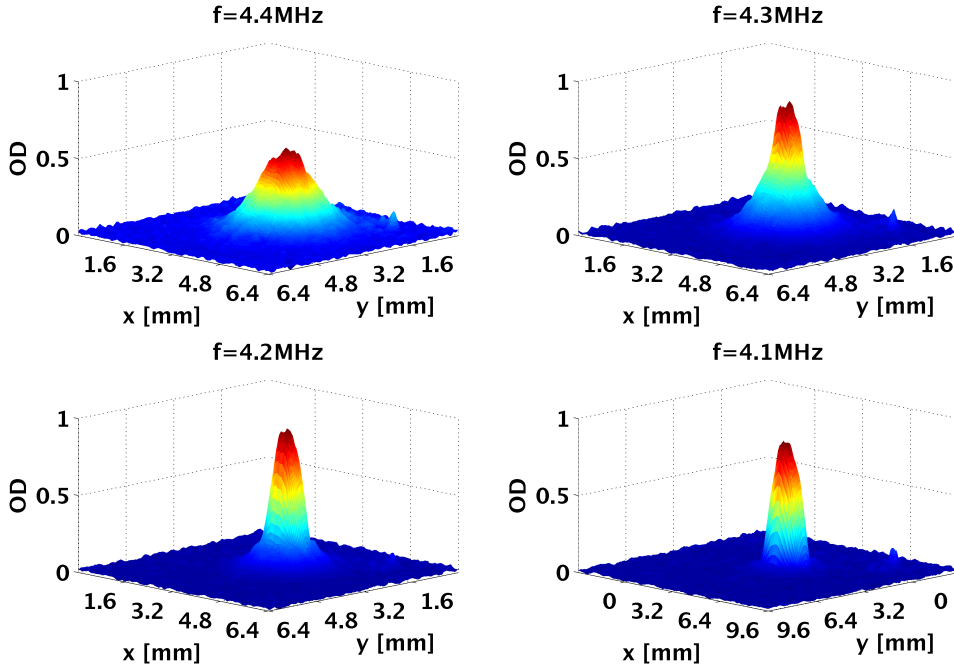
Figure 2.29: The bimodal signature of the transition to a BEC. As the transition temperature is crossed, more and more atoms condense into the ground state and a sharp inverted parabola arises out of the thermal distribution.

For a thermal cloud occupying the excited states according to the Maxwell-Boltzmann distribution the spatial shape follows a Gaussian distribution. However, the competing terms of the Gross-Pitaevski equation in the Thomas-Fermi approximation result in the fact that the potential of the trap is just evenly filled up with atoms. Hence, the atoms map the profile of the trap and the density profile of the cloud is an inverted parabola. Fig. 2.29 shows how this parabola profile arises as sharp peak in the thermal cloud as the transition temperature is crossed, termed "bimodal" distribution.

Another signature of a Bose-Einstein condensate is its ballistic expansion upon release from the trap. A thermal cloud expands isotropically and the high spatial anisotropy of the cloud in the trap cannot be seen. Conversely, a BEC only populates the lowest lying energy level. This is different for the three axes for they have different trapping frequencies. Hence, the atoms have a much higher momentum in radial direction than in axial direction. While the cloud has a much smaller extent in the radial direction than it has in the axial direction, it is expanding more rapidly in radial direction. Fig. 2.30 shows how the BEC barely expands in axial direction while the atoms burst out in radial direction. Moreover, the energies are still small compared to the thermal expansion. Hence, even before they start to spread and are too dilute to be detected by absorption imaging as in the case of the thermal cloud, gravity pulls the atoms downwards. This pulling of gravity will eventually make the atoms fall onto the DLD, which will be discussed in more detail in the next chapter.
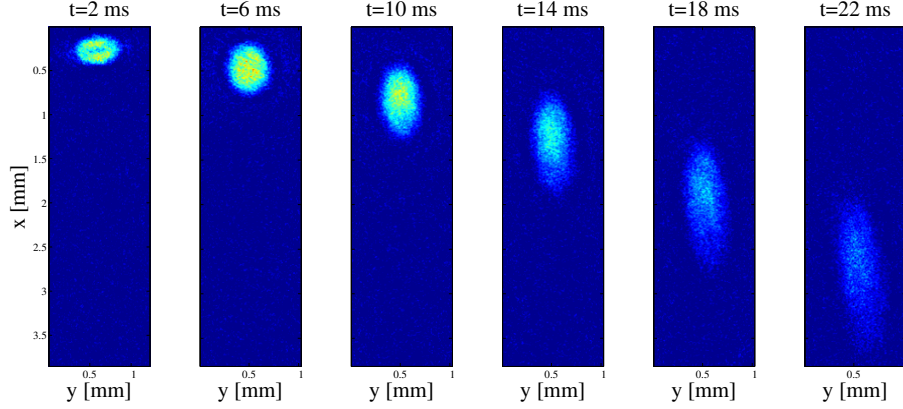
Figure 2.30: The highly anisotropic expansion of a BEC. Equivalent to the Heisenberg uncertainty principle, the atoms expand much faster in radial direction than in axial, as the confinement in the magnetic trap is radially much higher than compared to the axial direction. During free expansion the atoms are pulled downwards by gravity and expand in radial direction while the axial dimension of the BEC remains almost unchanged

Hence, the expansion is on the order of Heisenberg's uncertainty principle. However, the interaction of the atoms adds a mean field interaction energy, which contributes significantly to the free evolution of the cloud radius along the axial direction:

$$r_y(t) = R_{TF\,y}\left(1 + \left(\frac{\omega_{ax}}{\omega_{rad}}\right)^2\left(\omega_{rad}\,t\arctan\left(\omega_{rad}\,t\right) - \log\sqrt{1 + (\omega_{rad}\,t)^2}\right)\right) \quad (2.45)$$

while the radial expansion is simply:

$$r_{x,z}(t) = R_{TF\,x,z}\sqrt{1 + (\omega_{rad}\,t)^2} \quad (2.46)$$

A big challenge is the stabilization of the trap bottom. The feedback loop that stabilizes the current is an improvement. However, fluctuations of the trap bottom due to grounding problems are still on the order of $\sim 100\,\text{kHz}$. This has to be further improved to run experiments continuously. However, the current system is able to achieve routinely BECs with about $5 \cdot 10^6$ atoms, which is enough for experiments to initiate and detect entanglement. The feasibility of such experiments will be discussed in more detail in chapter 4.

3 The setup to generate and detect momentum entanglement of matter waves

The previous chapter described the system to realize a sample of ultra cold, indistinguishable particles as source for coherent matter waves. However, no entanglement of the external degree of freedom is present for the individual constituents of a BEC that could be observed. This chapter is dedicated to describe how Raman transitions can initiate a four-wave mixing process. As a result the two outgoing waves are entangled, where the feasibility of proving this entanglement is the subject of this dissertation. The first section of this chapter describes the four-wave mixing process. This includes the Raman transition and its optical setup with a spatial light modulator (SLM) as main component, as well as the four-wave mixing itself. The second section then introduces and characterizes the delay-line detector which, able to detect single particles, has the capability to detect quantum correlations.

3.1 Four-Wave-Mixing of matter waves

In order to generate entanglement between two quantum mechanical systems an interaction between the systems has to establish a fixed relation between them. In order not to have measurements on one system directly affecting the other system, ideally this interaction can be switched on and off in a controlled fashion to avoid any further interaction between the entangled systems. In chapter 2.9 it was mentioned that the interaction of two colliding atoms in the low energy regime can be described by a single parameter, giving rise to a Dirac-delta function like contact potential. This strong interaction between the collision partners, which only occurs during collision and not anymore after separation, is responsible for an entanglement creation between the two partners. Without contact the two atoms do not interact with each other anymore corresponding to a switch off of the interaction upon separation.

In principle, the collisional interactions happen all the time among the millions of atoms within a BEC. However, due to the fact that the total momenta of the atoms compared to the momenta induced by collisions are on the same order, the signature of entanglement is untraceable within the BEC. In the next sections it is described how the cursor to the signature can be magnified by employing Raman transitions, which increase the total momentum already before the collision. The description of the Raman transition is then followed by the description of the the four-wave mixing process of the collision and eventually the optical setup with an SLM.

3.1.1 Raman transitions

To excel the statistics due to entanglement in the external degree of freedom of a matter wave above the dominating statistics within the coherent state of a BEC the atoms of interest need to be outcoupled of the ensemble of atoms of the BEC. A straightforward way of doing so is to accelerate the atoms above the speed of sound of the BEC creating a quasi free matter wave. If there are two counter-propagating matter waves of this type, atoms of these waves that collide will have interacted and be far separated from the rest of the BEC after a sufficient time of flight.

The generation of such supersonic waves in a BEC is possible by means of optical transitions[1]. In chapter 2.2.1 the coupling of two energy levels of an atom was described by Rabi oscillations. The concept of Rabi oscillations allows for coherent population transfers between two states. However, in practice the short lifetime of an optically excited energy level and its decay channels to other levels renders this process not efficient for a coherent state transfer. Subsequently as in laser cooling, spontaneous emission will lead to a random second momentum transfer to the atom which obscures the signature of the process. To avoid the second random momentum transfer the atoms can be transferred back to a ground state by stimulated emission of the photon. The stimulated emission then deterministically induces another momentum kick opposite to the direction of the second laser. Typically, the two laser frequencies are close to each other such that the resulting magnitude of the momentum of the atom is $\hbar k \sqrt{(2 - 2\cos(\phi))}\vec{e}_\phi$, where ϕ is the angle between the two laser beams. If a second laser drives a stimulated transition into a level different than the initial one, coherent population transfers of up to unity can be achieved [125]. Hence, in this two-photon process three energy levels of the atom are involved (compare of fig. 3.1a). Two long-lived ground states, where one is the initial and the other one the final state that is to be populated. A third intermediate level is only virtually involved during the transfer and thus, can have a short lifetime. The intermediate level however needs to be optically addressable by the two lasers hence, needs to fulfill the typical selection rules. Variations of this idea are widely used in Bragg spectroscopy [126–128], beam splitters for matter wave [60, 61, 129], and electromagnetically induced transparency (EIT) [130, 131].

The efficiency of this two photon process increases if the intermediate excited level is only populated as little as possible. Hence, a large detuning of the two laser beams from the actual transition but a relative resonance condition to match possible energy mismatches of the initial and final states yields best results. To understand why this two photon process occurs even though the lasers are individually not resonant with the intermediate energy level the dressed state picture is usually applied. The coupling of the second laser, being off resonant with the transition of the atom, induces similar to eq.(2.5) a level splitting depending on whether a photon is present or not. Hence, the atomic transition becomes dressed with the electromagnetical field of the photon. The first laser can now be tuned such to drive a transition to the level dressed with a photon of the second laser. The excited photon is then instantaneously stimulated into the same mode as the dressing photon of the second laser and thus, does not populate the intermediate level. The atom itself ends up in the state that was coupled by the second laser to the intermediate dressed level.

---

[1]The speed of sound $c_s = \sqrt{\mu/m}$ is about an order of magnitude smaller than the recoil velocity.
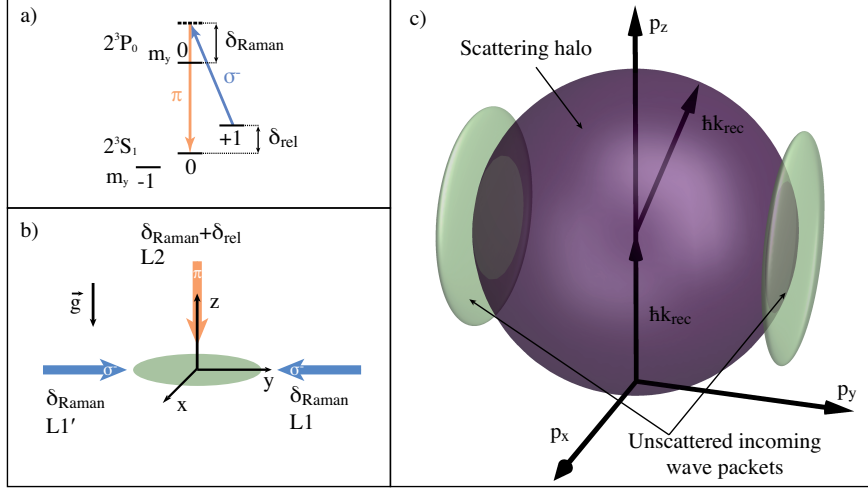
Figure 3.1: The geometry of the Raman lasers. a) The atoms are initially trapped in the m_{+1} state. A π-polarized beam dresses the excited state 2^3P_0, which is addressed with a σ^--polarized beam. This transfers the atoms into the magnetic insensitive state m_0. b) Two counter-propagating laser beams L1 and L1' transfer a momentum kick in the direction of the absorbed laser to the atoms. The absorbed photon is subsequently emitted into L2 leaving another momentum kick in the opposite direction of L2. c) Two waves counter-propagating to each other and along the y-axis are initiated, while the center of mass motion moves in -z-direction. Upon four-wave mixing (see section 3.1.2) some atoms are scattered onto a spherical halo in momentum space with radius $\hbar k_{rec}$.

As this is a coherent process again Rabi oscillations can be observed, which happen at the frequency of the two-photon Rabi frequency Ω_{12}

$$\Omega_{12} = \frac{\Omega_1 \Omega_2}{2|\delta|} \tag{3.1}$$

where $\Omega_{1,2}$ are the respective one photon Rabi frequencies from eq. (2.2). To avoid sensitivities to Doppler shifts due to the inherent velocity uncertainties of the BEC the two-photon Rabi frequency should be much larger than the Doppler shift $\Omega_{12} \gg \delta_{Doppler}$, which is on the order of a few kHz. Hence, Rabi frequencies of a few MHz are desirable. This way the population transfer also happens on much faster time scales than any change in the BEC, characterized by the trap frequencies. However, sub-μs light pulses are required to stop the transfer after half of a cycle when all atoms are in the final state.

A peculiarity of the Raman transitions is that the ground state to which the atoms are transferred is typically not the same as the initial state. In particular, transitions to other hyperfine or magnetic sublevels can be driven, which otherwise would require frequencies in the rf band or could be optically forbidden for single photon processes. The momentum transferred by a single rf photon, though is far too

little to separate the collided atoms from the BEC and thus optical transitions are favorable for this purpose. The atoms in the BEC are trapped in the m_{+1} low field seeking state. When the magnetic trap is switched off the extremely light helium atom in a magnetic sensitive state is subject to all stray magnetic fields that occur during switch off and along the atom's way to the delay-line detector. The inset of fig. 3.1a shows the relevant energy levels involved in a Raman transition. The first laser L_1 has a σ^--polarization. However, as it is off resonant with the $^3P_0$-level no absorption would happen. The second, π-polarized laser L_2, though couples the m_0 sublevel to the same excited level and in combination with L_1 can transfer atoms from the m_{+1} magnetic sublevel to the m_0 sublevel of the same state. Hence, after successful transfer, the atoms are insensitive to the field of the magnetic trap and stray fields on their way to the detector. As the $^3P_0$ is not degenerated no further coupling to the m_{-1}-state is possible and the populations only oscillate between the low field seeking and the magnetically insensitive state.

Fig. 3.1 shows the geometry of the lasers involved in the Raman transition and the subsequent motion of atoms. Another wave with opposite momentum can be initiated by a counter-propagating laser L_1' in order to have the motion of the center of mass of all atoms within the xy-plane at zero velocity. If the intensities of lasers L_1 and L_1' are equal, an equal amount of atoms are transferred to the respective momentum states creating a coherent superposition of two counter-propagating matter waves in the center of mass frame. While L_1 and L_1' have to be along the quantization axis of the magnetic trap to drive the right σ^--transition, the π-polarized L_2 can be oriented arbitrarily in the xz-plane. However, an orientation along the z-axis avoids any motion of the center of mass in the xy-plane. This way the atoms collide and subsequently separate along the y-axis, which is favorable for the devised experiment of chapter 4, where the detection of entanglement will be centered around the xz-plane. Hence, the atoms that do not undergo collisions are not interfering with the atoms of interest. In principle, one can change the geometry by employing multi pulse schemes [132]. However, the Raman transition to obtain the magnetically insensitive state is realized most easily with two counter-propagating laser beams along the y-axis.

3.1.2 Four-Wave-Mixing mechanism

The Raman transitions described in the previous subsection initiate two matter waves counter-propagating to each other. The atoms are transferred to a magnetic insensitive state and start to pass through each other. The interaction between the atoms of each wave begin a process called four-wave-mixing (FWM) in nonlinear optics. Two incoming waves interact through a nonlinear interaction with each other and initiate two outgoing waves. The corresponding Hamiltonian for this situation can be written as [133]

$$\mathcal{H} = -\int \hat{\Psi}^\dagger \frac{\hbar^2 \nabla^2}{2m} \hat{\Psi} d\vec{r} + g \int \hat{\Psi}^\dagger \hat{\Psi}^\dagger \hat{\Psi} \hat{\Psi} d\vec{r} \tag{3.2}$$

Here $\hat{\Psi}^\dagger$ and $\hat{\Psi}$ are the creation and annihilation operators of the "matter-field amplitudes" fulfilling bosonic commutation rules and are the equivalence to the electric field amplitudes in nonlinear optics. The second term gives the interaction

between the different waves. The interaction is characterized by the s-wave scattering interaction strength $g = 4\pi a_{00}\hbar/m$, which is responsible for the contact potential of the low energy atoms $V(\vec{r}) = 4\pi\hbar^2 a_{00}/m\delta(\vec{r} - \vec{r'})$. Note, that the scattering length $a_{00} = 5.3\,\mathrm{nm}$ of two atoms in the magnetic sublevel m_0 is different from the scattering length of atoms condensing to a BEC (compare chapter 2.9)[2].

As only the interaction term is of interest for the entanglement process the first term can be dropped and the interaction term written in second quantization

$$|\Psi\rangle = g_0 \oint_{|\vec{p}|=\hbar k} (\hat{a}^\dagger_{-\vec{p}} \hat{b}^\dagger_{\vec{p}} \hat{c}\,\hat{d} + \hat{a}_{\vec{p}} \hat{b}_{-\vec{p}} \hat{c}^\dagger\,\hat{d}^\dagger)|0011\rangle \qquad (3.3)$$

where each wave is given an individual name to emphasize the character of four waves mixing. Whenever a collision occurs an atom of each incoming mode (c and d) is annihilated and instead created in the outgoing modes (a and b). In order to maintain energy conservation the integral is limited to the surface of constant magnitude of momenta. In practice this is not necessarily fulfilled due to the initial momentum uncertainty of the BEC itself. However this results in a finite thickness of the surface and does not effect the entanglement, which is a result of the angle independent scattering. Hence, the atoms that collide in the four-wave-mixing process end up on a halo around the center of mass. The radius is $\hbar k_{rec}$ in momentum space with a finite width limited by the initial momentum uncertainty in the condensate.

Because of the nonlinearities in the Hamiltonian of the field operators the solutions to the equation of motion for eq. (3.2) are in general not analytically solvable. There are two approaches to model the situation. The slowly varying envelope (SVE) approach introduced by Trippenbach et al. [133] neglects mean field interactions and uses a perturbative approach to calculate the dynamics analytically. The second approach by Kheruntsyan et al. [134] does not require additional assumptions to the Hamiltonian by using a positive-P representation of the field[3]. This representation allows to write down a stochastic Fokker-Planck master equation for the fields, which then can be solved numerically.

For the SVE approach three characteristic time scales can be identified. The first is the separation time of the two clouds passing through each other

$$\tau_s = \frac{m\sigma_y}{\sqrt{2}\hbar k_{rec}} \qquad (3.4)$$

When the clouds[4] with spatial widths $\sigma_{x,y,z}$ do not overlap anymore the atoms obviously do not interact and thus do not scatter anymore as well. The two other time scales describe the evolution of the wave packets of the incoming waves itself. The nonlinear dispersion time describes the free ballistic expansion of the cloud and

---

[2]This difference in scattering length is responsible for the phase matching condition in the experiment of ref. [53, 54]

[3]The positive-P representation of phase space is an extension to the Glauber-Sudarshan P-representation for the phase space of photons. It can be shown that by extending the real Glauber-Sudarshan P-representation to a complex number phase space no negative P values exist and one can find this way solutions to Fokker-Planck master equations [135]

[4]To keep the calculations analytical Trippenbach et al. assume spherical symmetric Gaussian wave packets. In their analysis the wave packet has width $\sigma/\sqrt{2}$ however, to have the immediate relation to the RMS of the cloud here a width of σ is used.

is in the Thomas-Fermi approximation

$$\tau_{ND} = \sqrt{\frac{\pi^{3/2}(\bar{\sigma}/\sqrt{2})^5}{gN}} \qquad (3.5)$$

Leaving the mean field interaction aside the diffraction time or linear dispersion time

$$\tau_{LD} = \frac{m\sigma_{x,z}^2}{2\hbar} \qquad (3.6)$$

gives the dispersion due to the diffraction of the initial source size. There are two conditions to be fulfilled in order to maintain the validity of the approach. First, as the name says, the envelope of the wave packets should vary slowly, i.e. $\tau_{ND} \gg \tau_s$ as well as $\tau_{LD} \gg \tau_s$. In cigar shaped BECs this condition is in general only fulfilled if the clouds pass through each other perpendicular to the major axis of the ellipsoid. In order to continue their calculations in analogy to nonlinear optics Trippenbach et al. assume an undepleted pump, i.e. the number of atoms scattered into the outgoing waves is small compared to the number of atoms in the incoming waves. As the densities are so dilute only few scattering events happen when the clouds pass through each other, i.e. this is a reasonable assumption. However, if stimulated processes start to enhance the bosonic fields a significant population of the small perturbational fields can occur. The condition for stimulated scattering is $\tau_s/\sqrt{\tau_{LD}\tau_{ND}} \geq 2$, which is not fulfilled if the SVE assumption is fulfilled. A result of this approach is that, as no quantum mechanical stimulation occurs, the number of scattered atoms on the whole sphere is the same as expected from classical mechanics

$$N_s = \frac{2N^2 a_{00}^2}{\sigma_x \sigma_z} \qquad (3.7)$$

where N is the number of atoms in both incoming waves together, assuming an equal distribution among the two waves as created by the Raman laser pulses.

To capture more of the physics of the four-wave-mixing process of matter waves the mean field energy from the interactions of the surrounding atoms have to be taken into account. Kheruntsyan et al. try to accommodate for this by formulating the differential equations describing the mixing process in the positive-P representation. This way no additional assumptions to the Hamiltonian of eq. (3.2) have to be applied in order to solve the master equations. From numerical simulations it can then be shown, e.g. that even though the atoms "roll" down the energy hill of the mean field interaction upon separation from the condensate the radius of the scattering halo is reduced by about 4% [132]. The reduction of the radius, even though the mean field energy should increase the radius, is due to an increase in entropy. To place the atoms from the indistinguishable ensemble of atoms in the BEC into a mode of distinguishable atoms after scattering reduces the order and hence increases the entropy. Even though the positive-P method yields interesting results, it has its limitation as well. The numerical simulations rely on boundary conditions. The conditions, though diverge as the simulation time continues. Therefore, only collision times can be modeled that are even shorter than typical experimental conditions suggest [136].

The first experiment on four-wave-mixing of matter waves was performed in the group of William Philips [137] whereas the benchmark experiment to characterize the single atom correlations in the FWM process was realized in an experiment using metastable helium and a delay-line detector in the group of Alain Aspect [51]. They scattered on average about 250 atoms out of a condensate of 10^5 atoms and looked at the probability of detecting an atom at position $\vec{r}$ if another atom is detected at position $\vec{r}'$. This two particle correlation function is given by the $g^{(2)}(\vec{r}, \vec{r}')$-function (compare eq. (4.28)). They show that, as predicted by momentum conservation, there is an increased probability in the back-to-back correlations, i.e. the $g^{(2)}(\vec{r}, -\vec{r})$-value of detecting an atom at a position opposite to the position of the first atom mirrored through the center of mass rises above 1. This indicates the momentum conservation of the scattering process. As this process happens in a superposition of all possible angels of the halo, the atoms before detection were in a supposedly entangled state of their momenta.

They also measured the colinear correlations. An increased $g^{(2)}$-function in this case is a manifestation of the Hanbury-Brown-Twiss experiment [37]. Opposite to the $g^{(2)}$-function of a BEC, which is a coherent matter wave and thus is one for all moments of g [39–42], the scattering results in Fock states of single atoms that produce Hanbury-Brown-Twiss correlations. In another experiment the Canberra group used a strong rf outcoupling pulse to initiate a scattering process between m_{+1} and m_0 states. In the scattering process the high densities built up density gratings in the BEC, which in return form phase matching conditions for the scattering atoms[5]. With this self-amplifying process they entered the regime of stimulated scattering. The stimulation leads to a coherent state in the phase matched modes and hence they did not observe the Hanbury-Brown-Twiss effect in this situation [54].

The back-to-back correlations measured by the Palaiseau group suggest the existence of entanglement of two atoms scattered in the FWM process. In a later analysis of the data Kheruntsyan et al. showed that the back-to-back correlations increased significantly above the collinear correlations, such that they could violate a Cauchy-Schwarz inequality, a violation essential for quantum mechanical correlations. Hence, these atom correlation experiments show the prospects of how entanglement in the external degree of freedom of matter waves can be generated in such a system of four waves mixing. In the following subsections it will be described how such schemes will be implemented in the current system.

3.1.3 The optical setup

While all laser cooling to achieve a BEC is done by a laser locked to the 2^3P_2-transition, the Raman transitions will make use of the 2^3P_0-transition. This has the advantage that due to only one magnetic sub level in the excited state the transfer naturally stops at the m_0 magnetic sublevel and no population of the m_{-1} sublevel occurs. The seed laser is a diode laser (DL100L, Toptica) delivering nominally $100\,\mathrm{mW}$. Of typical $80\,\mathrm{mW}$ output $2\,\mathrm{mW}$ are used to lock the laser with a lock-in scheme to the transition. Currently, the current of the diode is modulated in order to modulate the frequency of the laser and the bandwidth limits the modulation to

---

[5]This self enforcing scattering process is similar to the superradiant scattering of light from a cold cloud of atoms.
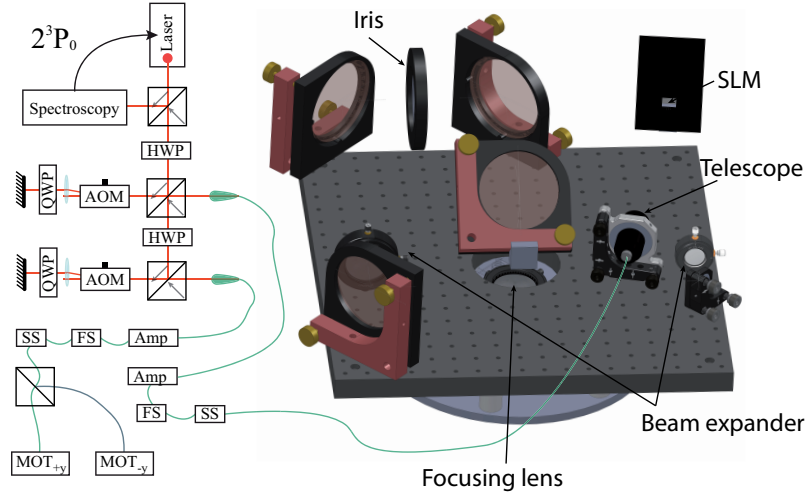
Figure 3.2: The laser preparation of the Raman beams. Two AOMs shift the laser
frequency of L1/L1′ and L2, respectively. Two 2W fiber amplifiers are
seeded by the two laser frequencies and deliver the necessary power
through fast fiber switches (FS) and high attenuation switches (SS) to
the respective stages. L2 needs to illuminate small regions of the BEC
for the devised experiment (see chapter 4) and hence large NA-optics
are used. By modulating spatially the phase of the laser beam, an SLM
generates flexible patterns at the position of the BEC in the focal plane
of the focusing lens.

a few MHz. However, this will be eventually substituted by a PDH scheme involving
an EOM and will be similar to the one for the cooling laser to avoid a modulation
on the laser itself. Fig. 3.2 shows the scheme for the laser preparation of the Raman
lasers.

The remaining laser power is sent through two AOMs to shift the frequency by
$\delta_{Raman} \approx 2 \times 350$MHz with small relative detuning $\delta_{rel} \approx 4.8$ MHz to match the
resonance condition for the two photon process. The resonance is determined by the
trap bottom which splits the magnetic sublevels, which are coupled by the Raman
transition. One AOM prepares the frequency for the lasers L1 and L1′ at δ_{Raman} and
the second one for L2 at $\delta_{Raman} + \delta_{rel}$. Each laser beam of about 2 mW is then fed
into a fiber amplifier (KPS-CUS-BT-YFA-33-SLM-PM-111-FA-FA, Keopsys). Each
of the laser beams will then first pass a fast fiber switch (NanoSpeed 1x2, Agiltron)
to generate the sub-μs light pulses and a slow fiber switch (LightBend 1x2, Agiltron)
which on the other hand has a high attenuation in the off-state to block all light.

After the high attenuation switch L1 and L1′ are split into two fibers by a variable
in-fiber beam splitter (905P, Evanescent Optics) and coupled via the fiber switches
to the respective MOT laser fibers which go to the MOT-telescopes on the y-axis.
As the amplifiers only accept one polarization, but L1 and L1′ have to have orthog-
onal polarizations in order to drive the same transition when coming from opposite
directions, L1 has one fiber whose connector is aligned with the slow axis of the PM
fiber and the other one with the fast axis.

The laser beam L2, which will be injected from the top, determines the regions

within the BEC where the Raman transitions happen, i.e. where the collisions of atoms will predominantly take place. Fig. 3.2 shows the optics for this laser beam. In order to achieve highest resolution of what atoms to address with L2, high NA-optics are used. A 2" achromat lens focuses the laser onto the BEC 400 mm below the lens. The focal length of this is $f = 400\,\text{mm}$ giving a theoretical Gaussian beam waist of $w_0 = 5.5\,\mu\text{m}$. A beam expander consisting of two achromats expands the beam by a factor of 400/75 (one 1" and one 2" lens with focal length $f = 75\,\text{mm}$ and $f = 400\,\text{mm}$).

To be flexible in the pattern generated in the focal plane a spatial light modulator is placed before the beam expands. The SLM operates by reflecting the light and the details will be described in the following subsection. In principle the SLM can change the spot size at the BEC, too. However, to maintain a good diffraction efficiency of the SLM an iris is placed in the confocal point of the second achromat of the beam expander and the focusing lens. The plane where the iris is placed, perpendicular to the optical axis and at the confocal point, is the Fourier plane of the focusing lens and the BEC. Thus, the contributing momentum components can conveniently be manipulated by opening and closing the iris, which will change the spatial intensity distribution of light at the position of the BEC on the scale of the diffraction limit.

3.1.4 Principle of a spatial light modulator

The devised experiment described in chapter 4 requires the light field of the π-polarized beam to be shaped as precisely as possible. In particular, not only the shape of one single spot needs to be modified but it is desirable to even split the beam into multiple spots, all aligned close to each other. In principle, this can be done by shaping different beams and injecting all of them into the vacuum chamber individually. However, this task can be more conveniently and precisely accomplished by a spatial light modulator (SLM). Spatial light modulators are liquid crystal displays, that are able to manipulate certain parts of the beam individually with their pixels of the display. In phase-only modulators the pixels act as phase retarders. A voltage applied to the liquid crystals changes the optical path length for the light. These are typically birefringent and can even rotate the polarization, which in combination with polarizers can then act as amplitude modulators.

The SLM (X10468-08 LCOS-SLM, Hamamatsu) used in the optical setup for the Raman transitions operates by reflecting the light at the back of the liquid crystal and thus is placed as a mirror in the setup. The pixel size is $20\,\mu\text{m}$ and has a filling factor of 95%. The diffraction efficiency, i.e. the amount of light that experiences the desired phase shift, is 80% but depends on the angle at which light is incident on the SLM. A reasonable efficiency can still be used for an incident angle of 7°, enough to seperate the incident beam and reflected beam at a distance of 10 cm from the SLM. The reflection efficiency is about 90%.

The SLM acts as display and is controlled by the graphics card of a computer just if it was one. Displaying on this "screen" different gray values will correspond to different phase shifts at the respective pixel. The phase modulation of the light at the SLM eventually results in amplitude modulation in the far field. Hence, by applying a proper phase modulation one can generate a specific intensity distribution in the focal plane of a lens, which acts as a Fourier transform for light. In general
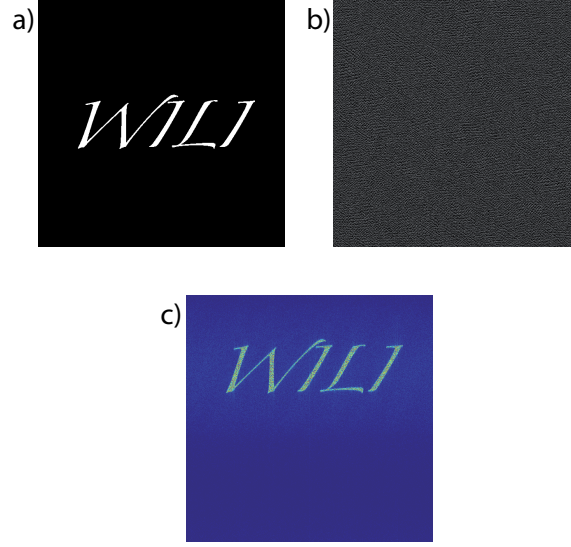
Figure 3.3: The Gerchberg-Saxton algorithm can be used to generate an arbitrary intensity distribution in the imaging plane of a focusing lens. The algorithm starts with a desired intensity a) and shuffles the phases of the two conjugated planes of SLM plane b) and imaging plane back and forth until the necessary phase at the SLM is obtained. Projecting the phase as image to the SLM-"screen" yields the desired image in the far field which is projected onto a camera by a focusing lens c), which can also be moved by a sawtooth grating on top of the main phase.

it is hard to compute the necessary phase modulation to achieve a certain intensity distribution in the focal plane. However, an iterative algorithm like the Gerchberg-Saxton [138] can achieve reasonable results. Fig. 3.3 shows the intensity distribution in the focal plane of the imaging lens created by spatially modulating the phase of a Gaussian beam, overfilling the SLM. The algorithm starts with a random phase distribution at the SLM and uniform intensity (therefore the overfilling the SLM with the Gaussian beam). In each iteration it computes the Fourier transform in the image plane, substitutes the obtained amplitude with the desired amplitude, then computes back the Fourier transform of this at the SLM, and substitutes the obtained amplitude again by a uniform one. Hence, the algorithm always neglects the amplitude after Fourier transform and is only interested in the phase distribution. This converges within less than 10 iterations to fairly satisfying results.

For the purposes of the SLM in this setup, where diffraction limited spots are desirable, the situation is different. The Gerchberg-Saxton algorithm in principle generates an image out of a multitude of diffraction limited spots. Hence, at the scales of the diffraction limit the accuracy of the algorithm breaks down. Instead, multiple spots are generated by step functions and a gradient deflects the light to the desired positions. To increase the spot size the NA of the optics can be reduced by the iris (compare fig 3.2).As the phase is periodic all desired patterns can be summed up and taken modulo 2π to obtain the desired gray scale image, which is to be displayed at the screen.

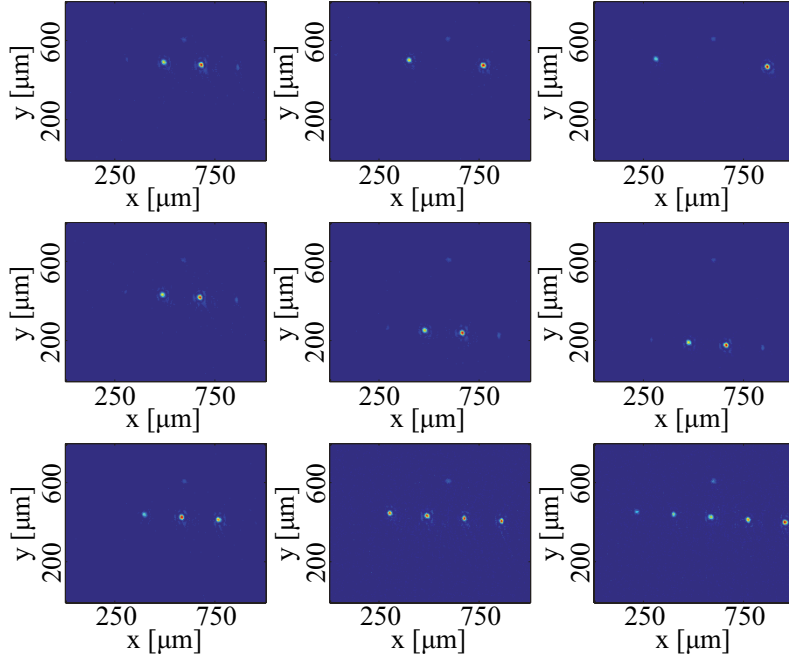Fig. 3.4 shows that with the high NA-optics spot sizes of $8.5\,\mu\text{m}$ can be achieved

Figure 3.4: Images of diffraction limited spots created by the SLM. The minimal obtainable spots size in the setup is 8.5 μm. Shown are varying distances of the spots (top row), varying positions (middle row), and varying numbers of spots (bottom row). The efficiency does not vary when the number of spots is changed or the spots are moved, making the SLM a convenient tool to generate the necessary pattern at the BEC.

in 400 mm distance from the lens, which is just sufficient to have the BEC in the focal plane. The efficiency of the diffraction is the 90% and does not vary much when multiple spots are generated or if they are moved over a distance of 300 μm and more. Again, crucial for high diffraction efficiencies is the alignment of the polarization. The reflection efficiency of the SLM is measured to be 70%. Hence, through the whole optical setup a transmission of 60% is possible.

This shows the ability to generate multiple light spots with beam waist of $w_0 = 8.5$ μm. The spot shape can be altered by an iris or alternative filters in the confocal plane of the focusing lens and the second beam expander. The spots can be conveniently moved and properly aligned with respect to the BEC as well as their own orientation. Only when the distance between adjacent spots is about the size of spots they start to influence each other.

3.2 The four-quadrant delay-line detector

In chapter 4 it will be shown how the ability of the SLM to precisely address small regions in the BEC with the Raman lasers can be used to generate EPR-like entangled states of two metastable helium atoms. In order to verify the entanglement the two atoms need to be detected and identified. Therefore, a single atom detection scheme is essential to prove the entanglement. The high internal energy of the

metastable atoms can be used for this purpose in combination with a micro-channel plate (MCP). A delay line underneath the MCP can then be used to extract the electronic signal and infer spatial and temporal information of the event. The principle and characteristics of this delay-line detector (DLD) is described in this section and will be essential part of the analysis of the feasibility of the experiment of chapter 4.

3.2.1 Principle of a delay-line detector

Micro-channel plates (MCPs) (see fig. 3.5) are widely used in particle physics to detect the high energetic particles with spatial resolutions of a few tens of µm [139, 140] The high internal energy of metastable noble gases can serve as an equivalent to the kinetic energy of high energy physics particles. The MCPs consist of millions of glass tubes with a core varying between a few µm and some ten µm. A high voltage supplied to the surfaces generates a strong electric field within the channels and accelerates all charged particles to the respective side of the MCP. Upon collision of the metastable helium atoms with the walls the energy is released and suffices to overcome the work function to eject electrons out of the channel wall[6]. The channels do not go straight through the glass slab but with a small angle such that accelerated particles do not just pass through the channel, but hit the walls over and over again. Every hit generates secondary electrons, such that a single high energetic particle at the entrance of the channel creates a significant avalanche at the exit (the single event is enhanced by a factor of 10^3-10^4 for single MCP). This avalanche is then strong enough to e.g. illuminate a phosphor screen that can be monitored by a CCD camera. As the avalanche depletes the charge carrier density locally a dead time of up to a few ms occurs. However, other regions of the MCP are not affected by this. In order to increase the gain to a factor of at least 10^7 typically a chevron-stack of two MCPs is used. The "chevron" indicates that the second MCP is oriented such that the angle of its channels is opposite to the one of the channels of the first MCP. This geometry enhances also the uniformity of gain over the whole MCP and additionally prohibits a straight passage of particles through the MCPs.

Monitoring the MCP by the combination of a phosphor screen and CCD allows for recording with high spatial resolution and high flux of particles. However, the read out of the CCD is slow compared to the capabilities of the MCP where the avalanche process takes about 100 ps. A different approach is to place a resistive anode behind the MCP and record the signal electronically. This gives the speed of pure electronics but does not contain accurate position information anymore. The speed of propagation of the electronic signal on the anode is about 30% of the speed of light in vacuum. For an MCP of radius 40 mm this means a signal takes about 100 ps to travel along the anode. This is at the limit of what is electronically recognizable, but makes it unlikely to resolve where the particle hit the anode. However, if the anode is arranged such that the signal needs to travel along it multiple times the resolution can be enhanced. The effective propagation speed in delay-line detectors is thus increased, by winding the anode as a transmission line either meander-shaped or as a helix behind the MCP. The avalanche signal is then coupled capacitively as image charge to the delay line and propagates along

---

[6]Some MCPs use coatings for the channels to lower the work function. This increases the efficiency of a detection by the MCP.
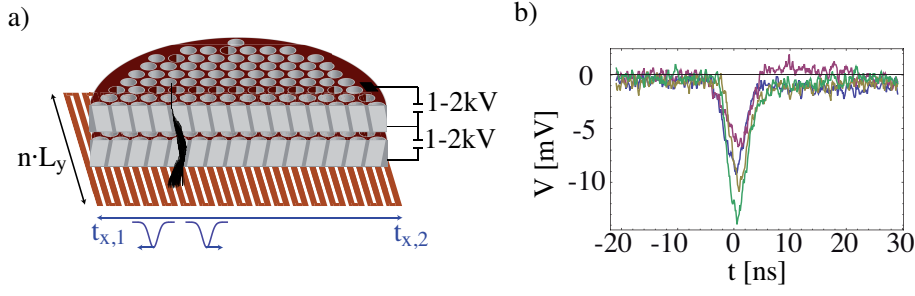
Figure 3.5: a) A schematic of an MCP. Glass tubes form μm-sized channels in which charged particles are accelerated to produce electronic avalanches. The avalanches can either be detected optically when they excite a phosphor screen or electronically in combination with a delay line. Using a delay line the signal takes $n \cdot L_y$ to propagate in x-direction. b) The delay line in the specific detector is split into four quadrants. For each quadrant the peaks heralding a detection event are shown. These are converted by the CFD into a fast rising pulse, whose arrival at the TDC is in turn converted into a digitized time.

the transmission line in both directions. The arrival time of the two signals at both ends of the delay line is recorded. The offset from the sum of the two signals from some time zero of when the recording was started yields the time when the event occurred. From the difference of the two arrival times the position in the dimension perpendicular to the winding of the meander can be inferred. To get a full three dimensional information typically a second meander is placed orthogonal to the first one. However, to properly identify signals a second particle must not hit the anode while the signals are still propagating on the delay line. Hence, a limiting dead time of typically some tens of ns is given by this restriction. To overcome this limitation, a third meander structure can be installed, such that the three delay lines are symmetrically oriented. The third helix is redundant for a single event reconstruction. Nevertheless, for situations of multi-events sophisticated algorithms can obtain the three dimensional information of up to ten events with this redundancy if they do not hit at the same position [141].

The avalanche behind the MCP typically spreads over multiple pick up strips of the delay line (typically a few hundred μm thick). However, upon propagation the wave packets traveling from each strip spread and overlap when they reach the read out electronics. This way a constant fraction discriminator (CFD) can determine the maximum of the signal with higher precision than the pitch distance of the delay line. The CFD transforms this information into a fast rising pulse (see inset of fig. 3.5).The CFD, combined with a preamplifier, is attached to the vacuum chamber as up to this point all contributions along the transmission line need to be considered for the analysis. From there the time signal is sent to a time-to-digital-converter (TDC) which can convert the time from the fast rising pulse generated by the CFD. The information of all arrival times is then recorded and an algorithm reconstructs which arrival times belong to each other and computes the three dimensional coordinate of the detection event.

3.2.2 The performance of the delay-line detector

There are two main figures of merit of the delay-line detector important to this system. The efficiency to detect single particles η and the resolution[7] in spatial as well as in temporal dimension $\delta_{x,y,t}$. This subsection describes the specific DLD of the system in terms of its characteristics as well as the geometry within the setup to reconstruct the three dimensional momentum of an atom after time of flight.

In the current system a four-quadrant delay-line detector (DLD 3030-4Q, Surface Concept) is installed. Even though the chevron stack of MCPs consists of one large circular disk with 40 mm radius, the delay line underneath the MCP splits into four individual delay lines with independent read out electronics. Fig. 3.6 shows a two dimensional image of a cloud passing through the MCP and being registered by the four quadrants. The detector is mounted straight underneath the magnetic trap of the helium atoms so that they hit the detector upon release from the trap and after free fall. Fine adjustment can be done by an xy-translation stage and a rotation stage (SLC-2460-S-UHV+ SR-3610-S-UHV, Smaract). The travel range of the linear stages is 17 mm with a resolution of 5 nm and the rotation stage can be rotated by 90° (limited by cables) in steps of 0.3 μrad. A hole in the optical table carrying the vacuum system allows for a distance from the magnetic trap to the detector of $H = 800$ mm. Just before the detector, there is a full metal gate valve (48244-CE74-AKS1, VAT) to close the detector off when the titanium sublimation pump in the main chamber is switched on. The detector side of the vacuum can separately be pumped by an extra turbo pump (HiPace300, Pfeiffer Vakuum).

Detection efficiency

To test the efficiency of the DLD a cloud of thermal helium atoms is cooled to 35 μK by evaporative cooling. A second 5 ms short rf pulse outcouples a fraction of the remaining atoms. From absorption imaging, the number of atoms still in the trap after the rf spilling pulse is known and the outcoupled atoms are recorded with the DLD. The total number of atoms is deduced from runs where no atoms are outcoupled of the trap. As the thermal cloud is too hot to fall entirely on the DLD, not all atoms missing in the remaining cloud in the trap can be detected by the DLD. More so the rf couples out from an isoenergetic shell of the cloud corresponding to the rf frequency. This results in a shell of atoms passing through the DLD with a radius larger than the radius of the active area of the MCP. The width and radius of this shell can be obtained by fitting two Gaussian distributions to the time histogram of the detection events on the DLD (compare fig. 3.7). From this fit the number of atoms that could have been detected can be corrected. The ratio to the total number of atoms then yields the efficiency of the DLD. If the voltage at the two MCPs is too low, quadrants one, two, and three show reduced count rates even when quadrant four still records reasonable count rates. This is due to a reduced pulse height (see inset of fig. 3.5) before the CFD and needs readjustment of the threshold of the CFD for the respective quadrants. However, when the voltages are high enough (1.35 kV at each of the MCPs) all four quadrants show similar count rates. Other groups have

---

[7]In the context of detecting the position of a single particle the term "resolution" is used to describe the error in determining the position and given by the standard deviation of a statistical ensemble.
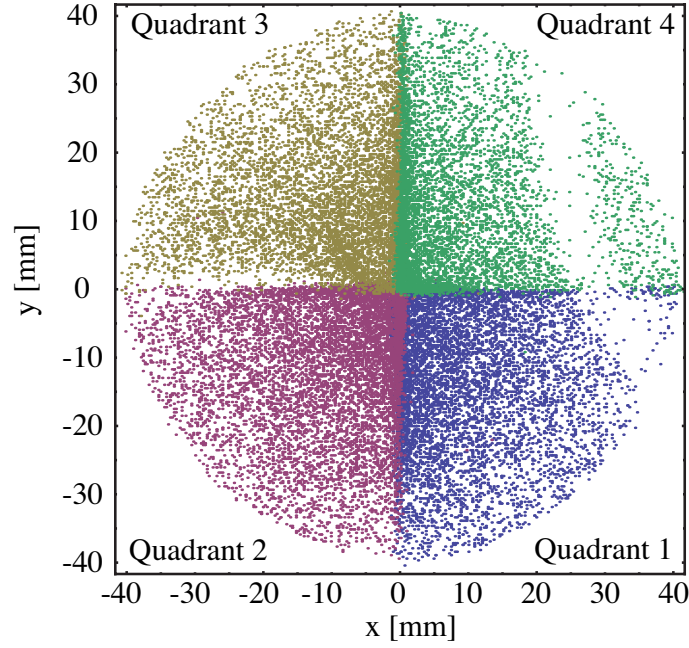
Figure 3.6: Behind the MCP are four independent delay lines splitting the detector
into four quadrants. This way single atoms can be detected simultane-
ously on different quadrants, overcoming the individual dead time of
each quadrant.

reported non-uniformities over the MCP, which are not observed with the 4Q-DLD
in this system. Hence, the efficiency is assumed to be constant over the MCP and
all four quadrants. The main systematic error results from the uncertainty of the
number of atoms determined by the imaging system. Correcting, for the temperature
dependent velocity distribution of the cloud the error in the number of atoms can
be assumed to be less than 20%. This is on less than the statistical error over 200
runs and yields an efficiency of $\eta = 0.07 \pm 0.02$, which is comparable to what other
groups have reported for metastable helium.

Temporal resolution

To test the temporal resolution of the DLD a mode locked picosecond laser (pico-
TRAINTM IC-355-3000 ps, HighQ Laser) at 355 nm was set up. The intense near UV
photon pulses can eject electrons by multi-photon absorption processes. The mode
locked pulses give an inherent trigger to the detector (repetition rate 80 MHz). Inte-
grating over 1 s each quadrant is addressed by the laser individually while a second
beam hits another quadrant. This way the relative error between quadrants can be
determined as well. The arrival times of the photons are then taken modulo the
repetition rate of the mode locked laser and the distribution yields an upper bound
to the electronic time resolution of the quadrants. Fig. 3.8 shows the distributions
for each quadrant. A width of $\delta_t = 250 \pm 50$ ps[8] averaged over all four quadrants
is measured. With the velocity of the atoms at the detector this can be converted

---

[8]This gives an upper bound as the pulse width of the mode-locked laser is not taken into account.
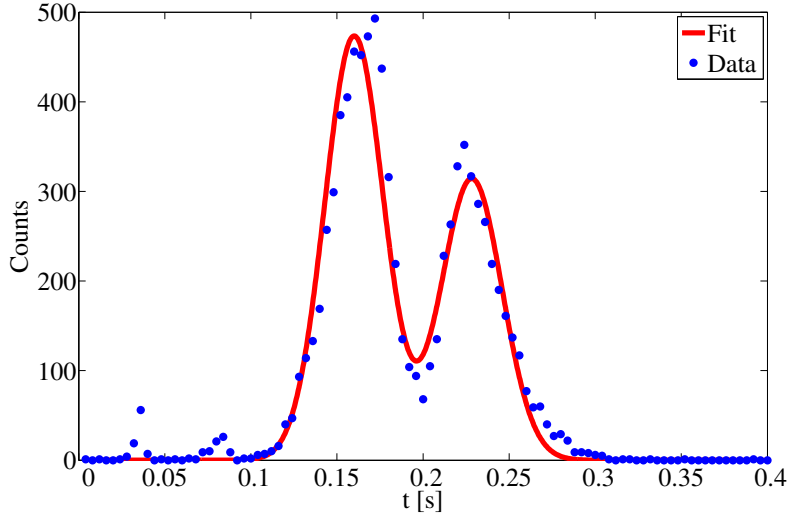
Figure 3.7: A shell of atoms with radius larger than the radius of the active area of the MCP is passing through the DLD. From the time histogram of the detection events the radius and width can be deduced to correct for the atoms that miss the detector.

into a spatial resolution in z-direction of $\delta_z = 1.0 \pm 0.2\,\text{nm}$. However, it should be mentioned that the validity of this conversion is not bullet-proof. The characterization of the temporal resolution is done by photons which travel at the speed of light. Hence, any finite penetration depth into the channel before the electrons are ejected is negligible. The metastable atoms, though have a velocity of $4\,\text{m/s}$ when they hit the detector. The angle of the channels allows the atoms in principle to penetrate about $d_p = 100\,\mu\text{m}$ into the channel before they have to hit the wall. Hence, the event can happen within a jitter of about $25\,\mu\text{s}$, much larger than the measured sub-ns temporal resolution. If the atoms can penetrate into the channel that means the spatial resolution in z-axis is given by the penetration depth d_p into the MCP. This would be on the same order of magnitude as the spatial resolution in x and y. The experiments on atom statistics performed by the Groups in Palaiseau [38, 45, 51] and Canberra [44] on the other hand confirm, that the temporal resolution is better than the spatial resolution and the electronic time resolution can in good approximation indeed be converted with the velocity of the atoms at the detector.

From the minimal distance of two detection events the dead time t_d of the individual quadrants can be deduced. All Quadrants show an onset of counts at about $t_d = 25\,\text{ns}$. Tab. 3.1 shows the results for the temporal resolution as well as the timing jitters δt_j between different quadrants which is calculated from the distribution of events of the same mode locked laser at the two different quadrants with respect to the first quadrant. The minimal distance between detection events on separate quadrants goes to zero as the read out electronics are independent and an event on one quadrant can be identified even though events at other quadrants can occur.
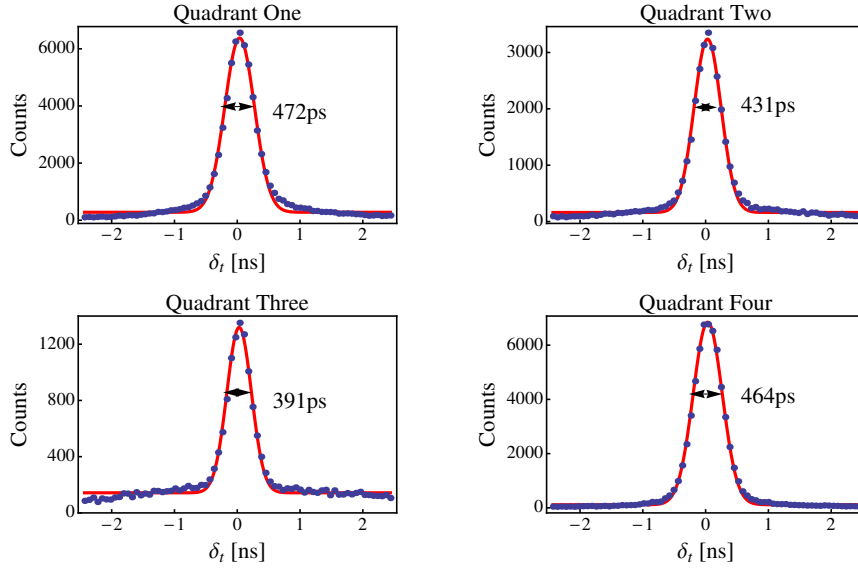
Figure 3.8: A mode locked ps-laser is used to characterize the temporal resolution of the DLD. The events occur at precise intervals given by the oscillator length of the laser. A histogram of the detection events modulo this interval yields the temporal resolution.

Quadrant	δt [ps]	δt_j [ps]
Q1	236 ± 12	0
Q2	215 ± 9	10
Q3	196 ± 16	40
Q4	232 ± 12	136

Table 3.1: A summary of the timing characteristics of the DLD. The error of the temporal resolution δt is a statistical over several runs. The jitter δt_j between individual quadrants is small compared to the resolution.

Spatial resolution

The time binning of the TDC is $6.859\,\mathrm{ps}$ while the binning of the spatial dimension happens at the TDC in $27\,\mathrm{ps}$ bins. The latter binning defines the pixel in the spatial dimension as well. From the size of the MCP and the number of pixels per diameter a spatial pixel size can be calculated to be $p_x = 32\,\mu\mathrm{m}$ and $p_y = 36\,\mu\mathrm{m}$. Note, the pixel size does not relate to the spatial resolution attainable by the DLD as it does for CCD cameras even though the terminology is similar. A simple approach to estimate the resolution can be done by subtracting the two time sums of the two dimensions. The time sum of each dimension should be the arrival time of the detection event plus some constant time the signal takes to propagate along the whole transmission line. Subtracting the two time sums of the two dimensions will eliminate the offset caused by the arrival time. As the time to travel the transmission line remains constant for every event the distribution of this time sum method results in a sharp peak if the resolutions of the DLD were perfect. Fig. 3.9 shows

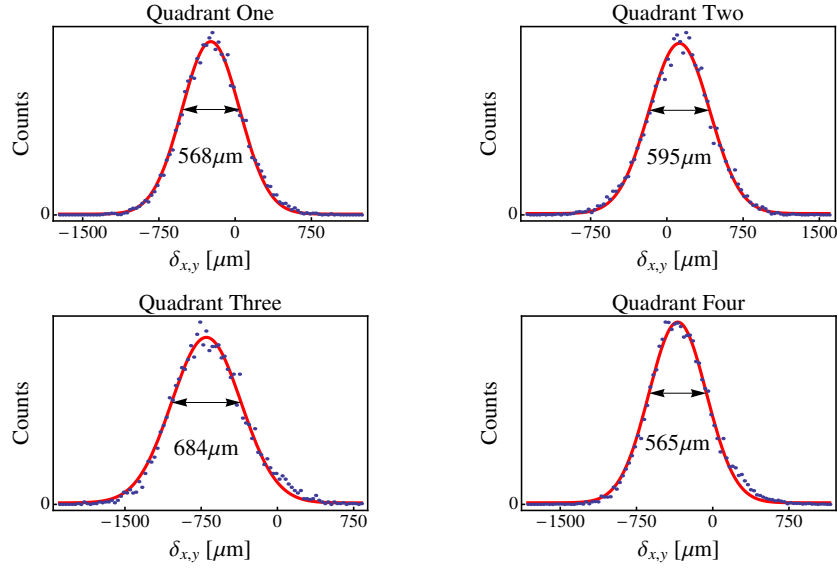Figure 3.9: The time sum of the recorded events can be subtracted for the two dimensions to have a first check on the spatial resolution of the detector. The histograms show the distribution of recorded events for all four quadrants. With the pixel size of about 30 μm this gives roughly 300 μm spatial resolution.

the histograms of the time sum distribution for all four quadrants. Together with the pixel size a spatial resolution of $\delta_{x,y} \approx 300\,\mu$m is obtained. However, the chips in the CFD produce similar systematic errors, which add up in the time sum but cancel out when the two individual signals of one dimension are subtracted from each other to determine the respective coordinate. Hence, there is a compromise between optimizing the temporal resolution (time sum) and spatial resolution (time difference). In particular, the spatial resolution is likely to be better than what is estimated from the time sum method.

A more accurate way to determine the spatial resolutions of the detector is to project a known pattern on to the detector. The drawback is that the vacuum system has to be opened to insert a mask to avoid any image blurring from a distant mask. In a first experiment a shadow mask with 30 μm holes in diameter and 500 μm pitch is placed 2 mm before the MCP. The diffraction at the holes is only 0.001rad. However, the mask itself is only 300 μm thick and thus, atoms with an angle of 0.1rad can pass through. Hence, the spot size at the detector is 90 μm. The mask is then illuminated by a cloud of thermal helium atoms released from the MOT with a short molasses pulse applied (see chapter 2.8.4). The small filling factor of the mask results in a little bit more than 10k events over the whole detector area. Hence, to obtain somewhat reasonable statistics 20k runs were performed. The diameter of the holes of the shadow mask was sampled with an electron microscope (Supra-55, Zeiss) Even though the error of the the diameter was measured to be only ±5 μm certain areas of the mask allowed for better transmission and held better statistics. These areas were analyzed by fitting 24 Gaussian distributions to a subarea of the detector. Fig. 3.10 shows the image of the shadow mask. In the fig. 3.10b the structure of the
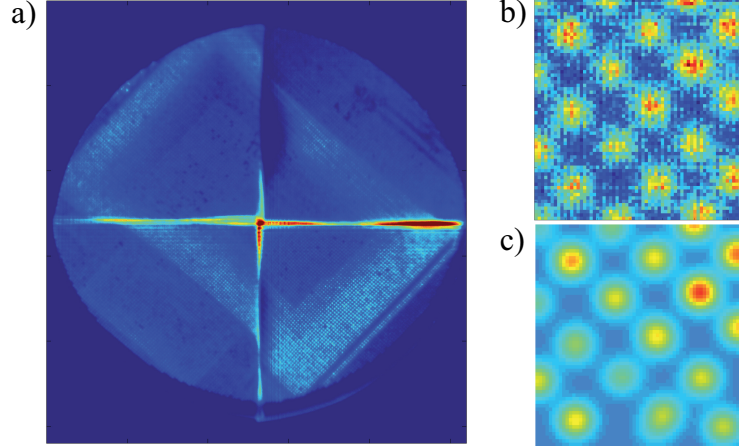
Figure 3.10: a) An image of a shadow mask placed $2\,\mathrm{mm}$ above the MCP. The shadow mask has about $80\,\mathrm{k}$ holes with $30\,\mu\mathrm{m}$ diameter and $500\,\mu\mathrm{m}$ pitch. An accumulation of $20\,\mathrm{k}$ clouds of thermal atoms from the MOT is used to extract the spatial resolution of the detector. b) shows a subsection of an area with high count rates and c) shows the fit of 24 two-dimensional Gaussian distributions to it, yielding the spatial resolution. Note how spots at the edges of the image can disturb the fitting procedure, still holding reasonable fits, while overestimating the resolution.

mask is more clearly visible and the fit to such a subsection of the image is shown in fig. 3.10.

With this the spatial resolution can be calculated. Table 3.2 shows the results for all four quadrants. The resolutions for quadrants one, two, and three where hard to extract and indicate that those three quadrants require a new adjustment of CFD and TDC. However, the result of quadrant four shows that resolutions of $\delta_x = 153 \pm 10\,\mu\mathrm{m}$ are possible. Deconvoluted with the spot size of the image at the detector this corresponds to $\delta'_x = 124\,\mu\mathrm{m} \pm 12$ and will be used for the analysis of chapter 4.

As the resolution of the detector is the bottle neck of all experiments looking for the correlations in time of flight measurements any effort to improve on the resolution is worthwhile. There are three technical improvements that can be implemented relatively easily[9]. Quadrants one through three showed issues with the pulse height of the CFD. This can be improved by improved amplification stages before the CFD. Secondly, the parameters for the quadrants need to be readjusted and can be optimized for spatial resolution. This can provide a spatial resolution improvement of about 50% at the cost of temporal resolution. However, the temporal resolution is by far better than the spatial ones and would not limit the experiment if reduced to some extent. Finally, but most promising is to upgrade the CFD with a module that

---

[9]This paragraph is an excerpt from personal discussions with Andeas Ölsner of Surface Concept.

Quadrant	δ_x [μm]	δ'_x [μm]	δ_y [μm]	δ'_y [μm]
Q1	175.0 ± 5.8	150.1 ± 6.8	215.1 ± 6.8	195.4 ± 7.4
Q2	196.4 ± 8.7	174.5 ± 9.8	241 ± 12	224 ± 13
Q3	204 ± 15	184 ± 17	226 ± 10	207 ± 11
Q4	153 ± 10	124 ± 12	185 ± 12	161 ± 13

Table 3.2: The spatial resolution $\delta_{x,y}$ of the individual quadrants of the DLD, as well as the resolution $\delta'_{x,y}$ deconvoluted with the mask structure. The errors stem from statistical variations between different sub pictures. The large error for quadrant four suffers from areas where low count rates, i.e. no good fits, were obtained. As these areas probably only suffered from low count rates the resolution given here is on the conservative side. The degraded resolution of quadrants one through three compared to quadrant four indicate again the necessity for a readjustment of the other three quadrants.

reflects the incoming signal a few times back on the CFD. Hence, the signal can be measured multiple times reducing the error at the cost of a larger dead time of about 150 ns. Fig.3.11 shows a measurement of Surface Concept where they could improve the electronic accuracy by a factor 2-3. This would bring the spatial resolution down to about 60 μm.

Dark counts

A big advantage of a DLD for detection of single atoms is its low dark counts. Due to the requirement of relatively high energies in order to eject electrons out of the walls of the MCP, barely any spurious counts not originating from atoms are registered. To characterize the detector with respect to its dark counts within the system, the valve to the main chamber is left open, but no helium atoms are present in the main chamber. In this scenario a dark count rate of $60\,\text{s}^{-1}$ is measured over the whole detector. As seen in fig. 3.10 atoms hitting the MCP at the edge between two quadrants can be registered by either quadrant and therefore leads to an artificial higher count rate for the dark counts as well. As this area is restricted to $\pm 300\,\text{μm}$ where the intersection of two quadrants is, this can safely avoided by orienting the DLD appropriately for experiments. Table 3.3 shows the total dark counts of the individual quadrants as well as the dark counts excluding the regions of the edge.

3.2.3 Reconstructing momentum space

When the atoms are transferred to the magnetic insensitive state during the Raman transition, they are no longer trapped by the magnetic trap. Gravity accelerates them towards the detector underneath the trap. From the time of flight the momentum distribution in three spherical coordinates can be reconstructed. Fig. 3.12 shows a
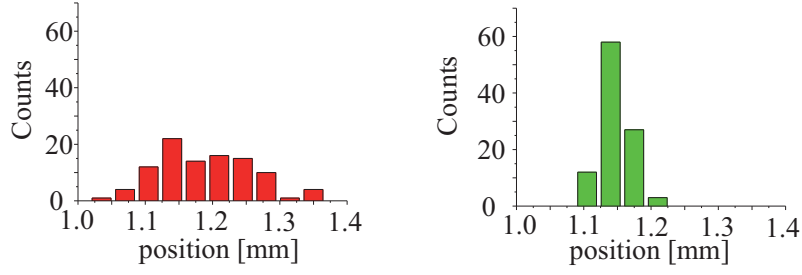
Figure 3.11: Histograms of arrival times of electronic signals. Shown is a test of the electronics performed by Surface Concept. The timing error has been converted to the corresponding spatial resolution of the DLD in the system. A module before the CFD (right) could reflect the signal N times to let the CFD measure it N times. Hence, the error would drop by a factor of $\sqrt{N}$, which would improve the spatial resolution by a factor of 2-3 in this case where 8 reflections were introduced.

Quadrant	Dark Counts Total [s^{-1}]	Dark Counts without Edge effect [s^{-1}]
Q1	28.2 ± 5.7	5.2 ± 1.0
Q2	13.6 ± 3.8	5.9 ± 1.6
Q3	49.5 ± 7.8	7.1 ± 1.1
Q4	18.3 ± 5.0	4.0 ± 1.1

Table 3.3: The dark counts of the individual quadrants of the DLD with and without the edges of the quadrants. The error is given from the statistics of 600 runs with each 1 s exposure.

BEC dropped onto the DLD and its momentum distribution calculated with

$$\theta(x,y,t) = \arccos\left(\frac{gt^2 - 2H - v_z}{\sqrt{\left(gt^2 - 2H - v_z\right)^2 + 4\left(x^2 + y^2\right)}}\right) \tag{3.8}$$

$$\phi(x,y,t) = \pi(1 - \mathrm{sgn}(y)) + \mathrm{sgn}(y)\arccos\left(\frac{x}{\sqrt{x^2 + y^2}}\right) \tag{3.9}$$

$$p(x,y,t) = \frac{m}{2t}\sqrt{\left(gt^2 - 2H - v_z\right)^2 + 4\left(x^2 + y^2\right)} \tag{3.10}$$

$$\tag{3.11}$$

The equations include already a possible initial velocity v_z component along the z-direction. This is required for properly reconstructing the momentum shell of the scattered atoms after the Raman transition, where the atoms receive a momentum kick upwards $v_z = \sqrt{2}\hbar k/m$ by the stimulated emission of a photon into L2. However, if a cloud is simply released from the trap, this component is taken to be zero. The
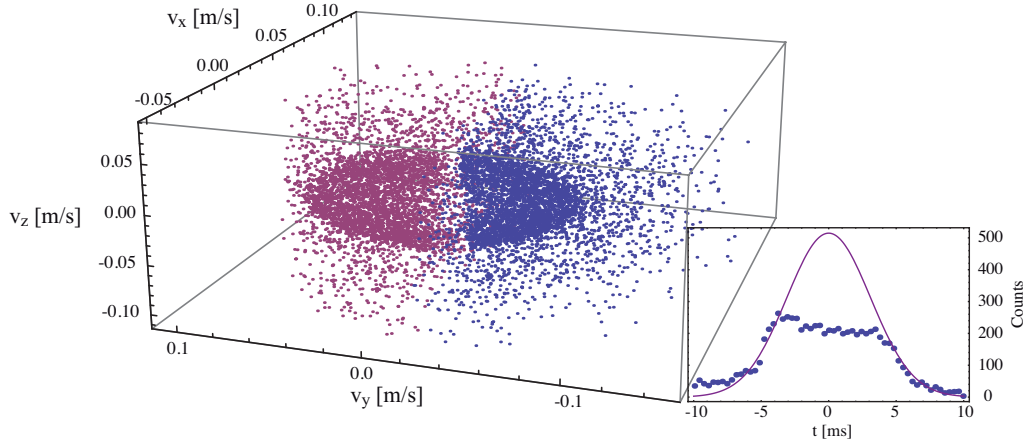
Figure 3.12: An image of a BEC passing through the DLD. With the distance of the trap to the detector known the momenta of the atoms can be reconstructed and the pancake shape of the BEC after time of flight becomes visible. The inset shows a time histogram of the cloud. At the center of the cloud the density becomes too high for the detector to record all events.

inset of fig. 3.12 shows the time histogram for the cloud exhibiting a flat hat top of the distribution where the detector is saturated by the dense cloud of atoms. From this the maximal flux is determined to be $\sim 5 \cdot 10^5\,\mathrm{s}^{-1}$ per quadrant. This is valid in the regime of a BEC where high densities for a (in terms of particle physics) long burst time occur. However, the atoms scattered in the four-wave-mixing process are much more dilute and will not be limited by the bandwidth of the detector.

This concludes this chapter, where the four-wave mixing-process was introduced and the ability to realize flexible light patterns at the BEC with a resolution close to the diffraction limit. The DLD was shown to have comparable detection efficiencies as reported by other groups and the resolution of the detector was characterized. The spatial resolution of $120\,\mu\mathrm{m}$ will be the bottle neck for experiments looking at atom correlations. However, possible ways for improvements are pointed out, such as multiple measurements of the electronic signal to reduce the measurement error.

4 The devised experiment to demonstrate momentum entanglement

In the preceding chapters the experimental basis to precisely create matter waves and accurately measure them was presented. In this chapter the experiment is discussed for which the system is designed. The ensemble of ultra-cold atoms in the BEC serves as a source for coherent matter waves. The precise control of the Raman beams using the spatial light modulator will be used to prepare an Einstein-Podolsky-Rosen-like state of two counter-propagating atoms. The delay-line detector finally, with its high spatial and temporal resolution able to detect single atoms, will be used to analyze the correlations of the atoms. For interpreting the data the first section of this chapter lays the foundation of an understanding of entanglement in terms of a historical review. Afterwards two conceptual experiments are described, capable of showing entanglement in momentum space. While the double-double diamond scheme of section 4.2 is able to perform a full Bell type experiment, section 4.3 will simplify the setup at the cost of not being able to rule out local hidden variables. Nevertheless, within quantum mechanics entanglement can be shown with this arrangement and tested against classical predictions. A deviation of this scheme provides access to test local hidden variables again and will be used to discuss the theory behind the devised experiment in section 4.5 and analyze the capabilities of the metastable helium BEC platform to perform such an experiment.

4.1 Review of entanglement

In this section the idea of entanglement is presented in the context of its historical argument by Einstein, Podolsky, and Rosen (EPR) [11]. Their idea will provide the essential gedankenexperiment underlying the setup to perform an entanglement experiment in the external degree of freedom of a matter wave. This section is concluded by pointing out the difference to the more widely used scheme of spin entanglement.

Not long after the formulation of quantum mechanics by Schrödinger and Heisenberg, EPR drew the attention to entanglement, an intriguing feature of quantum mechanics. In their seminal work of 1935, they argued that quantum mechanics cannot be complete by its own laws. They first took special relativity to claim no action to have an effect faster than light on a distant object. Together with their criterion for "elements of reality", that a prediction about a real physical quantity cannot be subject to probabilities if all elements of this reality can be observed, they laid the foundation to what is today called "local realism". An implication of what Bell later

extended to be local realism is, that a measurement on one particle cannot affect the reality of another, space-like separated particle. EPR then looked at a system of two particles A and B interacting at some point in time, but that are then separated and do not interact with each other anymore. The state in its position representation for the position x_a and x_b of particle A and particle B, respectively can be written as

$$\Psi(x_a, x_b) = \int_{-\infty}^{\infty} e^{(2\pi i/h)(x_a - x_b + x_0)p} dp \tag{4.1}$$

with some constant offset x_0 in position. The integrand is the eigenfunction for the single-particle momentum operator $\hat{p}_i$ with eigenvalues p and $-p$ for particle A and particle B, respectively. On the other hand the state itself, i.e. the Fourier transform of the integrand is the eigenfunction for the position operator $\hat{x}_i$ with eigenvalues x_a and $x_b - x_0$ for particle A and particle B, respectively. The Fourier transform represents the quantum mechanical feature that all bases are equivalent to describe a state, i.e. the observer can choose the basis in which the measurement is conducted. This mathematical rotation of the basis corresponds to a different experimental measurement setting. In the EPR example, the observer can choose whether he wants to measure position or momentum (or anything in between) of the system and still the measurement yields an exact answer in the respective Fourier space.

When one observation is now made in position space the state is projected onto the state corresponding to the measurement, i.e. if the position of particle A is measured $\hat{x}_a|\Psi\rangle = x_a$ then particle B has to be in an eigenstate of its position representation as well, yielding with certainty an outcome $\hat{x}_b|\Psi\rangle = x_a + x_0$. On the other hand, the same holds true for momentum space, i.e. if the momentum of particle A is measured $\hat{p}_a|\Psi\rangle = p$ then particle B has to be in an eigenstate of its momentum representation as well, yielding with certainty outcome $-p$ for $\hat{p}_b|\Psi\rangle$. However, the two particles are well separated and the measurements can be performed independently. This is to say, without disturbing particle B, the position of particle A can be measured and the outcome for a position measurement on particle B predicted with certainty. On the other hand, again without disturbing particle B, the momentum of particle A can be measured and the outcome for a momentum measurement on particle B predicted with certainty. As required by the locality of the measurement process and to be an element of reality, particle B has to have both outcomes for position and momentum with certainty no matter what measurement is performed on particle A.

However in quantum mechanics, after Heisenberg's uncertainty principle [12], two conjugate variables of one particle like $\hat{x}$ and $\hat{p}$ cannot be predetermined without any uncertainty the same time. The operators of two conjugate variables of one particle are non-commuting, i.e. the order in which they are applied to the state matters

$$[\hat{x}_i, \hat{p}_j] = \hat{x}_i\hat{p}_j - \hat{p}_j\hat{x}_i = -i\hbar\delta_{ij} \tag{4.2}$$

Note that two "conjugate" variables x_i and p_j with $i \neq j$ of two different particles are not conjugate and do commute. The complimentarity of the two conjugate variables requires the uncertainty of one variable to approach infinity if its conjugate variable is determined with certainty. From this commutation relation Heisenberg derived his uncertainty principle which is one of the most fundamental principles in quantum

mechanics, i.e. the product of the uncertainties of two non-commuting observables cannot vanish

$$\sigma_{x_i}\sigma_{p_i} \geqslant \frac{\hbar}{2} \tag{4.3}$$

Thus, only one observable can be measured arbitrarily precise[1], while the uncertainty of the other one unconditionally approaches infinity. This however, leads to a contradiction of the train of thoughts in the EPR case. Measuring either observable of particle A, predicts the respective observable of particle B equally well, even though there is no action at a distance. As the basis of the measurement on particle A is not a priori determined, both observables of particle B need to be an "element of reality" from the very beginning and should be precisely measurable with unity probability contradicting Heisenberg's principle.

As EPR only used the quantum mechanical properties of uncertainty principle and entanglement to conclude this contradiction, the problem formulated by EPR is usually referred to as EPR paradox. However, EPR proved quantum mechanics to be incompatible with their notion of "elements of reality", as this assumption is necessary to infer the result at the other particle. As a consequence of the Newtonian mechanics this was the prevailing philosophical view of physics[2] at that time and the incompatibility to quantum mechanical predictions justified their reasoning to claim quantum mechanics to be incomplete, i.e. not capturing the full physics behind this effect. To recover the deterministic world view initiated by the mathematical formulation of classical physics by Newton, Einstein expressed the hope that a theory could be formulated that extends quantum mechanics with some additional physical quantity to make it complete. Such quantities were later referred to as "local hidden variables".

As the measurement of the conjugate variable to the one measured at particle A is performed at the remote location where particle B is measured, the uncertainty principle of eq. (4.3) does not describe the full system of two particles. In this situation, though a criterion can be derived that, given the total variance of the system of the dimensionless positions $\langle\Delta(\hat{x}_a - \hat{x}_b)\rangle^2/x_d^2$ and momenta $\langle\Delta(\hat{p}_a + \hat{p}_b)\rangle^2/p_d^2$, is only fulfilled for entangled systems [143]

$$\frac{1}{x_d^2}\langle\Delta(\hat{x}_a - \hat{x}_b)\rangle^2 + \frac{1}{p_d^2}\langle\Delta(\hat{p}_a + \hat{p}_b)\rangle^2 \leq 1 \tag{4.4}$$

The constants x_d and p_d have to be chosen for the appropriate system and fulfill the relation[3]

$$ix_dp_d = [(\hat{x}_a - \hat{x}_b), (\hat{p}_a + \hat{p}_b)] \tag{4.5}$$

For more than 30 years this problem was taken as purely philosophical. Bohm had reformulated the problem of EPR's continuous variables into a system of two discrete

---

[1]This formulation indicates the statistical uncertainty $\sigma_{x_i} = \sqrt{\langle\hat{x}_i^2\rangle - \langle\hat{x}_i\rangle^2}$ to be zero.

[2]Bohr in his early response already pointed out that such view is not consistent with quantum mechanics and should be avoided [142].

[3]If either of the variances of the observables is known the respective proper constant is the variance times $\sqrt{2}$.

two-level particles with spin-1/2 [13]. Even though equivalent the discrete system is easier to deal with as measurement outcomes can only yield $\hat{J}_i|\Psi_{\frac{1}{2}}\rangle = \pm 1/2$. However, observables J_i along either axis i of the Bloch sphere do not commute and yield the same arguments as in the case of the continuous variables $\hat{x}$ and $\hat{p}$. It was Bell to realize that no local hidden variable theory, i.e. a theory employing some local hidden variables (even if only additional to quantum mechanics in order to make it complete), could explain the correlations arising from entanglement [14, 15]. The ideas of Bell were to be proven in a system with perfect correlations and thus challenging to proof by experiments. The most prominent formulation of a Bell inequality applicable to real experiments was brought forward by Clauser, Horne, Shimony, and Holt (CHSH) [144]. Central to both, Bell's and CHSH's proof is the assumption that the measurement on one side does not depend on the measurement on the other side fulfilling the locality criterion, but can depend on some hidden variables. The requirement to reproduce quantum mechanical correlations for measurements in orthogonal bases and the use of a Cauchy-Schwarz inequality [4] to calculate probabilities at different angles lead to an upper bound for theories of local hidden variables. However, quantum mechanical probabilities of the two-level system do not adhere to a linear trend, which is immanent to the Cauchy-Schwarz inequality, but rather show a sinusoidal behavior as result of the projective measurement process on eigenstates. For example, the probability to detect a photon of linear polarization after a polarizer follows Malus' Law[5]. Hence, choosing the right angles to measure the state on the Bloch sphere let quantum mechanical correlations violate a Bell-, or a CHSH-inequality, respectively[6].

With the experiments demonstrating a violation of Bell's inequality [16, 21–25], respectively appropriate versions of it, quantum mechanics was proven impressively to be correct and excelled with its correlation to be stronger than what local hidden variable theories can provide. While a full proof under strict locality conditions with high detection efficiencies remains challenging to perform for current technology, the implications of entanglement for information science is far reaching [145–148]. Quantum cryptography and quantum computing assume quantum mechanics to be true and have started to explore the power of entanglement. In these scenarios it is not a question of completeness of quantum mechanics, but rather whether the state at hand is entangled. The definition of entanglement in quantum mechanics is a more general one than what is required for the EPR-paradox, but can be illustrated with their example. The outcome of the measurement on each particle has to be random in any basis, i.e. the mixed state[7] of the single particle, after the second particle is traced out of the entangled state, has even probabilities for all measurement settings. Hence, a maximally entangled state is an even superposition of orthogonal states.

---

[4]The Cauchy-Schwarz inequality states that the square of the inner product of two vectors is smaller or equal the product of the inner products of the individual vectors and one of its consequences is for example the triangle inequality, which is used in Bell's derivation.

[5]$P(\theta) = 1 - (\cos\theta)^2$

[6]The original angles are calculated for the two level system, i.e. spin-1/2. The polarization of photons is in practice however, a spin-1 particle and thus, its phase changes twice as fast. Hence, the angles at which quantum mechanics violates the inequalities maximally are half as big for photons entangled in their polarization.

[7]Mixed states result from pure states where some information has been irrevocably migrated to the environment and thus is traced out.

On the other hand the two systems should be correlated, i.e. each eigenstate in one system should be uniquely related to an eigenstate of the partner system. As this should hold for any basis, the system of both particles needs to be in a superposition of correlated states. Formally, this means a pure bipartite state is entangled if and only if the state cannot be separated into a simple product of states [149]

$$\Psi_{ent}(x_1, x_2) \neq \Psi_{sep}(x_1, x_2) = \psi(x_1)\phi(x_2) \tag{4.6}$$

As current technology is far from being able to separate matter waves for space-like separated detection, this is the criterion to be tested for the system of this dissertation. However, to exclusively rule out any possibility that a state is separable can be challenging most of the times and so called entanglement witnesses are used. These witnesses are constructed such that, given the violation of a boundary, no separable state can be used to describe the measurement outcome [149]. The Bell inequalities are by far not the only ones to witness entanglement, but are usually exploited for spin-like systems, e.g. photons [23], ions [25], Josephson junction qubits [150], where internal degrees of freedom are entangled. In the following sections it will become obvious why violating a Bell inequality, as clear as it serves as an entanglement witness[8], is hard to realize experimentally and other witnesses might be more useful.

The internal degrees are alluring to use for entanglement as their coupling to the environment is small, compared to particles moving through space and time. By coupling to the environment the coherence of the superpositions is lost and the state decoheres to a mixed state with eventually no entanglement left for verification. Interestingly, the effect of coupling to the environment is of the same nature as the entanglement of the two systems. The interaction with the environment establishes an entanglement between the environment and the system. This leads to an information flux from and into the environment, which if read out corresponds to a measurement. However, a measurement destroys the superposition. Thus, the coupling to the environment in principle offers the possibility to gain information of the system, destroy the superposition, and with this the entanglement. This notion of information and superposition will be important again when a closer look at different paths of the particles will be given.

The only candidates so far succeeding in demonstrating EPR like correlations in their external degrees of freedom are photons produced in a spontaneous parametric down conversion process (SPDC) [34, 151–154]. Photons propagating in free space are neither disturbed by electric, nor magnetic fields, and their effects in gravity are faint. Thus, they are ideal in terms of low decoherence during propagation through space and time.

In the next section it will be shown how exploiting the quadrature phase operators can be used to demonstrate EPR correlation in a system of two momentum entangled particles, which is then extended to the situation of matter waves as well.

---

[8]Discriminating quantum mechanics against other theories goes beyond the boundaries of quantum mechanics and thus, violating a Bell inequality certainly implies much more than being an entanglement witness.

4.2 Concept of double-diamond experiments

After this general overview of entanglement and its terminology, this section will turn towards the specific situation of systems entangled in their external degree in the spirit of the original EPR gedankenexperiment. The widely employed mechanism to create entangled photons happens in a nonlinear crystal, where highly energetic photons split their energy onto two daughter photons. This process of spontaneous parametric down conversion (SPDC) is well understood in the field of nonlinear optics [155]. While developed for strong fields for second harmonic generation, the interaction of two fields in the crystal can be simplified by incorporating the non-linearity χ^2 of the crystal into a single coupling constant g_0 and neglecting all other orders. This yields then in second quantization

$$|\Psi\rangle = g_0 \int \int (\hat{a}_{\vec{p}_a}^\dagger \, \hat{b}_{\vec{p}_b}^\dagger \, \hat{c} \, \hat{d} + \hat{a}_{\vec{p}_a} \, \hat{b}_{\vec{p}_b} \, \hat{c}^\dagger \, \hat{d}^\dagger)|0011\rangle d\vec{p}_a d\vec{p}_b \qquad (4.7)$$

where a, b and c, d are the annihilation operators for the two outgoing modes and two incoming modes, respectively. They need to fulfill phase matching conditions, i.e. conserve momentum and energy as well as support coherent amplification while the incoming fields propagate through the crystal. One of the two incoming modes, say c is typically a strong coherent light field and the second one, d, is populated by the vacuum and the quantum fluctuations therein. Therefore the name "spontaneous". Upon interaction with the crystal the modes are populated, where due to momentum conservation particle A always occupies a mode with opposite momentum to the momentum of particle B in the co-moving frame of the strong light field ($\vec{p}_a = -\vec{p}_b$). In general, this results in two forward directed light cones, each for every photon. High production rates of these photon pairs however allow to select only two distinct modes of the cones and the respective modes on the cone of the partner photon and results in the entangled output state

$$|\Psi\rangle = \frac{1}{\sqrt{2}} \left(|p_{a1}p_{b2}\rangle + |p_{a2}p_{b1}\rangle \right) \qquad (4.8)$$

Double Diamond

The integral in eq. (4.7) is an extension of a two-mode squeezed state [156] where only one single p_{k1} would be considered. However, to show entanglement in a two mode squeezed state a strong coherent field is required as a local oscillator in the homodyne detection of the photons. While this is feasible for light, particle conservation renders it extremely unlikely to be used for matter waves. However, by extending the state with the p_{k2}-mode, a natural source for the local oscillator is generated at the same time. Fig. 4.1 shows a schematic of how an entanglement experiment would look like for such a state in a double-diamond configuration. The name "double diamond" arises from the two paths on each side describing each a diamond. The two modes for each photon are reflected and interfered again on a beam splitter. Using retardation plates in one arm of each photon, the relative phase between the two paths can be adjusted and thus, the quadratures (see top row of fig. 4.1) of both photons scanned. This way the additional second paths substitute the strong coherent field impinging
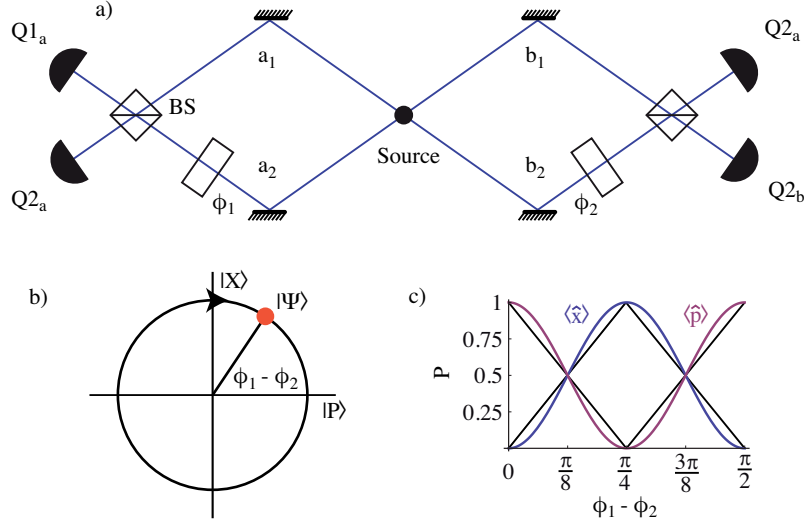
Figure 4.1: a) A schematic of the setup for a double-diamond measurement to verify entanglement of a state given by eq. (4.17). The two photons are generated in the source and can either take path $\{a_1, b_2\}$ or $\{a_2, b_1\}$, with each side describing a diamond when reflected by mirrors. The two paths interfere again on a beam splitter and retardation plates are used to adjust the relative phases for homodyning. b) By varying the relative phase difference $\phi_1 - \phi_2$ the phase quadratures $\hat{x}$ and $\hat{p}$ can be scanned, i.e. the complete relevant phase space accessed. c) The quantum mechanical projective measurement on one of the two axes yields then a sinusoidal dependence. The black lines indicate the linear trend of classical theories obeying the Cauchy-Schwarz inequality, yet reproducing quantum mechanical results at $\phi_1 - \phi_2 = 0, \pi/4, \pi/2$.

on the second input of the beam splitter in the two mode squeezed situation. In both cases the two output modes of the beam splitters are monitored with detectors on each side. With the phase plates ϕ_1 and ϕ_2 and the 50/50-beam splitter, where the reflected beams experience a phase shift of $\pi/2$, one can calculate the state at the bucket detectors $Q1_a$, $Q1_b$, $Q2_a$, and $Q2_b$ in the output modes of the beam splitter:

$$|\Psi\rangle = \frac{1}{\sqrt{2}} \left(|P\rangle + |X\rangle \right) \tag{4.9}$$

$$= \left(|Q1_a Q1_b\rangle + |Q2_a Q2_b\rangle \right) \cos\left(\frac{\phi_1 - \phi_2}{2} \right) \tag{4.10}$$

$$+ \left(|Q1_a Q2_b\rangle + |Q2_a Q1_b\rangle \right) \sin\left(\frac{\phi_1 - \phi_2}{2} \right)$$

where $|X\rangle$ and $|P\rangle$ are the eigenstates to the phase quadratures

$$\hat{x} = \frac{|Q1_a Q2_b\rangle\langle Q1_a Q2_b| + |Q2_a Q1_b\rangle\langle Q2_a Q1_b|}{2} \tag{4.11}$$

and

$$\hat{p} = \frac{|Q1_a Q1_b\rangle\langle Q1_a Q1_b| + |Q2_a Q2_b\rangle\langle Q2_a Q2_b|}{2} \tag{4.12}$$

respectively. While $\hat{x}$ measures coincidences of crossed detectors, $\hat{p}$ measure the coincidences if parallel detectors click.

Hence, at all detectors a detection is equally probable with probability $1/2$ as required for an entangled state. However, upon conditional detection the outcomes become correlated in a, typical for quantum mechanics, sinusoidal dependence on the relative phase. For example same detectors always click (i.e. both Q1s or both Q2s) if the relative phase is zero, or the crossed detectors click (i.e. Q1 clicks for one particle while Q2 clicks for the other particle) if the relative phase is π. Additionally, the phase can be adjusted such that all angles in between are accessible, in particular the ones where quantum mechanics deviate from the linear trend of classical physics and local hidden variable theories.

This experiment was originally proposed by Horne et al. [63] in a time when SPDC sources were not that developed. Nevertheless, before considering matter waves of massive particles they analyzed a system of photons, which at that time were envisioned to be created in positronium annihilation yielding entangled γ-rays. The realization of the proposal by Rarity and Tapster [34] eventually confirmed the predictions of quantum mechanics using photons of SPDC. However, whether massive particles exhibit similar correlations or experience decoherence due to, e.g. gravity, remains an open question for experimental physics. Even though neutron experiments, because of their weak interaction with the environment, were at the forefront of fundamental research [3–6], because of this weak interaction, now among each other, they were not candidates for sources of entangled pairs. Yet, with the advent of laser cooling and the achievement of Bose-Einstein condensation, the strong interaction of atoms in collisions has become attractive to be exploited for such experiments. Many proposals investigate the possibility of using dissociating molecules in the BCS-BEC crossover [134, 157, 158]. The similarities of eq. (4.7) and eq. (3.3) however are striking and the experiments by Perin et al. [51, 52] are promising that the four-wave mixing process (FWM) yields a test bed for an EPR experiment with massive particles in their external degree of freedom.

The SPDC source relies on proper alignment of the crystal and the laser beam, which creates the strong coherent light field to drive the process. Only under certain angles a phase matching is fulfilled that allows for a coherent population of the desired modes and a decent output of photons in those modes. As this phase matching condition only supports a limited amount of modes, collecting the photons at reasonable count rates is feasible. The FWM process of chapter 3 however, is solely governed by the low energetic scattering parameter describing s-wave scattering. Hence, the produced atom pairs do not only lie on selected modes but are isotropically scattered over all 4π of the whole solid angle. This makes it hard to collect the atoms, especially as the mirrors in atom optics are usually made out of Bragg laser pulses [60, 129, 159, 160]. Bragg pulses only resonantly reflect certain velocity classes which have a Doppler shift smaller than the linewidth. This is difficult to construct for a three-dimensional, expanding cloud. There exist proposals and attempts to realize phase matching conditions in FWM of matter waves by em-
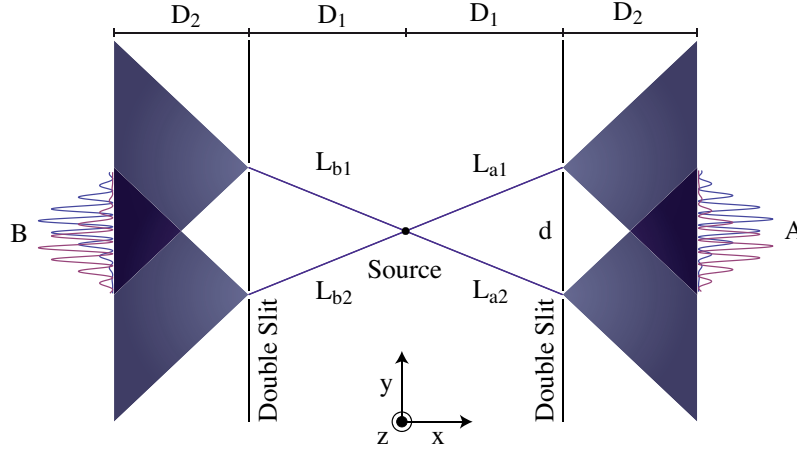
Figure 4.2: The mirrors of a double-diamond setup can be substituted by double-slits. Diffraction at these slits cause an overlap of the two different paths at the screen and result in an interference pattern in conditional detection if the two partners are entangled. As the pattern only arises in conditional detection, the pattern on either side can be shifted to different locations for the detection on the other side. Note, the arrangement drawn in 2D neglects gravity which points in opposite direction to the z-axis. This is justified as long as the slits do not have a z-component as only the transversal momentum uncertainty Δp_y defines the pattern and the magnitude $|p_x|$ scales the pattern at the screen.

ploying moving standing waves of the Raman lasers [161–163], which are promising pathways to increase count rates.

The rf method of ref. [53] already showed similar beam profiles as SPDC sources and atom correlations to verify the existence of correlations in this process have been measured [54]. However, the phase matching condition in the rf scheme relies on density fluctuations of the BEC itself. To enter the stimulated (directed beam) regime high densities are required. In section 4.5.2 it will be shown that demonstrating entanglement, requires pair identification of the respective partners. After all, for high densities and thus, high pair production rates this identification is very challenging even for DLDs.

Double double-slit

Another way to again overlap the two paths without using mirrors is to use the diffraction of a wave at small slits. Fig. 4.2 illustrates the altered scheme of the double-diamond experiment. Just like in ordinary single-particle interference at a double-slit the waves coming from each slit are diffracted and the divergent waves overlap again in the far field. The screen consists of an array of bucket detectors.

To analyze the situation it will be assumed that the FWM process has populated the scattering modes spontaneously (compare chapter 3.1.2) and only these modes are considered for further analysis. Particle A can then take either path L_{a1} or L_{a2}

while particle B takes path L_{b1} or L_{b2}

$$|\phi\rangle = |L_{a1}\,L_{b1}\rangle + |L_{a2}\,L_{b2}\rangle + |L_{a1}\,L_{b2}\rangle + |L_{a2}\,L_{b1}\rangle \qquad (4.13)$$

For this qualitative analysis $|\phi\rangle$ is not normalized and for the pattern on the screen only the phase resulting from each path is relevant

$$|L_{ai}\,L_{bj}\rangle = \exp\left(-ik_{rec}L_{ai}(y_a, y_s)\right)\exp\left(-ik_{rec}L_{bj}(y_b, y_s)\right) \qquad (4.14)$$

For the full quantum mechanical state, though, all possible paths contributing to the pattern have to be considered [164, 165]. In a simplified picture of a one dimensional source along the y-axis this can be taken into account by adding up all possible paths for the particles, in particular different positions of the source y_s. Hence, the path lengths of the particles $L_{ai,bj}(y_{a,b}, y_s)$ depend on the location of the collision in the source y_s, the position[9] y_a where particle A is detected, respectively the position y_b where particle B is detected. The path lengths L_{kl} for particle $k = a, b$ on path $l = 1, 2$ can be geometrically calculated to be

$$L_{kl}(y_k, y_s) = \sqrt{\left(\frac{d}{2} + (-1)^l y_k\right)^2 + D_2^2} + \sqrt{\left(\frac{d}{2} + (-1)^l y_s\right)^2 + D_1^2} \qquad (4.15)$$

Here d is the distance between the two slits and D_1 and D_2 describe the distance between the source and the slits, and the distance between the slits and the screen, respectively. As the two particles originate from the same position of the collision of two incoming atoms, y_s is the same for both particles. For the analysis of conditional detection the width of the slits s is taken to be zero. A finite slit width only results in an envelope of the fringe[10] pattern and does not change the result of conditional detection as long as the slit width remains smaller than the slit distance. Superposing all possible paths the particles can take to reach the screen yields the state

$$\Psi(y_a, y_b) = \int_s |\phi(y_s, y_a, y_b)\rangle dy_s \qquad (4.16)$$

This integration will yield in general a state Ψ' at the double slits which has terms for the crossed passage a_c and parallel passage a_p of particles through the slits

$$|\Psi'\rangle = a_c\left(|p_{a1}p_{b2}\rangle + |p_{a2}p_{b1}\rangle\right) + a_p\left(|p_{a1}p_{b1}\rangle + |p_{a2}p_{b2}\rangle\right) \qquad (4.17)$$

For analyzing the specific situation of collided atoms it is important to understand that the state produced during FWM is far from being perfectly anti-correlated. The atoms before the Raman transition are not at perfect rest, but their velocities are limited by their zero point fluctuations governed by the trap geometry. Owing to Heisenberg's uncertainty principle, the spatial confinement leads to a momentum uncertainty (see chapter 2.9 and chapter 3.1). Hence, the atoms have an initial momentum uncertainty which is transferred on to the outgoing modes. In other words, the center of mass motion of the two colliding atoms is not zero before and is

---

[9]Note the label of the coordinate has been changed from x to y to be consistent with the coordinate system used in previous chapters and match the experimental conditions of this dissertation.

[10]The term fringe describes the sinusoidal pattern arising from the interference of different slits.

not zero after the Raman transition and the s-wave scattering of the atoms. Hence, the correlations in momentum of the atoms are limited by the size of the source and ultimately by the initial momentum uncertainty in the BEC.

Fig. 4.3 displays the probability of detecting particle A at position y_a conditional on the detection of particle B at position y_b as a result of a numerical integration over the whole source size s_y for this state. The significance of the two other dimensions only marginally changes the pattern and is neglected. This demonstrates nicely the importance of the size of the source and at the same time casts light on the importance of information in the realm of quantum mechanics. If the source is too small, the initial momentum uncertainty is too large. Hence, the correlations between the two particles are too weak to establish a conditional pattern on the screen. On the other hand, the momentum uncertainty for the individual particles is so large that the single particle can go through both slits at the same time. The high momentum uncertainty leads to a product state for the two-particle wave function of the two single-particle wave functions, i.e. a separable state. With the single-particle uncertainty of its transversal momentum Δp_y the condition for this to happen is the same as for the single-particle interference pattern to arise [166–169]

$$\Delta p_y \ll m v_{rec} \frac{d}{D_1} \tag{4.18}$$

When the source size increases the initial momentum uncertainty decreases and the correlations become stronger $\Delta p_y \sim 1/s_y$. Hence, the information through which slit particle A goes is carried by particle B, and vice versa. For example, in principle it would be possible to detect particle B and infer through which slit particle A went. This knowledge of which-path information means the latter particle was not able to go through both slits at the same time and the single-particle interference disappears. The first particle, say particle B, that allows to predict through which slit particle A went, does not even need to be detected. The information would then decohere into the environment and the interference would still be lost. However, the diffraction at the double-slit causes the two possible paths of particle B to overlap again and with this the possibility to identify through which slit the other particle went. This overlap makes the two paths of particle B indistinguishable for the detector and corresponds to an erasure of the information which path particle A takes that was carried by particle B, a so called quantum erasure [170–172]. The inseparability of this state is indicated by a $\cos(y_a - y_b)$ dependence of the conditional probability (compare eq. (4.9)). Hence, while in single-particle detection no pattern is visible, a detection conditioned on a detection on the other side will give an interference pattern.

One could assume now increasing the source size even further will enhance the correlations. Indeed the correlations become better. Yet, as the source size gets on the order of the slit distance the contribution of $|L_{a1} L_{b1}\rangle$ and $|L_{a2} L_{b2}\rangle$ increases as well. This causes the two amplitudes for crossed a_c and parallel a_p slit passage of the two particles to become equal (compare eq (4.13)). Hence, the state can be written as a separable product state again. The detection of a particle in either slit does not hold an information about which slit the other particle went through and, thus the
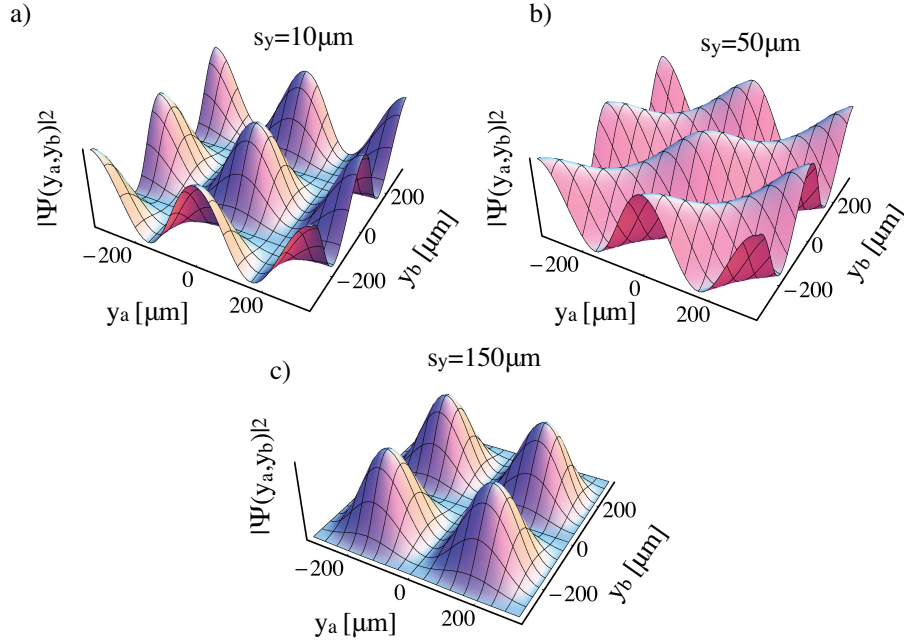
Figure 4.3: Double double-slit scenario: The probability distribution of conditional detection of particle A and particle B at position y_a and y_b, respectively. Parameters for the numerical integration are $D_1 = 5\,\text{mm}$, $D_2 = 30\,\text{mm}$, and $d = 100\,\mu\text{m}$. The source size is varied from $s_y = 10\,\mu\text{m}$, $50\,\mu\text{m}$, and $150\,\mu\text{m}$ demonstrating the three regimes. For too small sources a) each particle can go through both slits at the same time causing single-particle interference. b) When the source size increases and hence, the correlation improves, which-way information could be in principle obtained from the partner and the single-particle interference disappears. However, conditional fringes indicate the entanglement of the two particles. c) Contributions from parallel passage a_p through upper or lower paths make the state separable again and single-particle interference becomes visible again, as a detection of a particle at either slit does not hold an information about which path the other particle took.

single-particle interference pattern arises again[11] at the cost of loss of two-particle interference. The condition to avoid this situation is to have a smaller source size than the slit distance [169]

$$s_y \ll d \tag{4.19}$$

As long as the source is large enough it is always possible to achieve a genuine two-particle interference by keeping the slit distance larger. However, from a practical point of view the interference fringes need to be resolved by a detector. The fringe distance d_f scales inversely with the slit distance. In chapter 3.2 the spatial resolution

---

[11]In general the phase of the single-particle interference now depends on the relative position of the slits from the source to the distance to the screen

of the DLD is measured to be $\delta_{x,y} = 124\,\mu m$[12]. Hence, the correlations of fig. 4.3 are already unlikely to be resolved and a third condition applies to an experimental realization[13]

$$d < \frac{2\pi D_2}{5 k_{rec} \delta_{x,y}} \tag{4.20}$$

An interesting feature of such a slit version of the double-diamond experiment is that the bucket detectors in the two output modes of the beam splitter are replaced by an array of detectors. Each position of such a bucket detector corresponds to a different relative phase between the waves coming from the different slits. Hence, by looking at different detectors one can virtually change the phase of the double-diamond experiment. However, this can only serve as an entanglement witness, as a violation of a Bell inequality requires an active setting of the measurement basis. This is to say, the atoms detected at different positions could be described by different local hidden variables and thus, a violation of the Bell inequality would need an additional assumption that the particles are all from the same ensemble, independent from where they are detected.

There are possible ways to overcome the lack of the missing active phase change. In chapter 2.2 it was discussed how an off-resonant light field can shift the energy levels of an atom. This energy shift corresponds to a different phase evolution for a particle within the light field and the situation without the light field. Hence, a phase shift can be introduced. Shining such a laser on one of the slits can be used to control the phase of the matter wave by changing the power of the laser. Moreover, this phase control can be used to form the slits itself. Substituting the whole double-slit arrangement with a standing light wave would create a whole array of slits that could all contribute to the pattern and no particles were lost at the massive wall, yielding higher count rates. Changing the phase of the two laser fields creating the standing wave would then be a handle to change the phase again. However, care has to be taken to still fulfill the three conditions to see genuine two-particle interference as mentioned before as well as the three dimensionality of the scattering halo has to be taken into account. Hence, such an experiment would require very delicate design and control of the setup.

4.3 Theory of ghost-interference

In the preceding section it was argued that a large source is required to achieve a reasonable correlation between the momenta of the atoms. However, the distance between the two slits had to be even larger than the source to avoid a separable state at the detector. The slit distance determines the fringe distance and thus, has to be kept small to be still able to resolve the fringes with the detector. A simpler situation arises when the slits in the path of particle B are omitted (see fig. 4.4). Eq. (4.13) reduces then to

---

[12]In principle δ_z could be used as well. However, this makes the analysis much harder as gravitation would need to be taken into account and could even lead to decoherence

[13]Here the factor of 1/5 is chosen to incorporate 5 data points per fringe. Indeed, it will be seen later that this is a good approximation to achieve reasonable results
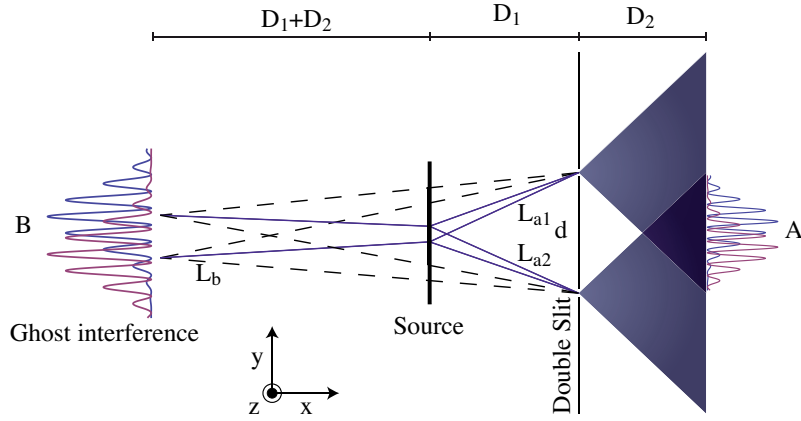
Figure 4.4: Simplifying the double double-slit setup by removing the slits in the path of particle B removes the restriction that the source size must not be larger than the slit distance, but can still yield conditional interference, called ghost-interference. The purple lines show the paths to calculate the geometrical phases, while the dotted black lines illustrate the Klyshko picture. With the Klyshko picture the interference pattern on the right hand side can be explained by taking the left-hand side as source for a single particle and connect it to the right-hand side through the correlations in the source.

$$|\phi\rangle = |L_{a1}\, L_b\rangle + |L_{a2}\, L_b\rangle \tag{4.21}$$

The situation of only one pair of slits in the path of one particle and not the other is generally referred to as ghost-interference. Even though only particle A passes through a double-slit and no double-slit is in the path of particle B an interference pattern can arise at position y_b in conditional detection. There is extensive literature about ghost imaging [173–175] and ghost-interference [176, 177] however, while ghost imaging can be performed by classical light, ghost-interference is a non-classical feature of quantum mechanics. Ghost imaging can be achieved by correlated classical light, where an object in the path of particle A is visible in the conditional detection of particle B as well. Ghost-interference goes one step further. Here the basis in which one measures can be chosen freely as allowed by quantum mechanics and one still obtains the conditional pattern, showing stronger than classical correlations.

For a qualitative analysis of the ghost-interference the calculations are analog to the ones for the double double-slit scenario, but using eq. (4.21). Fig. 4.5 demonstrates the new situation with the conditional probabilities displayed. In this situation the two-particle interference pattern does not disappear even when the source becomes larger than the slit distance, as no additional possibilities for the paths arise. However, the source needs to have a certain size to establish good momentum correlations and prohibit single-particle interference. If the source is too small a single-particle interference can be observed on screen a and only a as expected.

An intuition of this phenomenon can be gained by applying the Klyshko picture [176]. The particles from the source are emitted in random directions. However,
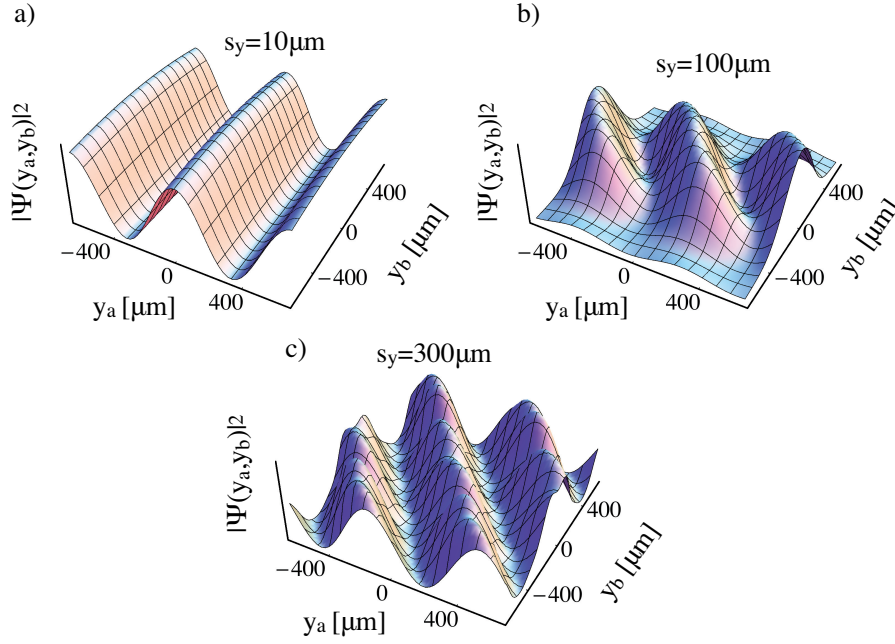
a)

$s_y=10\mu m$

$|\Psi(y_a,y_b)|^2$

$y_a\,[\mu m]$

$y_b\,[\mu m]$

b)

$s_y=100\mu m$

$|\Psi(y_a,y_b)|^2$

$y_a\,[\mu m]$

$y_b\,[\mu m]$

c)

$s_y=300\mu m$

$|\Psi(y_a,y_b)|^2$

$y_a\,[\mu m]$

$y_b\,[\mu m]$

Figure 4.5: Ghost-interference: The probability distribution of conditional detection of particle A and particle B at position y_a and y_b, respectively. Parameters for the numerical integration are $D_1 = 5\,\mathrm{mm}$, $D_2 = 30\,\mathrm{mm}$, and $d = 100\,\mu\mathrm{m}$. The source size is varied from $s_y = 10\,\mu\mathrm{m}$, $100\,\mu\mathrm{m}$, and $300\,\mu\mathrm{m}$. Now the condition that the source must be smaller than the slit distance can be dropped and only two regimes exist of single-particle and conditional interference.

if the momenta are well correlated, the virtual path of particle A can be reconstructed by following particle B. Therefore, taking the source for the two-particle state as the bridge[14] between two paths of just one single particle originating from the position where particle B is detected. This describes why the pattern on screen a moves when the location where particle B is detected differs, i.e. the source position for a single particle in the Klyshko picture is different. It is this ability to change the outcome of a measurement of the particle A by measuring particle B and vice versa that is made accessible by the quantum mechanical correlations and could not be achieved by classical correlated light.

In the ghost-interference experiment no other contributions start to arise when the source becomes larger as no additional path possibilities exist for particle B. The fact that a large source is possible to guarantee the momentum correlation while at the same time keep the slit distance still small, gives the advantage to have resolvable fringe distances (compare fig. 4.5). However, this comes at the cost of losing control over two distinguished paths. The relative phase of the two paths of particle B cannot be accessed by means of an additional laser. A local hidden variable model cannot be ruled out anymore as the active phase change cannot be performed on both sides anymore. Moreover, it was shown that ghost imaging can

---

[14]The original Klyshko picture is for SPDC where the crystal can be taken as a mirror, giving the same result as here

be performed by using classical light. So the question arises how to verify that the above discussed conditional pattern can only be explained by quantum correlations.

4.4 Fringe visibility

To test if a two-particle interference pattern can only be explained by quantum correlations, the visibility of the fringes can serve as a measure. This section clarifies the definition of the visibility for two-particle interference and its complimentarity to single-particle interference and shows how a criterion of visibility arises for quantum correlations. While the visibility in general is useful to discriminate quantum from classical correlations in the realm of pure states, the visibility can serve as an entanglement witness as well.

It is instructive to first only investigate the separability of pure bipartite states (compare eq. (4.13)). A measure of entanglement in such a state is called concurrence C in quantum theory and quantifies the non-classical phase correlation between the two parties of the entangled system. For the pure bipartite state from eq. (4.13) the degree of entanglement is given by the difference between the parallel terms and the crossed ones [178]

$$C = 2|a_c^2 - a_p^2| \tag{4.22}$$

In measurements, the observable to quantify the entanglement has to have a relation to the amplitude of the sinusoidal fringes, called visibility. In general, the visibility for single-particle interference v_i is defined as[15]

$$v_k = \frac{I(y_k)_{max} - I(y_k)_{min}}{I(y_k)_{max} + I(y_k)_{min}} \tag{4.23}$$

However, extending eq. (4.23) for the two-particle probabilities would serve as a wrong measure for entanglement. The two-particle visibility is still unity even in the case of a too small source where any sinusoidal pattern is simply due to local single-particle interference (compare fig. 4.3). To avoid such misleading situations a better definition is thus to subtract the product of the two single-particle probabilities from the two-particle probability and then add the square of the background single-particle probability $A_n = d\,k/\pi$ to counteract overcompensation [179, 180]

$$\bar{I}(y_a, y_b) = I(y_a, y_b) - I(y_a)I(y_b) + A_n^2 \tag{4.24}$$

With this modified probabilities the correct two-particle visibility reads

$$v_{ab} = \frac{\bar{I}(y_a, y_b)_{max} - \bar{I}(y_a, y_b)_{min}}{\bar{I}(y_a, y_b)_{max} + \bar{I}(y_a, y_b)_{min}} \tag{4.25}$$

and for pure states is equivalent to the concurrence. With these definitions it can then be shown that [178, 181][16]

$$v_{ab}^2 + v_k^2 \leq 1 \tag{4.26}$$

---

[15]In the later discussion the pattern will have an additional envelope. Nevertheless, the visibility is only defined with the oscillating term (compare e.g. eq. (4.32)).

[16]The reference to Jaeger et al. provides a nice discussion of this complementarity

where the equal sign holds for pure states. In the discussions about the different regimes of the source size for the setup it was already mentioned that it is necessary to avoid single-particle interference to maximize the two-particle interference as seen by equation eq. (4.26) as well. Another complementarity adding to the which-path discussion from above is obtained by the distinguishability of the paths $\mathcal{D}$, i.e. a knowledge that can in principle be gained about which path the particle takes. In general

$$\mathcal{D}_k^2 + v_k^2 \leq 1 \tag{4.27}$$

must hold while the equality is again given for pure states. The similarities of the two equations eq. (4.26) and eq. (4.27) are obvious and yield the sufficiency of a high two-particle visibility to guarantee a high distinguishability. Interestingly, while eq. (4.26) contains the two-particle quantity v_{ab}, the distinguishability is a single-particle quantity. This asymmetry results from the fact that the entangled partner of a two-particle system carries the information of distinguishability through which slit the other single particle went. Furthermore, in principle this information could be measured, which makes the two paths distinguishable, and thus the single-particle visibility has to vanish.

Now most of the discussion was focused around pure states. However, while in theory everything is perfect, in experiments rarely anything is. Hence, the pure states degrade to mixed states. While in the pure state scenario it is sufficient to obtain any finite two-particle visibility to claim entanglement, for mixed states this does not hold anymore. If information about entanglement is lost into the environment, then there are situations allowed where the two-particle visibility of classical light can exceed the concurrence, i.e. it is not possible anymore to conclude from any finite two-particle visibility directly to entanglement.

To still differentiate between classical and quantum correlations, the stochastic properties of classical light can be exploited [182]. In this situation the phenomenon of conditional particle interference is best captured in the normalized second order correlation function $g^{(2)}(y_a, y_b)$, that was introduced in chapter 3.1. It describes the normalized probability to find a particle at y_a conditioned on detecting a particle at y_b. Qualitatively this is equivalent to the unnormalized probability distribution displayed in fig. 4.3 and 4.5. In general the second order correlation function is defined by the position dependent annihilation $\hat{a}(y_i)$ and creation $\hat{a}^\dagger(y_i)$ operators

$$g^{(2)}(y_a, y_b) = \frac{\langle \hat{a}^\dagger(y_a)\hat{a}^\dagger(y_b)\hat{a}(y_a)\hat{a}(y_b)\rangle_\Psi}{\langle \hat{a}^\dagger(y_a)\hat{a}(y_a)\rangle_\Psi \langle \hat{a}^\dagger(y_b)\hat{a}(y_b)\rangle_\Psi} \tag{4.28}$$

where the average is taken over an ensemble of particles in state Ψ. However, in classical statistics the quantities are no operators and thus do not need to be normally ordered:

$$g^{(2)}(y_a, y_b) = \frac{\langle a^*(y_a)a(y_a)a^*(y_b)a(y_b)\rangle_P}{\langle a^*(y_a)a(y_a)\rangle_P \langle a^*(y_b)a(y_b)\rangle_P} \tag{4.29}$$

$$= \frac{\langle I(y_a)I(y_b)\rangle_P}{\langle I(y_a)\rangle_P \langle I(y_b)\rangle_P}$$

For a field obeying just a phase difference, this can hold the similar sinusoidal dependence on the difference of the location of the detectors as quantum mechanics [183]. For this dependence to be maximal the single-particle interference has to be minimized following eq. (4.26) and hence zero single-particle fluctuations yield highest two-particle visibilities

$$\langle I(y_i)\rangle = \langle I_1\rangle + \langle I_2\rangle \tag{4.30}$$

where I_k are the intensities resulting from the two different paths on both sides of the source. This also holds for the ghost-interference situation where it is not obvious that there are two paths. However, the paths of the second particle have different spots in the source where they originate from as the Klyshko picture illustrates.

Hence, in the situation where the phase is random such that the single-particle interference is averaged out and vanishes the two-particle interference can arise

$$\langle I(y_a)I(y_b)\rangle_P = \langle I_1^2\rangle + \langle I_2^2\rangle + 2\langle I_1 I_2\rangle \left[1 + \cos\left(d\, k_{rec}\left(y_a - y_b\right)\right)\right] \tag{4.31}$$

Here it is assumed the that intensity passing through slit k on both sides to be the same, which is necessary to maximize the two-particle visibility[17] . Inserting this into the classical definition for $g^{(2)}$ the two-particle correlation function can be written as [182]

$$g^{(2)}(y_a, y_b) = A\left[1 + v_{ab}\cos\left(d\, k_{rec}(y_a - y_b)\right)\right] \tag{4.32}$$

where the parameters A and the two-particle visibility v_{ab} are used for clarity. They are given by:

$$A = \frac{\langle I^2(y_a)\rangle + \langle I^2(y_b)\rangle + 2\langle I(y_a)I(y_b)\rangle}{\left(I(y_a) + I(y_b)\right)^2} \tag{4.33}$$

and

$$v_{ab} = \frac{2\langle I_1 I_2\rangle}{\langle I_1^2\rangle + \langle I_2^2\rangle + 2\langle I_1 I_2\rangle} \tag{4.34}$$

For classical stochastic correlations again a Cauchy-Schwarz inequality holds and as a consequence $\langle I_1^2\rangle + \langle I_2^2\rangle \geq 2\langle I_1 I_2\rangle$. With this the two-particle visibility for classical light cannot exceed $1/2$. Hence, a non-classical, i.e. quantum correlation has to be responsible for two-particle visibilities larger than $1/2$ [182]

$$v_{ab} > \frac{1}{2} \tag{4.35}$$

This visibility criterion can be easily read out of the experimentally observed pattern and hence, is a first indicator for quantum mechanical correlations. There is ongoing research on how to construct an entanglement witness for such a pattern to include even mixed quantum mechanical states [158, 163, 184, 185]. However, as a first proof of quantum mechanical correlations the visibility criterion will be used to discuss the feasibility of a ghost-interference experiment in the subsequent section.

---

[17]Note, that the two individual particles do not necessarily need to emit from the same slit in order to obtain two-particle interference.

4.5 The devised experiment

The preceding sections introduced the conceptual ideas of demonstrating entanglement in the external degree of freedom of matter waves and laid the foundation for this section, where the devised experiment to be first realized on the new platform of this dissertation is presented. An approach adapted from quantum optics is used to analytically calculate the expected pattern in conditional two-particle detection. Finally, the parameter range of the system with respect to the feasibility of performing such an experiment is discussed.

4.5.1 The spherical wave approximation

To calculate the conditional probabilities for the double-slit and ghost-interference experiment all possible ways originating from the source were summed up. This worked well when the possible ways through the slits where given (compare eq.(4.16)). In ref. [168] the authors showed that for a SPDC source the correlations in forward direction in principle can be obtained by integrating over the source region with spherical waves as Green's functions. The coherence of the BEC gives the possibility to follow the same approach in the case of FWM[18].

To transfer this, it is useful to enter a frame co-moving with the center of mass motion. This way the effect of gravitation can be neglected and will only be required to retrieve the numerical values in the end. Let the two particles then emit from just a single point source with constant momentum given by the momentum kick from the Raman lasers $k_0 = k_{rec}$. This is analog to eq. (4.14), where all possible phase contributions from different spots in the source were considered.

The analysis of momentum correlation happens in the far field and thus, will be described by angles so that a finite uncertainty in the magnitude of the longitudinal momenta will not change the angle dependent pattern. The state in the far field can than be written as

$$\Psi(\vec{r}_a, \vec{r}_b) = \frac{e^{ik_{rec}|\vec{r}_a|}}{|\vec{r}_a|} \frac{e^{ik_{rec}|\vec{r}_b|}}{|\vec{r}_b|} = \psi(\vec{r}_a)\psi(\vec{r}_b) \qquad (4.36)$$

As there is no dependence of the detection of particle A at position $\vec{r}_a$ on the detection of particle B at position $\vec{r}_b$ this is a product state and does not contain correlations. However, the wave function of the initial particle before collision is described by the Thomas-Fermi parabola (compare chapter 2.9). The coherence of the BEC given by the single-particle wave function does not allow for a distinguishability from where the pair was emitted within the source and hence, all possibilities need to be summed up, weighted by the density of the single-particle wave function $\phi(\vec{r}')$.

$$\Psi(\vec{r}_a, \vec{r}_b) = \int_V |\phi(\vec{r}')|^2 \frac{e^{ik_{rec}|\vec{r}_a - \vec{r}'|}}{|\vec{r}_a - \vec{r}'|} \frac{e^{ik_{rec}|\vec{r}_b - \vec{r}'|}}{|\vec{r}_b - \vec{r}'|} d\vec{r}' \qquad (4.37)$$

To investigate the momentum correlations the observation is done in the far field at position r_i so that $r_i \gg r'$. With this $|\vec{r}_i - \vec{r}'| \simeq r_i - \vec{r}'\vec{r}_i/r_i$ and $|\vec{r}_i - \vec{r}'|^{-1} \simeq r_i^{-1}$,

---

[18]Again, to analyze the pattern the dynamics during FWM are neglected and only the scattered atoms are discussed

and eq. (4.37) can be rewritten as the Fourier transform of the density profile[19]. Underlining the momentum space characteristic of the measured probability distribution the wave function is here given as function of the wave vectors $\vec{k}_a$ and $\vec{k}_b$

$$\Psi(\vec{k}_a, \vec{k}_b) = \frac{1}{(2\pi)^{3/2}} \int_V |\phi(\vec{r}')|^2 e^{-i(\vec{k}_a + \vec{k}_b)\vec{r}'} d\vec{r}' \qquad (4.38)$$

To write the equation in this form the wave vectors where identified to be $\vec{k}_i \equiv k_{rec} \vec{r}_i / r_i$ and the factor in front of the integral is to normalize properly in the far field.

To justify this fairly simple approach, which for most situations can be calculated analytically, the results of Perrin et al. can be compared to predictions by eq. (4.38). The integration over an inverted parabola of a BEC in one dimension yields

$$\Psi(k_{a,y}, k_{b,y}) = \frac{3\sin\left(s_y\left(k_{a,y} + k_{b,y}\right)\right) - 3s_y\left(k_{a,y} + k_{b,y}\right)\cos\left(s_y\left(k_{a,y} + k_{b,y}\right)\right)}{\sqrt{2\pi}s_y^3\left(k_{a,y} + k_{b,y}\right)^3} \quad (4.39)$$

Fig. 4.6 shows a comparison of the correlations between the spherical wave approximation, the numerical calculations of ref. [136], and the experimental data of ref. [51]. While the numerical simulation is somewhat closer to the experimental result, the simple numerical approach only differs by about 10%. This is remarkable as no initial momentum uncertainty of the original BEC had to be taken into account, neither were mean field interactions between the atoms, nor time scales on which the collisions happen taken into account. Their effects will be discussed later. However, the good agreement motivates to use this model for further analysis.

Another remarkable feature of this approach is that the correlations arise merely from the summation of coherent point sources. Just as in simple Fourier optics, where a single beam is more collimated if emitted by a larger source, the correlations become stronger if a larger source participates in the creation process. Notably, when this approach was first used by Horne et al. [168] they only considered the half sphere in which the two photons could be emitted. However, the s-wave scattering in the FWM is isotropic and can in principle populate all 4π, even the collinear half sphere. Hence, there is no a priori reason why atoms should not be detected next to each other. As a matter of fact if only a point source is considered this is actually what happens. Fig. 4.7 shows the probability distribution to detect particle B relative to particle A for different source sizes. For very small source sizes $s_y \ll 2\pi/k_{rec}$, the probability to find the second particle is uniform over the whole sphere, no matter where the first particle was detected. However, as the source grows, the second particle becomes more and more localized on the opposite side of the sphere with respect to the first particle. This way momentum conservation comes in naturally for a large enough source [20].

This simple formulation will be used to analyze the parameters for the envisioned experiment and test the feasibility of the system and extended by a discussions about finite collision time and interacting particles when needed.

---

[19]These calculations follow an unpublished draft by Mandip Singh.

[20]The apparent momentum violation for very small source sizes is a result of the high initial momentum uncertainty caused by Heisenberg's uncertainty principle and does not contradict physical reality.
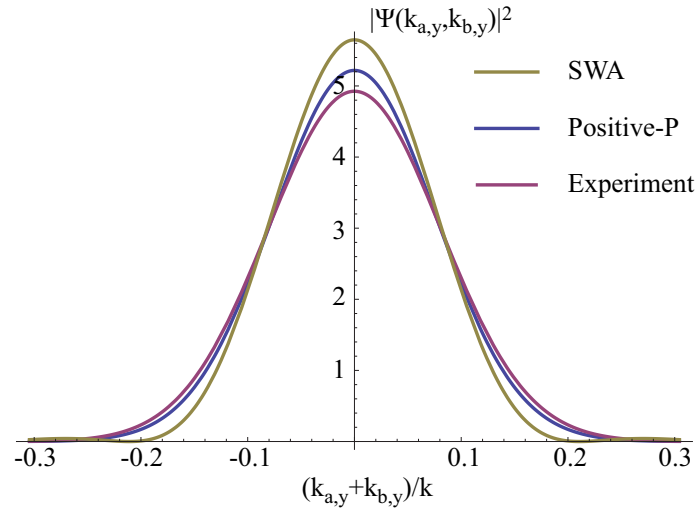
Figure 4.6: A comparison of the prediction by the spherical wave approximation and the numerical positive P method as well as experimental results of Perrin et al. show a good agreement and justifies the simple approach. The curves for the experiment and the numerical simulation are simple Gaussian distributions with the rms-value given in ref. [51] and ref. [136], respectively.

4.5.2 The feasibility analysis

In the preceding sections it was discussed how the spherical wave approximation (SWA) can be used to calculate the correlations of two particles scattered out of the BEC into an entangled state of two counter-propagating waves. It was also shown how a ghost-interference setup can be used to identify the entanglement. A double-slit placed in the path of one of the particles can then cause a conditional interference pattern on either side. In this situation the fringe distance depends on the distance between the slits and the distance between the position of the slits with respect to the screen, i.e. detector. The larger the distance from the screen, the more time the particles have to expand and hence, the fringe distance increases and the interference pattern is easier to resolve. The maximal distance can be achieved by placing the slits right at the position where the source is. Hence, a modulation of the source itself yields the best resolvable interference pattern. Experimentally, this is appealing as well, as no additional components for the slits have to be introduced into the vacuum chamber.

Multiple collision zones

One way to achieve the altered situation of having the "slits" as source is by splitting the BEC into two parts. This can be done by introducing a blue detuned light sheet that rejects the atoms from the middle of the BEC and forms a double source ("double well"). However, the coherence over both sources has to be preserved and hence, the barrier height has to be accurately controlled to allow for tunneling [186, 187]. A different approach is to avoid the manipulation of the main BEC, this way maintain-
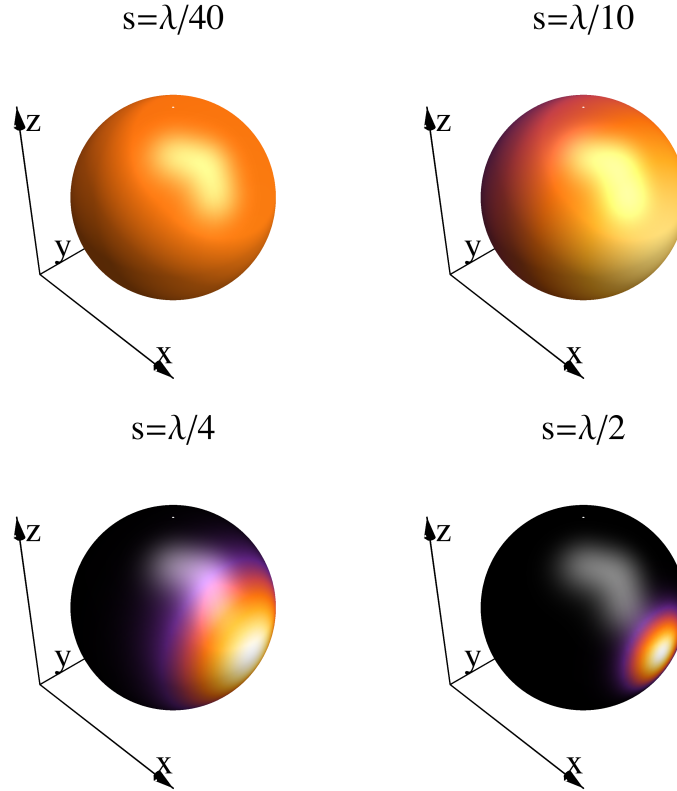
Figure 4.7: The probability of detecting particle B when particle A is detected at $-k_{rec}\vec{e}_x$. As the source size grows the momentum conservation comes in naturally by using the spherical wave approximation. When the source size s_y is smaller than the wavelength λ, the probability of finding particle B on the same side as particle A is still significant. The larger the source the better is the anti-correlation in momentum of the two emitted atoms. Note, the shiny spot in the upper right part of the spheres is a result of the three-dimensional presentation of the probability sphere and is not part of the probability distribution itself.

ing the coherence and thus the relative phases, but to create counter-propagating waves at two different locations in the BEC. This can be achieved by means of the Raman lasers. Fig. 4.8 shows a schematic of the arrangement of the laser beams to create a modulated source for the colliding particles. The spatial light modulator (SLM) for the Raman laser beam L2 propagating in -z-direction can be used to shape the beam such that different regions in the BEC are selected to initiate the FWM process.

An advantage of creating the slits within the BEC is that the whole pattern arising at the detector is now governed by the source and no intermediate components need to be taken into account. Hence, the SWA can be used as is and makes the analysis of the experiment more feasible. In this situation the weighted integration is not over the whole BEC $|\phi(\vec{r}')|^2$ anymore but rather over the area where the atoms are coupled out by the laser beams $|\phi'(\vec{r}')|^2$. The SLM imprints a pattern of two slits with Gaussian shape and width $s_{x,y} = w_0$ in a distance d into the BEC. The
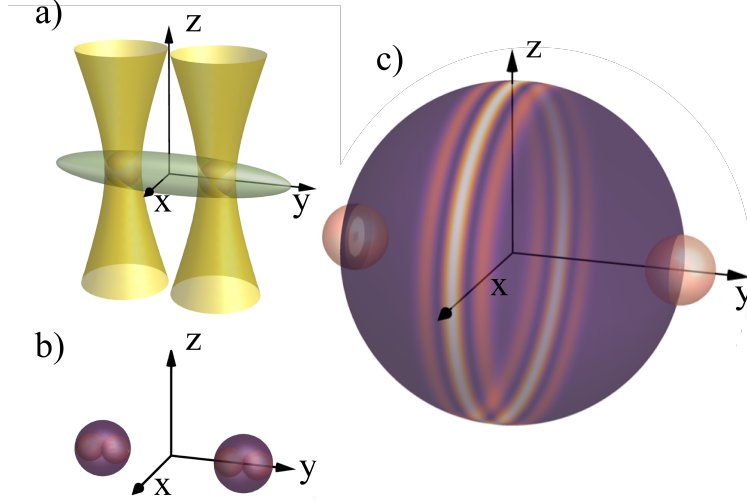
Figure 4.8: A schematic of how a ghost-interference experiment can be realized in the system. a) The SLM modulates the laser beam $L2$ such that it generates small spots in the BEC. b) Atoms are only coupled out of the BEC in those regions which serve as collision zones from where the spherical waves are emitted. As the atoms are in a superposition of being at either spot, these regions serve as sources for the entanglement. The small red spheres are the unscattered, conuter-propagating waves from each source spot, while the purple halo is a result of the FWM process. c) When the waves from the two zones start to overlap in the far field they interfere and in conditional detection the fringes become visible.

source size in z-direction is still given by the Thomas-Fermi radius of the BEC. However, the z-direction only gives the envelope of the distribution perpendicular to the interference pattern which reveals the entanglement. Thus, for simplicity of the integration the distribution is still calculated with a Gaussian distribution as in the other two directions

$$|\phi'(x')|^2 = \frac{1}{\sqrt{(2\pi)}s_x} \exp\left(-\frac{x'^2}{2s_x^2}\right) \tag{4.40}$$

$$|\phi'(y')|^2 = \frac{1}{\sqrt{(8\pi)}s_y} \left[\exp\left(-\frac{(y'+d/2)^2}{2s_y^2}\right) + \exp\left(-\frac{(y'-d/2)^2}{2s_y^2}\right)\right]$$

$$|\phi'(z')|^2 = \frac{1}{\sqrt{(2\pi)}s_z} \exp\left(-\frac{(z')^2}{2s_z^2}\right)$$

The integrals of eq. (4.38) can be evaluated independently and hold for the two-

particle probability distribution in x- and z-direction

$$\Psi_i(k_{a,i}, k_{b,i}) = \frac{e^{-\frac{1}{2}s_i^2\left(k_{a,i}+k_{b,i}\right)^2}}{\sqrt{2\pi}} \tag{4.41}$$

with $i = x, z$. In y-direction the superposition of the two Gaussian distributions gives in addition to this envelope a oscillatory term indicated by the imaginary i

$$\Psi_y(k_{a,y}, k_{b,y}) = \frac{\left(1 + e^{id\left(k_{a,y}+k_{b,y}\right)}\right) e^{\left(-\frac{1}{2}\left(k_{a,y}+k_{b,y}\right)\left(s_y^2\left(k_{a,y}+k_{b,y}\right)+id\right)\right)}}{2\sqrt{2\pi}} \tag{4.42}$$

The oscillations will become more apparent when the probabilities are computed. In spherical coordinates and with $k_i = k_{rec}$ the absolute square of the wave function has in three dimensions the explicit form

$$|\Psi(\vec{k}_a, \vec{k}_b)|^2 = |\Psi(\phi_a, \theta_a, \phi_b, \theta_b)|^2 \tag{4.43}$$

$$= \frac{1}{16\pi^3}\left\{1 + \cos\left[d\,k_{rec}\left(\sin(\theta_a)\sin(\phi_a) + \sin(\theta_b)\sin(\phi_b)\right)\right]\right\}$$

$$\exp\left\{-2k^2s^2\left[1 + \sin(\theta_a)\sin(\theta_b)\cos(\phi_a - \phi_b) + \cos(\theta_a)\cos(\theta_b)\right]\right\}$$

where the first bracket holds the conditional fringe pattern showing entanglement and the second bracket gives the envelope given by the source size $s = s_x = s_y = s_z$, including momentum conservation. For clarity of the equation the source sizes are set to be equal as they only determine the envelopes as described by eq. (4.41). For the inverted parabola distribution of a BEC, the envelope would be replaced by the absolute square of eq. (4.39). Fig. 4.9 shows exemplarily how the fringe pattern of detection of particle B conditional on detection of particle A is visible in the xz-plane. The probability distribution where particle B is detected moves depending on the position where particle A is detected. When particle A is detected close to the y-axis, the two source spots in the BEC become, viewed from the detection position, aligned behind each other. Hence, they do not reveal a lateral interference pattern[21].

For clarity of fig. 4.9, the spot sizes of the source were assumed to be half the wavelength. The small source size "enlarges" the pattern on the sphere and makes it easier to recognize. This illustrates how the situation changes when the slits are inside the source. In contrast to the situation of the regular double double-slit or even ghost-interference where the goal was to achieve a source size as large as possible in order to achieve good momentum anti-correlation, this setup benefits from smallest possible spot sizes within the BEC. The smaller the spots the larger the envelope for the pattern. This requirement was neglected in the earlier consideration by taking the slit widths to zero resulting in infinite widths for the envelopes. However, in the experiment considered here one does not need to worry about the momentum anti-correlation of the two particles before the slit[22]. The condition to avoid single-particle

---

[21]Due to the first order time dependence of the Schrödinger equation an interference in longitudinal direction can potentially be observed.

[22]Later, in the analysis it will be discussed how the anti-correlations in the directions perpendicular (x and z) to the interference pattern in y-direction do play a role for detection of the particle in coincidences.

$$\vec{k}_a = -k_{\mathrm{rec}}\vec{e}_x \qquad\qquad \vec{k}_a = -k_{\mathrm{rec}}\vec{e}_z$$

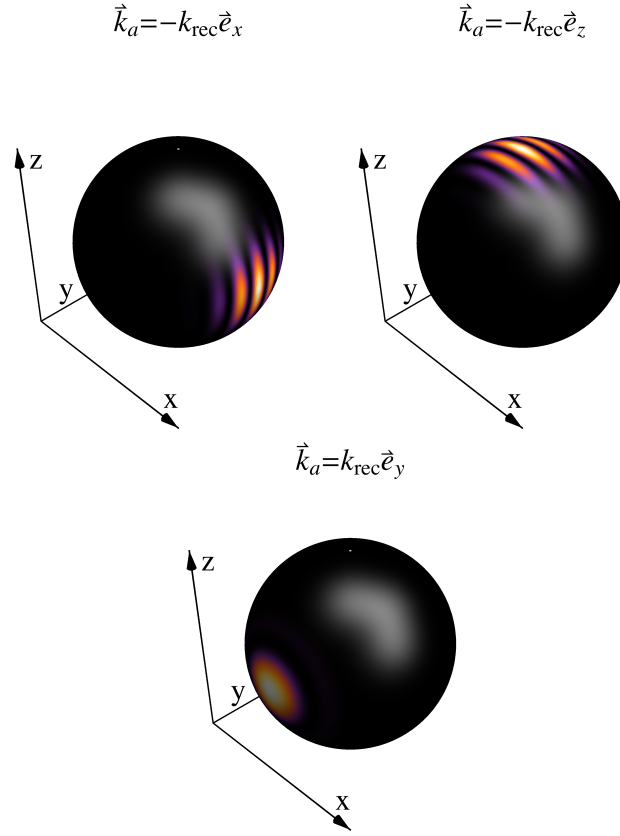$$\vec{k}_a = k_{\mathrm{rec}}\vec{e}_y$$

Figure 4.9: The probability distribution of the scattering halo for detecting particle B, when particle A is detected at $\vec{k}_a = -k_{rec}\vec{e}_x$, $\vec{k}_a = -k_{rec}\vec{e}_z$, and $\vec{k}_a = k_{rec}\vec{e}_y$, respectively. Depending on the detection of particle A a conditional interference pattern can be observed for particle B. As the setup is symmetric around the y-axis the pattern can be observed in the whole xz-plane, while it disappears for detections close to the y-axis.

interference (see eq. (4.18)) is always fulfilled and the EPR-like entanglement is a result of the superposition of two positions rather than the a priori anti-correlation of momenta. In that sense the source size only matters for the overlap of the two waves from the different spots in the far field and define the envelope of the pattern. Hence, the SLM has to create tunable patterns which have smallest possible beam waists.

Before continuing with an analysis of the setup using the spherical wave approximation it is worthwhile to consider two more effects neglected by this approach. The mean field interaction as well as the finite pair creation time are not captured in the SWA.

Even though the SWA predictions was within 10% of the experimental data of ref. [51] and even closer to the numerical results [136], the mean field interactions play a role in the correlation in momenta. However, they lead to a broadened distribution, i.e. they have the same effect as a smaller spot size. So by using the SWA for the experimental situation described here the envelope is rather underestimated and additional broadening by interactions will enhance the pattern in the sense that

the envelope comprises more fringes. This justifies to use the SWA even to obtain numerical values, keeping in mind that the envelope might be a little bit wider.

Eq. (4.43) is given in dependence of angles, assuming perfectly monochromatic waves with wave vector[23] $k = k_{rec}$. However, this conceals that the width of the shell of scattered atoms is finite as well. This is limited by the initial momentum spread within the BEC, but can be broadened by the pair creation time. There are two timescales which can define this creation time. One is given by the linear dispersion of the cloud after being released from the trap and can be calculated by the inverse of the radial trap frequency $\tau_{LD} = m s_{x,y,z}^2/2\hbar \approx 1/\omega_{x,z}$ (compare eq. (3.6)). The other one is given by the separation of the two counter-propagating clouds, which serve as source for the scattered pairs. When they do not overlap anymore no pairs are produced, which happens after $\tau_s = m s_y/\sqrt{2}\hbar k$ (compare eq. (3.4)). The width of the shell is then given by $\delta k = m/\hbar k\, \tau_{LD,s}$, with whichever τ is smaller. Hence, as long as the expansion time is larger than the separation time the width of the shell is determined by the inverse of the source size $\delta k = \sqrt{2}/s_{x,y,z}$. For spots in the BEC on the order of a few µm the cloud separation time becomes $\sim 65\,\mu s$, while the expansion time is on the order of $\sim 200\,\mu s$.

Now it is possible that one wave packet from one spot collides with one packet from the other spot, resulting in a third collision zone in the middle. This would result in a three slit interference pattern at the detector. However, the time before they collide in this third zone is only after $\sim 300\,\mu s$, on the order of the expansion time. Hence, the incoming matter waves for the FWM process are already considerably diluted and will only generate wave-amplitudes that contribute negligibly to the interference pattern. Actually, the SLM easily generates a third or even more spots on purpose within the BEC. This will be an intriguing future experiment where eventually Born's rule can be tested, i.e. that the absolute square of the quantum mechanical wave function corresponds to the probability to detect the particle, [181] in the spirit of the photon experiment of ref. [188].

With these considerations in mind, eq. (4.43) can be used to estimate the feasibility of such an experiment in the current system. The first challenge is to be able to resolve the pattern with the detector. Hence, slit distance d and detector resolution $\delta_{x,y,z}$ are the figures of merit. Additionally, the envelope has to be wide enough to support at least the first order of the interference pattern. Hence, the beam waist w_0 is important as well. Fig. 4.10 shows that with the results from chapter 3 the first order is just supported and can be resolved by the detector.

With eq. (3.8) the three-dimensional data, recorded by the detector in space and time, can be transformed back into the spherical momentum distribution. For clarity, for the remainder of this section the resulting three-dimensional pattern is interpreted as it will be in the experimental realization. Firstly, the radius dependence is averaged out. In order to obtain decent count rates, each detection of coincident events is also rotated around the origin such that all detection events of particle A fall on $\phi'_a = \pi$ and $\theta'_a = \pi/2$. In this way a two dimensional pattern of only the relative coordinates is obtained for a detection at side B conditioned on a detection

---

[23]In ref. [132] it is shown that taking an atom out of the BEC adds the chemical potential to its momentum. On the other hand, occupying a mode of the outgoing waves as a distinguishable particle even requires a little bit more energy. However, for the analysis this effect is neglected as k is only a few percent smaller than k_{rec}.
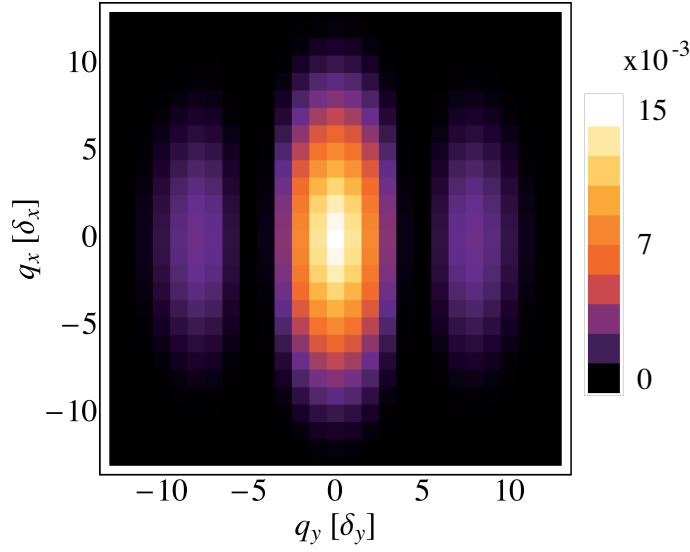
Figure 4.10: The expected interference pattern on side B, given a detection on side A and rotated as described in the text. The angle dependence is given in multiples of the detector resolution. The fringe distance spans about seven pixels to just barely resolve the interference pattern for a source size $s_y = w_0 = 8.5\,\mu$m and a slit distance of $d = \sqrt{2}\pi s = 37.8\,\mu$m.

at side A

$$|\Psi_{b|a}(q_x, q_y)|^2 = \frac{k^2 s_y s_x}{\pi D^2 \left(e^{-\frac{d^2}{4sy^2}} + 1\right)} \left[\cos\left(d\,k\,q_y/D\right) + 1\right] e^{-\frac{k^2}{D^2}(s_y^2 q_y^2 + s_x^2 q_x^2)} \qquad (4.44)$$

where D is the radius of the scattering halo at the detector and $\sin\theta'_b = q_x/D$ as well as $\sin\phi'_b = q_y/D$ was used. For the height of the cloud $H = 80$ cm above the DLD and the recoil velocity of the Raman transition the radius of the scattering halo at the detector is $D = 37.1$ mm.

This interpretation of the experimental data has two distinct consequences in the cases of the polar and azimuthal dimension. If not the polar coordinate of the first particle, but only the relative angle in this direction is used, this is equivalent to averaging over a larger sample to obtain better statistics. Each particle remains in its respective fringe when rotated. Doing this for the azimuthal coordinate implies even more. If this averaging still yields an interference pattern the averaging is equivalent to measuring at different relative phases between the two paths of particle A. Hence, if the interference pattern is not washed out by the rotation, not only are better statistics achieved, but this situation also indicates the existence of the same pattern in all bases, e.g. in the two basis $|X\rangle$ and $|P\rangle$ in the case of the double-diamond experiment (see section 4.2), which is required for entanglement.

In contrast to the original ghost-interference idea with the slits outside the BEC, in the scenario with the two sources within the BEC it even becomes possible to violate Bell's inequality. Obviously the aforementioned averaging would not be allowed anymore. However, by shining an additional detuned laser on one of the source spots to introduce a phase shift gives the possibility to change the phase of the two respec-

tive paths again as in the double-slit scenario (see fig. 4.2). Different intensities on either side would give the possibility to even have different phase changes for side A and B, which is required for a Bell measurement. In that sense, the envisioned experiment is more a hybrid of a double double-slit experiment and a ghost-interference experiment.

Separability-criterion with modular variables

To analyze the significance of quantum mechanical correlations over classical correlations in the following subsection, the visibility that can be achieved with the current system will be analyzed. However, from the analysis so far an intuitive understanding of the entanglement in context of the EPR-inequality (4.4) can be seen in fig. 4.10, namely the reduced uncertainty in one variable without a loss of certainty in the conjugate variable.

In the work of Gneiting et al. [185], they employ modular variables [189–191] that split the momentum operator p into the periodic $\bar{p} = (p + h/2d)mod(h/d) - h/2d$, and an integer part N_p

$$p = N_p\frac{h}{d} + \bar{p} \tag{4.45}$$

and in similar fashion the position y into $\bar{y} = (y + d/2)mod(d) - d/2$ and N_y

$$y = N_y d + \bar{y} \tag{4.46}$$

The interference pattern with its envelope and the periodic fringe pattern is then described by the respective parts of the momentum, i.e. the oscillations in momentum space is solely governed by $\bar{p}$ and the envelope by $N_p h/d$. Interestingly, while the modular variables commute with each other, and so do the integer parts ($[\bar{y}, \bar{p}] = 0$ and $[N_y, N_p] = 0$), the integer part of one observable does not commute with the modular variable of the other and vice versa ($[\bar{y}, N_y] \neq 0$ and $[\bar{p}, N_p] \neq 0$). With this Gneiting et al. construct a separability criterion similar to eq. (4.4) for the relative integer position $N_{y,rel} = N_{y,1} - N_{y,2}$ and total modular momentum $\bar{p}_{tot} = \bar{p}_1 + \bar{p}_2$

$$\langle(\Delta N_{y,rel})^2\rangle + \frac{d^2}{h^2}\langle(\Delta \bar{p}_{tot})^2\rangle \leq 2C \tag{4.47}$$

where d is the slit distance, h the Planck constant and $C \simeq 0.078235$. This condition can only be fulfilled by an entangled state and discriminates them from separable states. Illustratively this means for a separable state, that the reduction of the uncertainty in the relative position comes at the cost of an increase in uncertainty of the total momentum, as discussed when the importance of the source size for the anti-correlation of momenta was stressed (the smaller the source size the larger the momentum spread, see section 4.2). However, with the double-source for entangled states the uncertainties of the modular variables can be independently reduced. To see this one has to confirm that both particles originate from the same source region of the hybrid experiment[24] and thus $\langle(\Delta N_{y,rel})^2\rangle = 0$. Then the reduced width of

---

[24]In case of the double double-slit experiment, it would be necessary to confirm that they went through "anti-correlated slits", i.e. the particles pass through the upper slit if the partner goes through the lower slit and vice versa

the modular momentum as seen in the width of one fringe can be smaller than the width of the single source spot, which is close to the limit for a separable state, as seen in the envelope of the pattern (compare fig. 4.10) to exclude separability. Moreover, the uncertainty of the modular momentum does not change when the source size is reduced. This underlines again that the smallest possible source size is an advantage rather than a problem as one could expect because the anti-correlation of the momenta becomes weaker.

A qualitative effect of the entanglement in this interpretation can be seen in fig. 4.10. While the source size for q_x and q_y are the same, the width of the zeroth order fringe can be independently reduced in y-direction by changing d, somehow analog to a squeezing in this direction. Assuming each pair always originates from the same source region (as they do in the scattering process, however without proof in the experiment), the separability criterion for modular variables is fulfilled in y-direction[25]

$$\frac{d^2}{h^2}\langle(\Delta\bar{p}_{y,tot})^2\rangle = \frac{\pi^2 - 3}{6\pi} < 2C \tag{4.48}$$

$$\frac{d^2}{h^2}\langle(\Delta\bar{p}_{x,tot})^2\rangle = \frac{1}{6} > 2C$$

To verify $\langle(\Delta N_{y,rel})^2\rangle = 0$ in a double double-slit experiment a control experiment can be performed where the slits are removed and from the anti-correlation in momenta it can be excluded that the particles do not originate from the anti-correlated slits. However, in the envisioned experiment such a verification would really require to measure the relative position of the pairs that close to the collision regions that it is impossible to have been created in the other source region. This is impossible if using a DLD 80 cm below the BEC and a different verification scheme would be necessary or additional assumptions would be required which would weaken the modular variable argument.

A final remark relating the criterion of Gneiting et al. and the visibility: if the uncertainty of the integer part is guaranteed to be zero, the modular variable criterion is solely given by the variance of the total modular momenta and a visibility of already 20.1% excludes a separable mixed state. Yet, as the aforementioned, simple control experiment to verify $\langle(\Delta N_{y,rel})^2\rangle = 0$ is only applicable to the double double-slit version of the experiment, criterion (4.47) can only be employed in a future, full blown double double-slit experiment and the here discussed hybrid experiment is left with the visibility criterion[26] $v_{ab} \geq 1/2$.

Visibilities

The signature of entanglement in all discussed scenarios is heralded by the disappearance of single-particle interference, but only visible in coincidence detection on both sides A and B. Essential for the coincidence measurements, single atoms need to be detected, which is the reason for using He* atoms in combination with the

---

[25]As there is no double slit in x-direction, the number is only given for comparison and cannot be related to the modular variable criterion.

[26]Interestingly, as no entanglement is existent in the classical stochastic theories that can achieve this visibility, the particles creating such a pattern cannot always originate from the same slit.

delay-line detector (DLD). Yet, single-atom detection is only a prerequisite for the coincidences. The main challenge is to identify the pairs, i.e. the correct partner has to be associated with its counterpart on the other side of the momentum sphere. Due to the native correlation length of back-to-back scattered atoms, i.e. the width of the Gaussian distribution of eq. (4.44), which defines a mode volume, the partner-atom can be discriminated against other atoms. On the other hand, falsely associating particles to each other which are not correlated will diminish the visibility of the interference pattern. Hence, it is delicate to choose the right coincidence window that determines whether a partner was detected, and the correct amount of pairs produced in the first place.

The angular coincidence window CW on the sphere has to span at least the first order maximum of the pattern (see fig. 4.10) in azimuthal direction to make this fringe visible and has then a free parameter c, which is the width in polar direction in units of the width of the Gaussian distribution $1/\sqrt{2}s_x k$ describing the correlations. Hence, the area on the sphere of the coincidence windows is obtained by integration over $\pi/2 \pm c/\sqrt{2}s_x k$ in polar direction and $\pm 1/\sqrt{2}s_y k$ in azimuthal direction.

$$CW = \int_{\frac{1}{\sqrt{2}s_y k}}^{\frac{1}{\sqrt{2}s_y k}} \int_{\pi/2-\frac{c}{\sqrt{2}s_x k}}^{\pi/2+\frac{c}{\sqrt{2}s_x k}} \sin\theta \, d\theta \, d\phi = \frac{4}{\sqrt{2}s_y k} \sin\left(\frac{c}{\sqrt{2}s_x k}\right) \qquad (4.49)$$

Now the good coincidence counts GC are the emitted atoms per steradian, $N = N_s/4\pi$, times the detection efficiency η on each side times the probability that the partner is in the coincidence window. Latter probability is given by the Gaussian correlation distribution, integrated over the coincidence window. Hence the good coincidences are

$$GC = N\eta^2 \text{erf}\left(\frac{c}{\sqrt{2}}\right) \text{erf}\left(\frac{1}{\sqrt{2}}\right) \qquad (4.50)$$

The accidental counts AC, i.e. counts where two detection events are misinterpreted as correlated atoms, are made up out of three contributions. Either a particle from one pair and a particle from another pair are detected within the coincidence window, while the respective partner is lost, and are associated to be a pair[27] $CW(\eta(1-\eta)N)^2$; a dark count of the detector on either side and a particle with a lost partner on the other side within the coincidence window are associated $2CW\,DC\eta(1-\eta)N$ (DC are the dark counts per steradian of the detector[28]); or two dark counts are accidentally identified to be a pair $CW\,DC^2$. The three contributions can be summarized as [192]

$$AC = CW(DC + \eta(1-\eta)N)^2 \qquad (4.51)$$

---

[27]This is an approximation to the Poisson distribution of detection events, valid if $CW\eta N \ll 0.1$. The coincidence window is on the order of 10^{-4} sr and together with the detection efficiency guarantees the validity of the approximation

[28]The dark counts per second of chapter 3.2 can be converted into DC if the thickness of the scattering halo is known.

Hence, choosing the coincidence window to be small yields low accidental counts, but as it becomes smaller than the native mode volume, the low accidental count rates come at the cost of a high rejection of good coincidences.

The smaller the coincidence window the better the visibility as expected. However, longer integration times are required as the coincidence rate decreases. The minimal coincidence window that can be chosen is limited by one pixel of the detector resolution to

$$c_{min} = \frac{\sqrt{2}\delta_x k s_x}{D} \tag{4.52}$$

In principle the coincidence window parameter can change when detection is in the equatorial plane as the temporal resolution is much better. However, for simplicity and to stay on the conservative side the problem is kept symmetric around the y-axis and hence, the calculations are made with the detector resolution in x-direction.

Neglecting where specifically the first particle was detected averages over the distribution so that the two-particle visibility v_{ab} is equivalent to the definition of the one particle visibility and can be calculated from the count rates of coincidences CC and accidentals

$$v_{ab} = \frac{CC - AC}{CC + AC} = \frac{GC}{GC + 2 \cdot AC} \tag{4.53}$$

Even though the efficiency of the detector is only about 7% the low dark count rate of the detector compared to optical detection schemes suggests a good visibility for the pattern.

Fig. 4.11a shows the visibility in dependence of emitted pairs. The visibility increases linearly with less pairs produced per shot. However, at some point dark counts start to dominate the accidental count rate and the visibility decreases again for too low pair production rates[29]. Shown is also the dependence of the visibility above $1/2$ in units of the standard deviation σ for a fixed number of shots. Here, the maximum is shifted towards higher numbers of pairs.

Parameter	Value
$\delta_{x,z,y}$	$124\,\mu\mathrm{m}$
$s_{x,y,z}$	$8.5\,\mu\mathrm{m}$
d	$37.8\,\mu\mathrm{m}$
Dark counts	$6\,\mathrm{s}^{-1}$
H	$80\,\mathrm{cm}$
η	0.07

Table 4.1: A summary of the parameters used to obtain numerical results and plots.

Fig. 4.11b shows how the visibility can slightly be improved by increasing the source sizes s_x and s_z perpendicular to the interference pattern. A better correlation in this dimension increases the probability to find the scattering partner within the coincidence window. Fig. 4.13a shows the probability to detect a particle per Raman

---

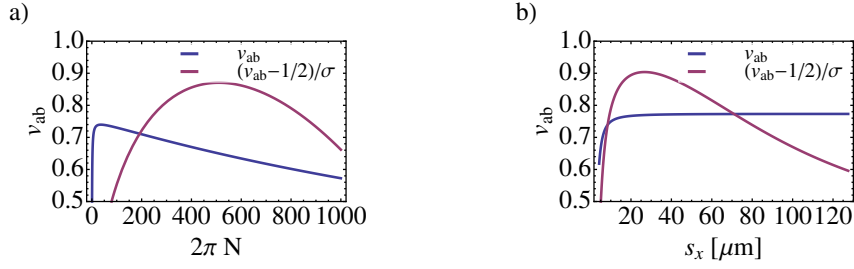[29]The optimum visibility is on the order of $\eta N = DC$.

a)

b)

Figure 4.11: The achievable visibility versus the pair production rate per shot $2\pi N$ and the source size s_x perpendicular to the dimension of the interference. a) The pair production rate, even though favorable to be small to avoid high accidental count rates, can enter a regime where dark counts can dominate the accidental count rate and outbalance the good coincidences. Even more pronounced is the disadvantage of too low numbers of scattered pairs, when the visibility is plotted in units of its standard deviation above $1/2$ (Here, 400 light pulses per pixel are used to generate the statistics). b) Some improvement on the visibility can be achieved by increasing the source size $s_{x,z}$ perpendicular to the interference pattern. A better correlation in these dimensions increases the probability to find the partner within the coincidence window. However, when s_y/s_x becomes small, the pattern out of the xz-plane degrades and the useful area of the sphere is smaller (see fig. 4.12). Hence, the count rate drops (Here, 200 Atoms are scattered in the FWM-process). A collection of other parameters can be found in tab. 4.1.

pulse, when half of the sphere can be used to collect events. This is possible if the source size $s_{x,z}$ and s_y in the different directions are equal. One handle to improve the visibility is to increase the correlations perpendicular to the interference pattern, hence increasing the source size in x- and z-direction. However, as the pattern is more and more restricted to the xz-plane less area on the sphere can be used. Fig. 4.12 shows how the height of the first order maximum decreases relative to the zeroth order maximum as the particles are detected closer to the y-axis and how the width of this curve reduces for higher ratios of $s_{x,z}$ to s_y. Hence, less area of the scattering halo can be used to obtain better statistics. Nevertheless, if required, such an increase in source size can be easily achieved by shaping the L2 beam in the Fourier plane of the focusing lens (compare chapter 3.1.4).

The visibilities after the considerations of accidental identification of partners are fairly high. However, another major effect is posed by the finite resolution of the detector. The pattern recorded does not perfectly follow eq. (4.44), but the result is the convolution of the pattern with the detector resolution $\delta_{x,y}$

$$|\tilde{\Psi}_x(q_x)|^2 = \frac{1}{\sqrt{2\pi(\delta_x^2 + \frac{D}{2s_x^2 k^2})}} \exp\left(-\frac{q_x^2}{2(\delta_x^2 + \frac{D}{2s_x^2 k^2})}\right) \tag{4.54}$$
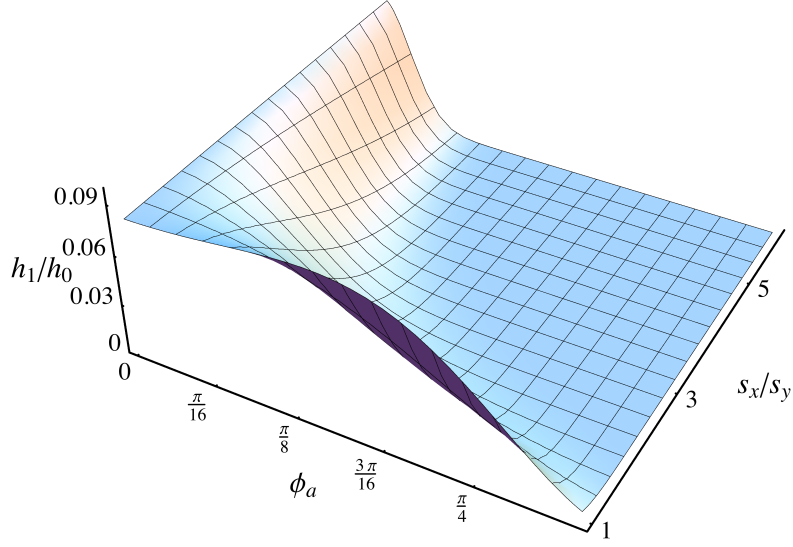
Figure 4.12: As the detection of the particles (here labeled with the detection angle ϕ_a of particle A) gets closer to the y-axis the interference pattern diminishes as the two source spots, viewed from the detection position, line up behind each other. The height of the first order maximum h_1 relative to the zero order h_0 is shown. As the source size s_x increases relative to s_y the useful angles are reduced.

for the polar dimension and

$$|\tilde{\Psi}_y(q_y)|^2 = \frac{1}{A}e^{-Eq_y^2}(1 + V\cos Fq_y) \tag{4.55}$$

for the azimuthal. The four parameters are the wider envelope

$$E = \frac{4k^2s_y^4}{8k^2s_y^4\delta_y^2 + 4D^2s_y^2} \tag{4.56}$$

the shifted frequency of the oscillations in the pattern

$$F = \frac{dkD}{2k^2s_y^2\delta_y^2 + D^2} \tag{4.57}$$

the normalization constant

$$A = \sqrt{\pi}\sqrt{\frac{D^2}{k^2s_y^2} + 2\delta_y^2}\left(e^{-\frac{d^2\left(\frac{D^4}{s_y^2(2k^2s_y^2\delta_y^2+D^2)}+2k^2\delta_y^2\right)}{4D^2}} + 1\right) \tag{4.58}$$

and the reduced visibility

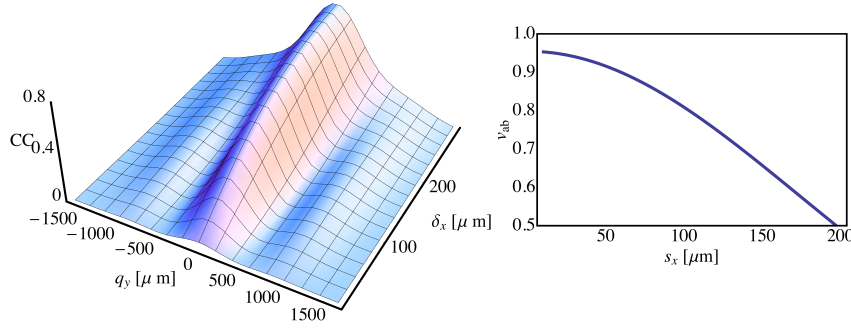$$V = e^{-\frac{d^2k^2\delta_y^2}{2D^2}} \tag{4.59}$$

Figure 4.13: The intensity pattern on side B given a detection on side A (per shot) resulting from the EPR-like entanglement in the source with the accidental coincidences are taken into account. The count rate increases as the detector resolution gets larger, because the minimal coincidence window has to be increased. However, the visibility starts to decrease significantly when the detector resolution gets on the same order as the fringe distance, more clearly visible in the right graph.

While the detector resolution broadens the envelope it also lowers the frequency at which the maxima of the interference pattern appear. More importantly for the visibility criterion, the visibility is reduced even with perfect pair identification.

In order to combine the results for the influence on the interference pattern from the finite detector resolution with the considerations about accidental pair identifications, the reduced visibility has to be scaled with the good coincidences. The minimum of the pattern yields then an additional contribution to the accidental count rate AC'

$$AC' = GC\frac{1-V}{2} + AC \tag{4.60}$$

and the expected coincidence rate CC' is reduced by the maximum of eq. (4.55) to

$$CC' = GC\frac{1+V}{2} + AC \tag{4.61}$$

Fig. 4.11 already included these considerations. However, the mere number obscures the fact that the first order maximum can vanish for the naked eye in the background even though the visibility is still high. This is owing to the fact that the visibility is only concerned with the oscillatory term and neglects the envelope, which is justified as the modular variable criterion also only requires the width of the of the fringes to be narrow. Fig. 4.13 shows how the interference pattern degrades and is washed out as the detector resolution approaches the fringe distance.

Note, to obtain decent count rates and thus statistics it can be useful to sacrifice some visibility by increasing the coincidence window and/or the scattered pairs per shot (compare fig. 4.11). Fig. 4.14 shows how the coincidence window and scattered pairs can be optimized given the parameters of tab. 4.1.

As fig. 4.13 points out the coincidence rate is extremely low. However, as only few atoms need to be scattered per shot in order to maintain a proper identification of
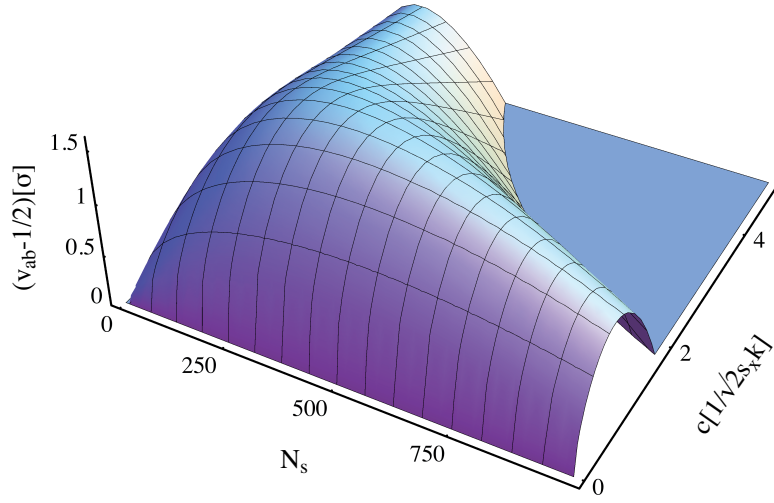
Figure 4.14: The coincidence window and number of scattered atoms can be optimized to achieve best statistical significance. For 400 shots per pixel the visibility can be more than σ above $1/2$.

collision partners anyway, multiple Raman pulses can be launched on to the same BEC. This way more use can be made out of one duty cycle of the experiment. To scatter about 120 pairs about $55\,\mathrm{k}$ atoms need to be released from the trap (compare eq. (3.7)). Hence, about five shots per BEC is realistic.

Taking all parameters given by the system, scattered pairs of $N_s = 120$, and $c = 1.5/\sqrt{2}s_x k$ a visibility of $v_{ab} = 0.71$ can theoretically be achieved and within $10\,h$ of data taking a Poisson error gives a significance of $1.7\,\sigma$ above a visibility[30] of $1/2$. This provides an estimate that it is in general possible to rule out classical correlation with this system. Fig. 4.13 shows how the visibility dramatically improves as the detector resolution improves. Hence, the suggested improvements of chapter 3.2 will bring the system well into the regime where not only the side lobes of the pattern can be observed but indeed a violation of classical correlations should be possible.

In conclusion, a scenario has been described that allows for observation of non-classical interference. The slits of a ghost-interference experiment are moved into the source, such that no additional components are required and the SWA can be used to calculate the expected pattern. In this situation smallest spot sizes are advantageous and the slit distance has to be chosen such that the detector can resolve the fringes on one hand, and lie within the envelope given by the individual source sizes on the other hand. Choosing the number of scattered atoms as well as the right size for the coincidence window are necessary when it comes to accidental counts to still yield high visibilities. The other limiting effect for the visibility is a result of the finite detector resolution. The parameters of the existing system are shown to be within the regime to achieve visibilities higher than $1/2$, which is the limit for classical intensity fluctuations. Possible handles, such as source sizes, scattered atom pairs,

---

[30]Here 15 pixel of the detector are filled with coincidences to cover both side lobes.

coincidence window, are pointed out with which to tune the parameters such that count rates are possible that allow for reasonable acquisition times and still have a significantly small statistical error.

5 Summary and Outlook

A system to cool metastable helium below the transition temperature and condense into a Bose-Einstein condensate has been developed. A high-resolving delay-line detector, capable of detecting single atoms in space and time, has been installed and its performance characterized. In the final section of this dissertation, the power of the metastable helium BEC platform was discussed in the context of its purpose to show entanglement of matter waves in their external degree of freedom.

To achieve Bose-Einstein condensation a sequence of well controlled manipulation and cooling steps has been designed, developed, and built. First, the atoms are excited to their metastable state within a DC-discharge source. Transverse laser cooling facilitates an increase in flux, necessary to achieve high loading rates of a magneto-optical trap, which is loaded via a Zeeman-slowed atomic beam. After transfer to a magnetic trap, the atoms can be cooled to degeneracy, which is accomplished with about 10^6 atoms at $1\,\mu K$. Despite current technical instabilities, this will eventually serve as source for coherent matter waves.

The creation of entanglement will follow the scheme of Perrin et al. by colliding atoms in a four-wave mixing process. The necessary optics, which are even able to generate arbitrary light fields at the position of the BEC, have been installed and tested. Importantly, a micro-channel plate in combination with a delay-line detector has been attached to the system and its characteristics were tested. The delay-line detector has the capability to resolve single-atom detection-events spatially with $120\,\mu m$ and temporally with $250\,ps$ at fluxes of about 10^6 events per second and quadrant. Possible ways to even improve on the spatial resolution capabilities are outlined and will enhance the signal quality further.

The combination of the BEC as source for coherent matter waves, the creation of four-wave mixing in the condensate, and the detection of single atoms to measure correlations will enable the system to perform experiments with non-classical states of matter waves. Among those experiments are double diamond, double double-slit, and ghost-interference experiments. These were described and a version of a hybrid of the double double-slit and ghost-interference experiment has been analyzed in detail for its feasibility to be implemented as entanglement experiment in the current system.

The next steps to realize such an experiment are to improve on the stability of the experiment and the detector resolution. An improved magnetic trap as well as an optical trap can boost the reproducibility of the experiment improving on the statistics obtained from multiple runs. The immediate next step is to create correlated atom pairs, for which the optics has been set up.

A proper identification of pairs, essential for all entanglement experiments, will provide better statistics for experiments on the back-to-back correlations as well. Together with a verification of the spherical wave approximation, which will be shown by measuring the dependence of the correlation uncertainty on the source size

(independent of the BEC size), the pair identification will be the crucial ingredient to perform the envisioned experiment.

This will bring a three-dimensional version of the original Einstein-Podolsky-Rosen paradox closer to realization in a matter-wave system. The envisioned experiment will demonstrate the non-classical character of the state, which is generated in the four-wave mixing process. Subsequent extensions like introducing a phase shift around one source spot or accompanying it with a double double-slit experiment will make even Bell measurements possible.

What is more, while demonstration of entanglement is an exciting experiment by itself, the current setup can eventually be used as platform to test concepts beyond the experiments performed so far with photons. A Franson-like experiment will for example yield significantly different outcomes for matter waves than it is the case for photons. Interference patterns in space and time should be possible to be observed. A multi slit experiment could test Born's rule with entangled matter waves. The significant effect of gravity on matter waves can be tested in an interferometric setup, now even exploiting the aspects of entanglement and possibly enhancing the sensitivity. The spatial-light modulator gives the opportunity to shape most complex light fields at and around the BEC. With this, gratings that facilitate anomalous transmission for matter waves can be generated or non-trivial properties, such as orbital angular momentum states, can be transferred onto the matter wave. The fermionic character of helium-3 can be exploited to investigate the fundamentally different statistics as compared to bosons. For example, four-wave mixing has not been shown for fermions and the Pauli exclusion principle would suggest at first sight a breakdown of the spherical wave approximation. On the other hand though, the necessary anti-symmetrization of the wave function for Fermions proposes an a priori entanglement of the Green's function itself, which only comes in for Bosons upon integration over the source volume.

Hence, it is obvious that with this platform at hand the possibilities of finding and potentially solving a multitude of puzzling yet thrilling questions have significantly grown and it primes the playground to continue the challenge of our perception of the world!

Remerciements

This will read as a list of names but as a matter of fact after more than four years working on this project the people involved were much more part of my life than black ink on white paper. I herewith want to thank especially those people contributing the colorful spots in the picture!

Not only in the past four years, but my whole life has been "sans soucis", because my mom and dad supported all my ideas and let me always know that they are there for me. THANK YOU!

I feel blessed for having my friendships from childhood with Flo and Chris, as well for the ones I found in physics and took beyond with Daniel and Simon. And this is said without neglecting all the other color stains of my life. Thank you!!!

I wanna thank explicitly Ju and Wili for contributing some dark red spots during my time in Vienna!

I want to thank the whole IQOQI. It was a pleasure and honor to walk with all of you. With this I also appreciate to had the opportunity to work with Anton. Thank you, for everything, for creating such an extraordinary environment, and thank you for all the visionary discussions.

Special thanks go to Markus, who is not just an outstanding professor for his own students, but always had a helpful ear for me as well. Thanks a lot!

I also wanna thank my colleagues on the project itself. First, Michi and Mateusz, who have borne the longest with me in this endeavor. Thank you very much! But also Flo and Mandip for their valuable contributions in the lab as well as Johannes for his particular involvement in the theoretical discussions.

It is a pleasure to express my distinct gratitude to Roland, without whose ingenious constructions nothing in this dissertation would have been possible. Thanks for the joyful invites to your kingdom!

I am also grateful for all the helpers in the administration for all the small talks and the big support with all bureaucracy!

The financial support from the University of Vienna is greatly appreciated as well as the extra curricula support from the FWF in form of the CoQuS doctoral program, with all its students and the inspiring discussions with them.

Last but not least I wanna thank two special companions that carried me through this time. Music was such soothing, yet provocative ingredient and certainly got me going, if not gorillas! And sports was indispensable to exhaust the body when the mind had to be cleansed free of thoughts.

A little sweat ain't never hurt nobody. So get the bottles poppin'!

Bibliography

[1] L. de Broglie, Waves and quanta, *Nature* **112**, 540 (1923).

[2] C. Davisson and C. Kunsman, The scattering of electrons by nickel, *Science (New York, NY)* **54**, 522 (1921).

[3] H. Rauch, W. Treimer, and U. Bonse, Test of a single crystal neutron interferometer, *Physics Letters A* **47**, 369 (1974).

[4] R. Colella, A. Overhauser, and S. Werner, Observation of Gravitationally Induced Quantum Interference, *Physical Review Letters* **34**, 1472 (1975).

[5] S. A. Werner and J. L. Staudenmann, Effect of Earth's Rotation on the Quantum Mechanical Phase of the Neutron, *Physical Review Letters* **42**, 1103 (1979).

[6] H. Kaiser, M. Arif, R. Berliner, R. Clothier, S. A. Werner, A. Cimmino, A. G. Klein, and G. I. Opat, Neutron interferometry investigation of the Aharonov-Casher effect, *Nuclear Instruments and Methods in Physics Research Section A: Accelerators, Spectrometers, Detectors and Associated Equipment* **151**, 68 (1988).

[7] H. Batelaan, E. Rasel, M. Oberthaler, J. Schmiedmayer, and A. Zeilinger, Anomalous transmission in atom optics, *Journal of Modern Optics* **44**, 2629 (1997).

[8] C. Keller, M. K. Oberthaler, R. Abfalterer, S. Bernet, J. Schmiedmayer, and A. Zeilinger, Tailored complex potentials and Friedel's law in atom optics, *Physical Review Letters* **79**, 3327 (1997).

[9] M. Oberthaler, R. Abfalterer, S. Bernet, C. Keller, J. Schmiedmayer, and A. Zeilinger, Dynamical diffraction of atomic matter waves by crystals of light, *Physical Review A* **60**, 456 (1999).

[10] M. Arndt, O. Nairz, J. Vos-Andreae, C. Keller, G. Van der Zouw, and A. Zeilinger, Wave-particle duality of C 60 molecules, *Nature* **401**, 680 (1999).

[11] A. Einstein, B. Podolsky, and N. Rosen, Can quantum-mechanical description of physical reality be considered complete?, *Physical Review* **47**, 777 (1935).

[12] W. Heisenberg, Über den anschaulichen Inhalt der quantentheoretischen Kinematik und Mechanik, *Zeitschrift für Physik A Hadrons and Nuclei* **43**, 172 (1927).

[13] D. Bohm and Y. Aharonov, Discussion of experimental proof for the paradox of Einstein, Rosen, and Podolsky, *Physical Review* (1957).

[14] J. Bell, On the einstein-podolsky-rosen paradox, *Physics* **1**, 195 (1964).

[15] J. Bell, On the problem of hidden variables in quantum mechanics, *Reviews of Modern Physics* **38**, 447 (1966).

[16] S. J. Freedman and J. F. Clauser, Experimental Test of Local Hidden-Variable Theories, *Physical Review Letters* **28**, 938 (1972).

[17] L. R. Kasday, J. D. Ullman, and C. S. Wu, Angular correlation of compton-scattered annihilation photons and hidden variables, *Il Nuovo Cimento B* **25**, 633 (1975).

[18] J. Clauser, Experimental Investigation of a Polarization Correlation Anomaly, *Physical Review Letters* **36**, 1223 (1976).

[19] E. S. Fry and R. C. Thompson, Experimental Test of Local Hidden-Variable Theories, *Physical Review Letters* **37**, 465 (1976).

[20] M. Lamehi-Rachti and W. Mittig, Quantum mechanics and hidden variables: A test of Bell's inequality by the measurement of the spin correlation in low-energy proton-proton scattering, *Physical Review D* **14**, 2543 (1976).

[21] A. Aspect, P. Grangier, and G. Roger, Experimental realization of Einstein-Podolsky-Rosen-Bohm Gedankenexperiment: a new violation of Bell's inequalities, *Physical Review Letters* **49**, 91 (1982).

[22] A. Aspect, J. Dalibard, and G. Roger, Experimental test of Bell's inequalities using time-varying analyzers, *Physical Review Letters* **49**, 1804 (1982).

[23] G. Weihs, T. Jennewein, C. Simon, H. Weinfurter, and A. Zeilinger, Violation of Bell's inequality under strict Einstein locality conditions, *Physical Review Letters* **81**, 5039 (1998).

[24] T. Scheidl, R. Ursin, J. Kofler, S. Ramelow, X. S. Ma, T. Herbst, L. Ratschbacher, A. Fedrizzi, N. K. Langford, and T. Jennewein, Violation of local realism with freedom of choice, *Proceedings of the National Academy of Sciences* **107**, 19708 (2010).

[25] M. A. Rowe, D. Kielpinski, V. Meyer, C. A. Sackett, W. M. Itano, C. Monroe, and D. J. Wineland, Experimental violation of a Bell's inequality with efficient detection, *Nature* **409**, 791 (2001).

[26] Z. Merali, Quantum Mechanics Braces for the Ultimate Test, *Science* **331**, 1380 (2011).

[27] A. Ekert and R. Jozsa, Quantum computation and Shor's factoring algorithm, *Reviews of Modern Physics* **68**, 733 (1996).

[28] R. Blatt and D. Wineland, Entangled states of trapped atomic ions, *Nature* **453**, 1008 (2008).

[29] R. Gerritsma, B. Lanyon, G. Kirchmair, F. Zähringer, C. Hempel, J. Casanova, J. García-Ripoll, E. Solano, R. Blatt, and C. Roos, Quantum Simulation of the Klein Paradox with Trapped Ions, *Physical Review Letters* **106**, 060503 (2011).

[30] M. Steffen, M. Ansmann, R. C. Bialczak, N. Katz, E. Lucero, R. McDermott, M. Neeley, E. M. Weig, A. N. Cleland, and J. M. Martinis, Measurement of the Entanglement of Two Superconducting Qubits via State Tomography, *Science* **313**, 1423 (2006).

[31] J. Hald, J. L. Sørensen, C. Schori, and E. S. Polzik, Spin Squeezed Atoms: A Macroscopic Entangled Ensemble Created by Light, *Physical Review Letters* **83**, 1319 (1999).

[32] C. Gross, H. Strobel, E. Nicklas, T. Zibold, N. Bar-Gill, G. Kurizki, and M. K. Oberthaler, Atomic homodyne detection of continuous-variable entangled twin-atom states, *Nature* (2011).

[33] S. Ritter, C. Nölleke, C. Hahn, A. Reiserer, A. Neuzner, M. Uphoff, M. Mücke, E. Figueroa, J. Bochmann, and G. Rempe, An elementary quantum network of single atoms in optical cavities, *Nature* **484**, 195 (2012).

[34] J. Rarity and P. Tapster, Experimental violation of Bell's inequality based on phase and momentum, *Physical Review Letters* **64**, 2495 (1990).

[35] K. Davis, M. Mewes, M. Andrews, N. Van Druten, D. Durfee, D. Kurn, and W. Ketterle, Bose-Einstein condensation in a gas of sodium atoms, *Physical Review Letters* **75**, 3969 (1995).

[36] J. Ensher, M. Matthews, and C. Wieman, Observation of Bose-Einstein condensation in a dilute atomic vapor, *Science* (1995).

[37] R. Brown and R. Twiss, A test of a new type of stellar interferometer on Sirius, *Nature* **178**, 1046 (1956).

[38] M. Schellekens, R. Hoppeler, A. Perrin, J. V. Gomes, D. Boiron, A. Aspect, and C. I. Westbrook, Hanbury Brown Twiss effect for ultracold quantum gases, *Science* **310**, 648 (2005).

[39] R. J. Glauber, Coherent and Incoherent States of the Radiation Field, *Physical Review* **131**, 2766 (1963).

[40] R. J. Glauber, Photon correlations, *Physical Review Letters* **10**, 84 (1963).

[41] R. J. Glauber, The Quantum Theory of Optical Coherence, *Physical Review* **130**, 2529 (1963).

[42] U. M. Titulaer and R. J. Glauber, Correlation Functions for Coherent Fields, *Physical Review* **140**, 676 (1965).

[43] A. Perrin, R. Bücker, S. Manz, T. Betz, C. Koller, T. Plisson, T. Schumm, and J. Schmiedmayer, Hanbury Brown and Twiss correlations across the Bose-Einstein condensation threshold, *Nature Physics* (2012).

[44] S. S. Hodgman, R. G. Dall, A. G. Manning, K. G. H. Baldwin, and A. G. Truscott, Direct Measurement of Long-Range Third-Order Coherence in Bose-Einstein Condensates, *Science* **331**, 1046 (2011).

[45] T. Jeltes, J. McNamara, W. Hogervorst, W. Vassen, V. Krachmalnicoff, M. Schellekens, A. Perrin, H. Chang, D. Boiron, and A. Aspect, Comparison of the Hanbury Brown–Twiss effect for bosons and fermions, *Nature* **445**, 402 (2007).

[46] B. Demarco, Onset of Fermi Degeneracy in a Trapped Atomic Gas, *Science* **285**, 1703 (1999).

[47] S. Inouye, M. Andrews, J. Stenger, H. Miesner, D. Stamper-Kurn, and W. Ketterle, Observation of Feshbach resonances in a Bose–Einstein condensate, *Nature* **392**, 151 (1998).

[48] M. Greiner, C. Regal, and D. Jin, Emergence of a molecular Bose–Einstein condensate from a Fermi gas, *Nature* **426**, 537 (2003).

[49] M. Greiner, C. A. Regal, J. T. Stewart, and D. S. Jin, Probing Pair-Correlated Fermionic Atoms through Correlations in Atom Shot Noise, *Physical Review Letters* **94**, 110401 (2005).

[50] R. Bücker, J. Grond, S. Manz, T. Berrada, T. Betz, C. Koller, U. Hohenester, T. Schumm, A. Perrin, and J. Schmiedmayer, Twin-atom beams, *Nature Physics* (2011).

[51] A. Perrin, H. Chang, V. Krachmalnicoff, M. Schellekens, D. Boiron, A. Aspect, and C. I. Westbrook, Observation of Atom Pairs in Spontaneous Four-Wave Mixing of Two Colliding Bose-Einstein Condensates, *Physical Review Letters* **99**, 150405 (2007).

[52] K. V. Kheruntsyan, J.-C. Jaskula, P. Deuar, M. Bonneau, G. B. Partridge, J. Ruaudel, R. Lopes, D. Boiron, and C. I. Westbrook, Violation of the cauchy-schwarz inequality with matter waves., *Physical Review Letters* **108**, 260401 (2012).

[53] R. G. Dall, L. J. Byron, and A. G. Truscott, Paired-atom laser beams created via four-wave mixing, *Physical Review A* **79**, 011601 (2009).

[54] W. RuGway, S. Hodgman, R. Dall, M. Johnsson, and A. Truscott, Correlations in Amplified Four-Wave Mixing of Matter Waves, *Physical Review Letters* **107**, 075301 (2011).

[55] R. B. Griffiths and R. H. Dicke, Coherent Emission Light Source, *Review of Scientific Instruments* **28**, 646 (1957).

[56] N. Skribanowitz, I. Herman, J. MacGillivray, and M. Feld, Observation of Dicke Superradiance in Optically Pumped HF Gas, *Physical Review Letters* **30**, 309 (1973).

[57] S. Inouye, A. Chikkatur, D. Stamper-Kurn, J. Stenger, D. Pritchard, and W. Ketterle, Superradiant Rayleigh scattering from a Bose-Einstein condensate, *Science (New York, NY)* **285**, 571 (1999).

[58] Č. Brukner and A. Zeilinger, Diffraction of matter waves in space and in time, *Physical Review A* **56**, 3804 (1997).

[59] Č. Brukner and A. Zeilinger, Nonequivalence between stationary matter wave optics and stationary light optics, *Physical Review Letters* **79**, 2599 (1997).

[60] M. Kasevich and S. Chu, Atomic interferometry using stimulated Raman transitions, *Physical Review Letters* **67**, 181 (1991).

[61] P. Bouyer and M. Kasevich, Precision rotation measurements with an atom interferometer gyroscope, *Physical Review Letters* (1997).

[62] H. Müller, A. Peters, and S. Chu, A precision measurement of the gravitational redshift by the interference of matter waves, *Nature* **463**, 926 (2010).

[63] M. Horne and A. Zeilinger, A possible spin-less experimental test of Bell's inequality, *Microphysical Reality and Quantum Formalism* p. 401 (1988).

[64] F. Dalfovo, S. Giorgini, Pitaevskii, L.P., and S. Stringari, Theory of Bose-Einstein condensation in trapped gases, *Reviews of Modern Physics* **71**, 463 (1999).

[65] M. Andrews, C. Townsend, H. Miesner, D. Durfee, D. Kurn, and W. Ketterle, Observation of interference between two Bose condensates, *Science* **275**, 637 (1997).

[66] M. Kotyrba, Metastable-Helium-4 Source For Cold Atom Experiments, *Master Thesis* **University of Vienna**, 1 (2010).

[67] M. Zwierlein, C. Stan, C. Schunck, S. Raupach, S. Gupta, Z. Hadzibabic, and W. Ketterle, Observation of Bose-Einstein Condensation of Molecules, *Physical Review Letters* **91**, 250401 (2003).

[68] T. Weber, J. Herbig, M. Mark, H.-C. Nägerl, and R. Grimm, Bose-Einstein condensation of cesium., *Science* **299**, 232 (2003).

[69] R. Van Rooij, J. S. Borbely, J. Simonet, M. D. Hoogerland, K. S. E. Eikema, R. A. Rozendaal, and W. Vassen, Frequency Metrology in Quantum Degenerate Helium: Direct Measurement of the $2^3S_1 \rightarrow 2^1S_0$ Transition, *Science* **333**, 196 (2011).

[70] R. Bücker, A. Perrin, S. Manz, T. Betz, C. Koller, T. Plisson, J. Rottmann, T. Schumm, and J. Schmiedmayer, Single-particle-sensitive imaging of freely propagating ultracold atoms, *New Journal of Physics* **11**, 103039 (2009).

[71] W. H. Miller, Theory of Penning Ionization. I. Atoms, *Journal of Chemical Physics* **52**, 3563 (1970).

[72] N. Herschbach, P. J. Tol, W. Hogervorst, and W. Vassen, Suppression of Penning ionization by spin polarization of cold He (2^3S) atoms, *Physical Review A* **61**, 50702 (2000).

[73] S. Moal, M. Portier, J. Kim, J. Dugué, U. Rapol, M. Leduc, and C. Cohen-Tannoudji, Accurate Determination of the Scattering Length of Metastable Helium Atoms Using Dark Resonances between Atoms and Exotic Molecules, *Physical Review Letters* **96**, 023203 (2006).

[74] P. Spoden, M. Zinner, N. Herschbach, W. J. van Drunen, W. Ertmer, and G. Birkl, Collisional properties of cold spin-polarized metastable neon atoms., *Physical Review Letters* **94**, 223201 (2005).

[75] I. I. Rabi, Space Quantization in a Gyrating Magnetic Field, *Physical Review* **51**, 652 (1937).

[76] C. Cohen-Tannoudji, B. Diu, and F. Laloë, Quantum Mechanics, *Wiley, New York* (1977).

[77] H. J. Metcalf and P. van der Straten, Laser Cooling and Trapping, *Springer, New York* (1999).

[78] C. Cohen-Tannoudji, Manipulating atoms with photons, *Physica Scripta* **1998**, 33 (2006).

[79] J. Miller, R. Cline, and D. Heinzen, Far-off-resonance optical trapping of atoms, *Multiple values selected* **47**, 4567 (1993).

[80] C. S. Adams, H. J. Lee, N. Davidson, M. Kasevich, and S. Chu, Evaporative Cooling in a Crossed Dipole Trap, *Physical Review Letters* **74**, 3577 (1995).

[81] P. S. Jessen and I. H. Deutsch, Optical lattices, *Advances in atomic, molecular, and optical physics* **37**, 95 (1996).

[82] F. Diedrich, J. Bergquist, W. Itano, and D. Wineland, Laser Cooling to the Zero-Point Energy of Motion, *Physical Review Letters* **62**, 403 (1989).

[83] P. Maunz, T. Puppe, I. Schuster, N. Syassen, P. W. H. Pinkse, and G. Rempe, Cavity cooling of a single atom., *Nature* **428**, 50 (2004).

[84] T. M. Flanagan and J. Goree, Dust release from surfaces exposed to plasma, *Physics of Plasmas* **13**, 3504 (2006).

[85] P.-J. Nacher, E. Courtade, M. Abboud, A. Sinatra, G. Tastevin, and T. Dohnalik, Optical pumping of helium-3 at high pressure and magnetic field, *Acta Physica Polonica B33* pp. 2225–2236 (2002).

[86] Y. Yoshikawa, T. Umeki, T. Mukae, Y. Torii, and T. Kuga, Frequency stabilization of a laser diode with use of light-induced birefringence in an atomic vapor, *Applied Optics* **42**, 6645 (2003).

[87] S. Chu, L. Hollberg, J. Bjorkholm, A. Cable, and A. Ashkin, Three-dimensional viscous confinement and cooling of atoms by resonance radiation pressure, *Physical Review Letters* **55**, 48 (1985).

[88] E. Riis, D. Weiss, K. Moler, and S. Chu, Atom funnel for the production of a slow, high-density atomic beam, *Physical Review Letters* **64**, 1658 (1990).

[89] A. Scholz, M. Christ, D. Doll, J. Ludwig, and W. Ertmer, Magneto-optical preparation of a slow, cold and bright Ne¡ sup¿¡/sup¿ atomic beam, *Optics Communications* **111**, 155 (1994).

[90] A. Aspect, N. Vansteenkiste, R. Kaiser, and H. Haberland, Preparation of a pure intense beam of metastable helium by laser cooling, *Chemical Physics* (1990).

[91] J. Swansson, R. Dall, and A. Truscott, An intense cold beam of metastable helium, *Applied Physics B: Lasers and Optics* **86**, 485 (2007).

[92] M. D. Hoogerland, J. P. J. Driessen, E. J. D. Vredenbregt, H. J. L. Megens, M. P. Schuwer, H. C. W. Beijerinck, and K. A. H. van Leeuwen, Bright thermal atomic beams by laser cooling: A 1400-fold gain in beam flux, *Applied Physics B Laser and Optics* **62**, 323 (1996).

[93] J. Tempelaars, R. Stas, P. Sebel, H. Beijerinck, and E. Vredenbregt, An intense, slow and cold beam of metastable Ne (3s) 3 P 2 atoms, *The European Physical Journal D-Atomic, Molecular, Optical and Plasma Physics* **18**, 113 (2002).

[94] W. Ertmer, R. Blatt, J. L. Hall, and M. Zhu, Laser manipulation of atomic beam velocities: Demonstration of stopped atoms and velocity reversal, *Physical Review Letters* **54**, 996 (1985).

[95] W. Phillips and H. Metcalf, Laser deceleration of an atomic beam, *Physical Review Letters* **48**, 596 (1982).

[96] J. Prodan, W. Phillips, and H. Metcalf, Laser production of a very slow monoenergetic atomic beam, *Physical Review Letters* **49**, 1149 (1982).

[97] C. Dedman, J. Nes, T. Hanna, R. Dall, K. Baldwin, and A. Truscott, Optimum design and construction of a Zeeman slower for use with a magneto-optic trap, *Review of Scientific Instruments* **75**, 5136 (2004).

[98] W. Rooijakkers, W. Hogervorst, and W. Vassen, Laser deceleration and trapping of metastable helium atoms, *Optics Communications* **135**, 149 (1997).

[99] V. S. Letokhov and V. G. Minogin, Laser radiation pressure on free atoms, *Physics Reports* **73**, 1 (1981).

[100] M. Joffe, W. Ketterle, A. Martin, and D. Pritchard, Transverse cooling and deflection of an atomic beam inside a Zeeman slower, *Journal of the Optical Society of America B* **10**, 2257 (1993).

[101] F. Leupold, Production of a Slow Metastable Helium Atomic Beam for a BEC, *Freie Universität Berlin* **Diplomarbeit**, 1 (2010).

[102] E. Raab, M. Prentiss, A. Cable, S. Chu, and D. Pritchard, Trapping of neutral sodium atoms with radiation pressure, *Physical Review Letters* **59**, 2631 (1987).

[103] T. Walker, D. Sesko, and C. Wieman, Collective behavior of optically trapped neutral atoms., *Physical Review Letters* **64**, 408 (1990).

[104] C. Townsend, N. Edwards, C. Cooper, K. Zetie, C. Foot, A. Steane, P. Szriftgiser, H. Perrin, and J. Dalibard, Phase-space density in the magneto-optical trap, *Physical Review A* **52**, 1423 (1995).

[105] F. Dos Santos, F. Perales, J. Léonard, A. Sinatra, J. Wang, F. Pavone, E. Rasel, C. Unnikrishnan, and M. Leduc, Efficient magneto-optical trapping of a metastable helium gas, *Eur. Phys. J. AP* **14**, 69 (2001).

[106] P. Tol, N. Herschbach, E. Hessels, W. Hogervorst, and W. Vassen, Large numbers of cold metastable helium atoms in a magneto-optical trap, *Physical Review A* **60**, 761 (1999).

[107] J. Koelemeij, R. Stas, W. Hogervorst, and W. Vassen, Magneto-optical trap for metastable helium at 389 nm, *Physical Review A* **67**, 053406 (2003).

[108] H. Metcalf, Magneto-optical trapping and its application to helium metastables, *Journal of the Optical Society of America B* **6**, 2206 (1989).

[109] N. Van Druten, D. Durfee, D. Kurn, and W. Ketterle, Direct, nondestructive observation of a Bose condensate, *Physical Review Letters* (1995).

[110] M. Singh, A Magnetic Lattice and Macroscopic Entanglement of a BEC on an Atom Chip, *Swinburne University* **PhD Thesis**, 1 (2008).

[111] P. Tol, Trapping and Evaporative Cooling of Metastable Helium, *Vrije Universiteit Amsterdam* **PhD Thesis**, 1 (2005).

[112] F. Pereira Dos Santos, J. Léonard, J. Wang, C. Barrelet, F. Perales, E. Rasel, C. Unnikrishnan, M. Leduc, and C. Cohen-Tannoudji, Bose-Einstein Condensation of Metastable Helium, *Physical Review Letters* **86**, 3459 (2001).

[113] H. Hess, Evaporative cooling of magnetically trapped and compressed spin-polarized hydrogen, *Physical Review B* **34**, 3476 (1986).

[114] K. Davis, M. Mewes, M. Joffe, M. Andrews, and W. Ketterle, Evaporative cooling of sodium atoms, *Physical Review Letters* **74**, 5202 (1995).

[115] S. Chaudhuri, S. Roy, and C. S. Unnikrishnan, Evaporative Cooling of Atoms to Quantum Degeneracy in an Optical Dipole Trap, *Journal of Physics: Conference Series* **80**, 012036 (2007).

[116] J.-F. Clément, J.-P. Brantut, M. Robert-De-Saint-Vincent, R. A. Nyman, A. Aspect, T. Bourdel, and P. Bouyer, All-optical runaway evaporation to Bose-Einstein condensation, *Physical Review A* **79**, 061406 (2009).

[117] A. L. Migdall, J. V. Prodan, W. D. Phillips, T. H. Bergeman, and H. J. Metcalf, First observation of magnetically trapped neutral atoms, *Physical Review Letters* **54**, 2596 (1985).

[118] S. Nowak, A. Browaeys, J. Poupard, A. Robert, D. Boiron, C. Westbrook, and A. Aspect, Magnetic trapping of metastable helium atoms, *Applied Physics B: Lasers and Optics* **70**, 455 (2000).

[119] N. Herschbach, P. Tol, A. Tychkov, W. Hogervorst, and W. Vassen, Magnetic trapping and evaporative cooling of metastable triplet helium, *Journal of Optics B: Quantum and Semiclassical Optics* **5**, S65 (2003).

[120] C. Zener, Non-adiabatic crossing of energy levels, *Proceedings of the Royal Society of London. Series A, Containing Papers of a Mathematical and Physical Character* **137**, 696 (1932).

[121] W. Petrich, M. Anderson, J. Ensher, and E. Cornell, Stable, tightly confining magnetic trap for evaporative cooling of neutral atoms, *Physical Review Letters* **74**, 3352 (1995).

[122] D. J. Han, R. H. Wynar, P. Courteille, and D. J. Heinzen, Bose-Einstein condensation of large numbers of atoms in a magnetic time-averaged orbiting potential trap, *Physical Review A* **57**, 4114 (1998).

[123] C. V. Sukumar and D. M. Brink, Spin-flip transitions in a magnetic trap, *Physical Review A* **56**, 2451 (1997).

[124] P. O. Schmidt, S. Hensler, J. Werner, T. Binhammer, A. Görlitz, and T. Pfau, Doppler cooling of an optically dense cloud of magnetically trapped atoms, *JOSA B* **20**, 960 (2003).

[125] K. Bergmann and H. Theuer, Coherent population transfer among quantum states of atoms and molecules, *Reviews of Modern Physics* (1998).

[126] J. Stenger, S. Inouye, A. Chikkatur, D. Stamper-Kurn, D. Pritchard, and W. Ketterle, Bragg spectroscopy of a Bose-Einstein condensate, *Physical Review Letters* **82**, 4569 (1999).

[127] P. B. Blakie, R. J. Ballagh, and C. W. Gardiner, Theory of coherent Bragg spectroscopy of a trapped Bose-Einstein condensate, *Physical Review A* **65**, 033602 (2002).

[128] P. Ernst, S. Götze, J. Krauser, K. Pyka, D. Lühmann, D. Pfannkuche, and K. Sengstock, Probing superfluids in optical lattices by momentum-resolved Bragg spectroscopy, *Nature Physics* **6**, 56 (2009).

[129] H. Müller, S.-w. Chiow, Q. Long, S. Herrmann, and S. Chu, Atom Interferometry with up to 24-Photon-Momentum-Transfer Beam Splitters, *Physical Review Letters* **100**, 180405 (2008).

[130] K. Boller, A. Imamolu, and S. Harris, Observation of electromagnetically induced transparency, *Physical Review Letters* **66**, 2593 (1991).

[131] C. Liu, Z. Dutton, C. H. Behroozi, and L. V. Hau, Observation of coherent optical information storage in an atomic medium using halted light pulses, *Nature* **409**, 490 (2001).

[132] V. Krachmalnicoff, J.-C. Jaskula, M. Bonneau, V. Leung, G. B. Partridge, D. Boiron, C. I. Westbrook, P. Deuar, P. Ziń, M. Trippenbach, and K. V. Kheruntsyan, Spontaneous four-wave mixing of de Broglie waves: beyond optics., *Physical Review Letters* **104**, 150402 (2010).

[133] P. Ziń, J. Chwedeńczuk, and M. Trippenbach, Elastic scattering losses from colliding Bose-Einstein condensates, *Physical Review A* **73**, (2006).

[134] K. V. Kheruntsyan, M. K. Olsen, and P. D. Drummond, Einstein-Podolsky-Rosen Correlations via Dissociation of a Molecular Bose-Einstein Condensate, *Physical Review Letters* **95**, 150405 (2005).

[135] P. D. Drummond and C. W. Gardiner, Generalised P-representations in quantum optics, *Reports on Progress in Physics* **13**, 2353 (1999).

[136] A. Perrin, C. Savage, D. Boiron, V. Krachmalnicoff, C. Westbrook, and K. Kheruntsyan, Atomic four-wave mixing via condensate collisions, *New Journal of Physics* **10**, 045021 (2008).

[137] L. Deng, E. W. Hagley, J. Wen, M. Trippenbach, Y. Band, P. S. Julienne, J. E. Simsarian, K. Helmerson, S. L. Rolston, and W. D. Phillips, Four-wave mixing with matter waves, *Nature* **398**, 218 (1999).

[138] R. W. Gerchberg and W. O. Saxton, A practical algorithm for the determination of phase from image and diffraction plane pictures, *Optik)* **35**, 237246 (1972).

[139] C. Firmani, High-resolution imaging with a two-dimensional resistive anode photon counter, *Review of Scientific Instruments* **53**, 570 (1982).

[140] O. Jagutzki, V. Mergel, K. Ullmann-Pfleger, L. Spielberger, U. Spillmann, R. Dörner, and H. Schmidt-Böcking, A broad-application microchannel-plate detector system for advanced particle or photon detection tasks: large area imaging, precise multi-hit timing information and high detection rate, *Nuclear Instruments and Methods in Physics Research Section A: Accelerators, Spectrometers, Detectors and Associated Equipment* **477**, 244 (2002).

[141] O. Jagutzki, A. Cerezo, A. Czasch, R. Dörner, M. Hattas, M. Huang, V. Mergel, U. Spillmann, K. Ullmann-Pfleger, and T. Weber, Multiple hit readout of a microchannel plate detector with a three-layer delay-line anode, *Nuclear Science, IEEE Transactions on* **49**, 2477 (2002).

[142] N. Bohr, Can quantum-mechanical description of physical reality be considered complete?, *Physical Review* **48**, 696 (1935).

[143] L.-M. Duan, G. Giedke, J. I. Cirac, and P. Zoller, Inseparability Criterion for Continuous Variable Systems, *Physical Review Letters* **84**, 2722 (2000).

[144] J. Clauser, M. Horne, A. Shimony, and R. Holt, Proposed experiment to test local hidden-variable theories, *Physical Review Letters* **23**, 880 (1969).

[145] A. S. Holevo, Information-theoretical aspects of quantum measurement, *Problemy Peredachi Informatsii* **9**, 31 (1973).

[146] R. P. Feynman, Simulating Physics with Computers, *International Journal of Theoretical Physics* **21**, 467 (1982).

[147] C. H. Bennett and G. Brassard, Quantum cryptography: Public key distribution and coin tossing, in *Proceedings of IEEE International . . .* (1984).

[148] D. P. DiVincenzo, Quantum computation, *Science* (1995).

[149] R. Horodecki, P. Horodecki, and M. Horodecki, Quantum entanglement, *Reviews of Modern . . .* (2009).

[150] M. Ansmann, H. Wang, R. C. Bialczak, M. Hofheinz, E. Lucero, M. Neeley, A. D. O'Connell, D. Sank, M. Weides, J. Wenner, A. N. Cleland, and J. M. Martinis, Violation of Bell's inequality in Josephson phase qubits, *Nature* **461**, 504 (2009).

[151] J. Rarity, P. Tapster, E. Jakeman, and T. Larchuk, Two-photon interference in a Mach-Zehnder interferometer, *Physical Review Letters* (1990).

[152] M. D'angelo, Y.-H. Kim, S. Kulik, and Y. Shih, Identifying Entanglement Using Quantum Ghost Interference and Imaging, *Physical Review Letters* **92**, 233601 (2004).

[153] P.-A. Moreau, J. Mougin-Sisini, F. Devaux, and E. Lantz, Realization of the purely spatial Einstein-Podolsky-Rosen paradox in full-field images of spontaneous parametric down-conversion, *Physical Review A* **86**, 010101 (2012).

[154] M. P. Edgar, D. S. Tasca, F. Izdebski, R. E. Warburton, J. Leach, M. Agnew, G. S. Buller, R. W. Boyd, and M. J. Padgett, Imaging high-dimensional spatial entanglement with a camera., *Nature Communications* **3**, 984 (2012).

[155] R. W. Boyd, Nonlinear Optics, *Academic Press, New York)* **3rd edition** (2008).

[156] D. F. Walls and G. J. Milburn, Quantum Optics, *Springer* **2nd edition** (2008).

[157] K. Kheruntsyan, Quantum Atom Optics with Fermions from Molecular Dissociation, *Physical Review Letters* **96**, 110401 (2006).

[158] C. Gneiting and K. Hornberger, Bell Test for the Free Motion of Material Particles, *Physical Review Letters* **101**, 260503 (2008).

[159] A. Peters, K. Y. Chung, and S. Chu, Measurement of gravitational acceleration by dropping atoms, *Nature* **400**, 849 (1999).

[160] S. S. Szigeti, J. E. Debs, J. J. Hope, N. P. Robins, and J. D. Close, Why momentum width matters for atom interferometry with Bragg pulses, *New Journal of Physics* **14**, 023009 (2012).

[161] K. M. Hilligsøe and K. Mølmer, Phase-matched four wave mixing and quantum beam splitting of matter waves in a periodic potential, *Physical Review A* **71**, 41602 (2005).

[162] G. K. Campbell, J. Mun, M. Boyd, E. W. Streed, W. Ketterle, and D. E. Pritchard, Parametric Amplification of Scattered Atom Pairs, *Physical Review Letters* **96**, 020406 (2006).

[163] A. Ferris, M. Olsen, and M. Davis, Atomic entanglement generation and detection via degenerate four-wave mixing of a Bose-Einstein condensate in an optical lattice, *Physical Review A* **79**, 043634 (2009).

[164] P. Storey and C. Cohen-Tannoudji, The Feynman path integral approach to atomic interferometry. A tutorial, *Journal de Physique II* **4**, 1999 (1994).

[165] R. Feynman, Space-Time Approach to Non-Relativistic Quantum Mechanics, *Reviews of Modern Physics* **20**, 367 (1948).

[166] M. Horne and A. Zeilinger, Quantum mechanical studies for Abner Shimony, *edited by A. van der Merwe, F. Selleri, and G. Tarozzi (Kluwer Academic, Dordrecht)* **Microphysical Reality and Quantum Formalism** (1988).

[167] D. Greenberger, M. Horne, and A. Zeilinger, Multiparticle interferometry and the superposition principle, *Physics Today* **46**, 22 (1993).

[168] M. Horne, Quantum mechanical studies for Abner Shimony, *edited by R. S. Cohen, M. Horne, and J. Stachel (Kluwer Academic, Dordrecht)* **Experimental metaphysics**, 258 p. (1997).

[169] J. Kofler, M. Singh, M. Ebner, M. Keller, M. Kotyrba, and A. Zeilinger, Einstein-Podolsky-Rosen correlations from colliding Bose-Einstein condensates, *Physical Review A* **86**, 032115 (2012).

[170] M. O. Scully and K. Drühl, Quantum eraser: A proposed photon correlation experiment concerning observation and "delayed choice" in quantum mechanics, *Physical Review A (General Physics)* **25**, 2208 (1982).

[171] P. Kwiat, A. Steinberg, and R. Chiao, Observation of a "quantum eraser": A revival of coherence in a two-photon interference experiment, *Physical Review A* **45**, 7729 (1992).

[172] T. J. Herzog, P. G. Kwiat, H. Weinfurter, and A. Zeilinger, Complementarity and the Quantum Eraser, *Physical Review Letters* **75**, 3034 (1995).

[173] A. Gatti, E. Brambilla, M. Bache, and L. Lugiato, Ghost Imaging with Thermal Light: Comparing Entanglement and ClassicalCorrelation, *Physical Review Letters* **93**, 093602 (2004).

[174] A. Valencia, G. Scarcelli, M. D'Angelo, and Y. Shih, Two-Photon Imaging with Thermal Light, *Physical Review Letters* **94**, 063601 (2005).

[175] M. D'Angelo, A. Valencia, M. Rubin, and Y. Shih, Resolution of quantum and classical ghost imaging, *Physical Review A* **72**, 013810 (2005).

[176] D. Strekalov, A. Sergienko, D. Klyshko, and Y. Shih, Observation of Two-Photon "Ghost" Interference and Diffraction, *Physical Review Letters* **74**, 3600 (1995).

[177] M. D'Angelo, Y.-H. Kim, S. P. Kulik, and Y. Shih, Identifying Entanglement Using Quantum Ghost Interference and Imaging, *Physical Review Letters* **92**, 233601 (2004).

[178] M. Jakob and J. A. Bergou, Quantitative complementarity relations in bipartite systems: Entanglement as a physical reality, *Optics Communications* **283**, 827 (2010).

[179] G. Jaeger, M. Horne, and A. Shimony, Complementarity of one-particle and two-particle interference., *Physical Review A* **48**, 1023 (1993).

[180] G. Jaeger, A. Shimony, and L. Vaidman, Two interferometric complementarities., *Physical Review A* **51**, 54 (1995).

[181] G. Jaeger, Generalized Quantum Probability and Entanglement Enhancement Witnessing, *Foundations of Physics* **42**, 752 (2012).

[182] C. Su and K. Wódkiewicz, Quantum versus stochastic or hidden-variable fluctuations in two-photon interference effects, *Physical Review A* **44**, 6097 (1991).

[183] L. Mandel, Photon interference and correlation effects produced by independent quantum sources, *Physical Review A* **28**, 929 (1983).

[184] A. Ferris, M. Olsen, E. Cavalcanti, and M. Davis, Detection of continuous variable entanglement without coherent local oscillators, *Physical Review A* **78**, 060104 (2008).

[185] C. Gneiting and K. Hornberger, Detecting Entanglement in Spatial Interference, *Physical Review Letters* **106**, 210501 (2011).

[186] M. Greiner, O. Mandel, T. Esslinger, T. Hänsch, and I. Bloch, Quantum phase transition from a superfluid to a Mott insulator in a gas of ultracold atoms, *Nature* **415**, 39 (2002).

[187] J. Estève, C. Gross, A. Weller, S. Giovanazzi, and M. K. Oberthaler, Squeezing and entanglement in a Bose–Einstein condensate, *Nature* **455**, 1216 (2008).

[188] U. Sinha, C. Couteau, T. Jennewein, R. Laflamme, and G. Weihs, Ruling Out Multi-Order Interference in Quantum Mechanics, *Science* **329**, 418 (2010).

[189] Y. Aharonov, H. Pendleton, and A. Petersen, Modular variables in quantum theory, *International Journal of Theoretical Physics* **2**, 213 (1969).

[190] S. Popescu, Dynamical quantum non-locality, *Nature Physics* **6**, 151 (2010).

[191] J. Tollaksen, Y. Aharonov, A. Casher, T. Kaufherr, and S. Nussinov, Quantum interference experiments, modular variables and weak measurements, *New Journal of Physics* **12**, 013023 (2010).

[192] S. Ramelow, A. Mech, M. Giustina, and S. Groeblacher, Highly efficient heralding of entangled single photons, *arXiv.org* (2012).

Curriculum Vitae

Personal Information

Name: Maximilian Ebner
Date of Birth: 11/15/1982
Place of Birth: Bad Schwalbach, Germany

Education

May 08 - Feb. 13	University of Vienna, Austria
Feb. 13	P.h.D. in physics, "Development of a metastable helium BEC as a platform for experiments with EPR-entangled matter waves"
Aug. 06 - Dec. 07	University of Texas at Austin, USA
Dec. 07	M.A. in Physics, "Biological Nanofibers in a Standing Wave Optical Trap"
Oct. 03 - Jul. 06	University of Würzburg, Germany
Oct. 05	Vordiplom, Grade: 1.3
Sep. 1989 - Jun. 02	Freie Waldorfschule Wiesbaden
Jun. 02	Abitur, Grade: 1.2

Miscellaneous

Sep. 09 - Feb. 13	Teaching of lab courses and exercises
Feb. - Jun 10	Visiting scientist at the Harvard University, Cambridge, USA
Sep. 09	Organization of the "CoQuS Summer School 2009"
Jul. 08 - Feb. 13	Fellow of the Doctoral Program on Complex Quantum Systems "CoQuS" (FWF)
Aug. 06 - May 07	Scholarship of the German DAAD
Jun. 02	Book price of the German Physics Society (DPG)